Rapid Fracture Resistance of Polyethylene: Dependence on Polymer Structure

Pemra Özbek

Imperial College London

Department of Mechanical Engineering

A thesis submitted for the degree of

Doctor of Philosophy of Imperial College London

January 2008

To my family

the end...

...the beginning

Abstract

Polymer pipe materials being widely used in the industry for transport purposes introduced new areas of research from mechanics of materials perspective. In this study the effect of structural parameters on the fracture resistance of polyethylene pipe material have been investigated via testing materials differing in their overall structure, density, crystallinity, molecular weight, and carbon black by performing S4 tests in addition to Instrumented Charpy, Reversed Charpy and Tensile Tests. Furthermore, the effect of extrusion conditions have been investigated via performing S4 Tests on pipes having differing process histories.

A new technique of analysing tensile testing enlightening plane stress resistance is demonstrated. The stability of adiabatic drawing in a tensile test is found to be related to the plane stress fracture resistance, which forms the basis of the RCP resistance of a pipe. This proposed method enables the use of two basic material properties – yield stress and strain hardening modulus – for ranking of the pipes RCP performances, making the idea of *tailor-made* pipes possible.

Acknowledgements

I wish to express my deepest gratitude to Dr. P. S. Leevers for his supervision, help and support during this work. I would also like to thank to the members of Mechanics of Materials Group and all technical staff. In particular to Tom Nolan for his friendly attitude at all times in addition to his endless support and encouragement.

I am indebted to my sponsors, Chevron Phillips Chemical Company for their financial, technical and personal support at all times, and especially to Raj Krishnaswamy, Mark Lamborn and Ashish Sukhadia.

I have been very lucky to have met amazing people during my PhD to whom I will be grateful forever. My special thanks goes to my *family* in London; Vassia, Mihalis and Burak, who never let me be alone, Sabine and Marie for their kind supports, Chris for his friendship as well as his contributions to this work and to all those coffee breaks with Markus and Markus, which kept us joyful and motivated.

I cannot thank enough to my family, whose presence had been the motivating factor of my studies, and especially to my sister Nil, who always makes me laugh. Last but not least, I would like to thank to Can, who had been the initiative factor of this study, as well as the kind support at all times.

Contents

Abstract **3**

Acknowledgements **4**

List of Figures **10**

List of Tables **16**

1 Introduction **17**

1.1 Use of PE in the Pipe Industry 18

1.2 Defining Failure Characteristics and Transition behaviour 19

1.3 Thesis Outline 20

2 Review of Polyethylene Structure **22**

2.1 Structure of Polyethylene 22

2.2 Molecular Weight 24

2.2.1 Molecular Weight Distribution & Branching: PE 80 *vs.* PE 100 25

2.3 Crystallinity 26

2.3.1 Degree of Crystallinity 31

2.3.2 Mechanism of Crystallisation 32

2.3.3 Kinetics of Crystallisation 33

2.4 Glass Transition 34

2.5 Carbon Black Filler 35

2.6 Conclusion 35

3 Fracture Mechanics **37**

3.1 Linear Elastic Fracture Mechanics, (LEFM) 38

3.1.1 Energy Based Analysis 38

3.1.2 Stress Based Analysis 40

3.1.2.1 Plane Stress *vs.* Plane Strain 41

3.1.2.2 Determination of plane strain and plane stress fracture resistance 42

3.1.2.3 Prediction of plane stress and plane strain fracture resistance 44

3.1.3 Geometry Factor Determination for Arc-Shaped Geometry . 45

3.1.3.1 Derivation of Equations 46

3.1.3.2 Calculation of Integral and Derivative expressions using Matlab and Maple 48

3.1.3.3 Determination of the Integral Constant (C_0) using ANSYS 48

3.1.3.4 Determination of ϕ 51

3.1.3.5 Generalizing calculations for other pipe geometries 53

3.2 Elastic Plastic Fracture Mechanics, EPFM 55

3.2.1 Essential Work of Fracture (EWF) Method 55

3.3 Conclusions 56

4 Rapid Crack Propagation Tests on Pipe **57**

4.1 RCP Phenomena and Test Methods 57

4.1.1 Full Scale Test 58

4.1.2 Small Scale Steady State (S4) Test 59

4.2 Determination of RCP Properties: Critical Pressure and Critical Temperature 60

4.2.1 Definition from Single Test Results 61

4.2.2 Explaining P_c in terms of material properties 63

4.2.3 Plane stress and plane strain fracture in pipes 63

4.3 S4 Test Results 65

4.3.1 Specimen Preparation 66

4.3.2 Experimental Results 67

4.3.2.1 S4-11: Effect of Carbon Black and Extrusion Screw Type 67

4.3.2.2 S4-7: Effect of Extrusion Rate and Extrusion Set Temperature 70
4.3.3 Conclusions 73

5 ISO CD 17281 Impact Bend Test 77
5.1 Experimental Method and Specimen Preparation 78
5.1.1 Preparation of the moulded plaque specimens 79
5.1.1.1 Moulding rectangular specimens 79
5.1.1.2 Moulding arc-shaped specimens 80
5.1.2 Preparation of the pipe specimens 80
5.1.3 Thermal Conditioning Press 81
5.2 Analysis of the Instrumented Charpy Impact Test 83
5.2.1 Brittle-Tough Transition Temperature Determination Methods 85
5.2.1.1 Observation of the Fracture Surface 85
5.2.1.2 Observation of Load Displacement Traces, U^* Method 86
5.2.1.3 Load Ratio Method 87
5.3 Experimental Results 88
5.3.1 C-Series PE Resins 88
5.3.1.1 Determination of Crystallinity: Differential Scanning Calorimetry (DSC) 89
5.3.1.2 Determination of Tensile Modulus: Dynamical Mechanical Thermal Analysis (DMTA) 90
5.3.1.3 Load-Displacement Plots 92
5.3.1.4 Impact Fracture Resistance (G_c) 94
5.3.1.5 Brittle-Tough Transition Temperature Analysis . . 101
5.3.2 Effect of Density: D-Series PE Resins 103
5.3.3 Effect of Molecular Weight: MW-Series PE Resins 106
5.3.4 Effect of Carbon Black Dispersion 109
5.4 Discussion & Conclusions 110

6 Reversed Charpy Test 112
6.1 Experimental Method 113
6.2 Analysis of Reversed Charpy Test 115
6.3 Experimental Results 118

6.3.1 Effect of Notching Technique . . . 118
6.3.2 C-Series PE Resins . . . 119
6.3.3 Effect of Density: D-Series PE Resins . . . 121
6.3.4 Effect of Molecular Weight: MW-Series PE Resins . . . 121
6.3.5 Effect of Carbon Black Dispersion . . . 124
6.4 Discussion & Conclusions . . . 124
6.4.1 Contributions of Plane Strain and Plane Stress Regions to Overall Fracture Resistance . . . 126

7 Correlation of Plane Stress Fracture with Uniaxial Tensile Properties 129
7.1 Uniaxial Tensile Testing . . . 130
7.2 Tensile Test Curve . . . 132
7.3 Considère's Construction . . . 133
7.4 Eyring's Model . . . 135
7.5 Haward-Thackray Model . . . 137
7.6 Thermomechanical Effects . . . 140
7.7 Relation between the Reversed Charpy and the Tensile Test . . . 142
7.8 Deformation Mechanisms . . . 144
7.9 Tensile Test Experiments . . . 148
7.9.1 Procedure and Analysis of Tensile Test . . . 148
7.9.2 Experimental Results . . . 153
7.9.2.1 C-Series PE Resins . . . 153
7.9.2.2 Effect of Density: D-Series PE Resins . . . 162
7.9.2.3 Effect of Molecular Weight: MW Series PE Resins 165
7.10 Discussion and Conclusions . . . 167
7.10.1 Sensitivity analysis . . . 169
7.10.1.1 An alternative analysis method by reduction of parameters . . . 171
7.10.2 Relationship between Reversed Charpy and tensile test results 172

8 Conclusions and Recommendations for Future Work 175
8.1 Overview . . . 175
8.2 S4 Test Results . . . 176
8.3 Effect of structural changes on test parameters . . . 177

8.4 Arc-Shaped geometry factor determination 177
8.5 Uniaxial Tensile Test 178
8.6 Relationships between the test results 178
8.7 Recommendations for future work 179

Bibliography **181**

List of Figures

1.1 Timeline of Polymer Discoveries 18

2.1 Polyethylene Formation 23
2.2 Chain structure of Polyethylene 23
2.3 Entanglement of polymer chains (a)Low molecular weight, no entanglement (b) High molecular weight, chains are entangled 24
2.4 MW and chain branching distribution in unimodal PE 80 and bimodal PE 100 25
2.5 Crystallinity in Polyethylene 27
2.6 Fringed-micelle model of crystallites in amorphous matrix [1] 27
2.7 The chain-folded structure for a plate-shaped polymer crystallite [1] 28
2.8 Polymer crystalline spherulite 29
2.9 Polymer crystalline spherulite [2] 30
2.10 Stages of spherulitic growth during melt crystallisation of PE [3] . . 30

3.1 Energy Based Analysis Definitions 39
3.2 Plastic zone ahead of crack in a plate of finite thickness [1] 41
3.3 Rectangular Plaque Specimen 43
3.4 Side-grooved specimen 43
3.5 Standard arc-shaped geometry as suggested by ASTM 399-90 . . . 46
3.6 FEM Model of an unnotched arc-shaped specimen 49
3.7 FEM model details 49
3.8 Compliance values obtained from ANSYS for PE, differing S/W ratios [49] 50
3.9 Geometry factor (ϕ) values determined for arc-shaped specimens . . 51
3.10 Checking the validity of extrapolations 52
3.11 Comparison of ϕ values of arc-shaped and rectangular specimens . . 53
3.12 Geometry factor (ϕ) values for different pipe geometries 54

4.1 Schematic representation of an S4 Test [2] 59
4.2 PE pipe subjected to the S4 test [2] above its critical pressure . . . 60
4.3 RCP boundaries determining critical conditions 61
4.4 Determination of Critical Temperature (T_{c-S4}) at test pressure P=5 bar 62
4.5 Plane strain and plane stress regions on an impacted fracture surface of a pipe (units in mm) 64
4.6 110 SDR 11, S4 Test Pipe Specimen 65
4.7 Extrusion Screw types [4] 66
4.8 Data for the pipe specimens 68
4.9 S4 Test Results for Material 1 69
4.10 S4 Test Results for Material 2 69
4.11 S4 Test Results for Material 3 70
4.12 Comparison of S4 Critical Temperature Values for 3 materials as a function of carbon black content and shear 71
4.13 S4 Critical Temperature Values (°C) for pipes extruded at 193°C at different extrusion rates (see Table 4.2) 73
4.14 S4 Critical Temperature Values (°C) for pipes extruded at 250°C at different extrusion rates (see Table 4.2) 74
4.15 S4 Critical Temperature Values (°C) for pipe extruded at 227°C, having extrusion rate of 1.13 kg/min 74
4.16 Comparison of S4 Critical Temperature values for various extrusion temperatures and rates 75

5.1 Three Point Bend Impact Test arrangement 78
5.2 Compression Moulding Plaques 80
5.3 Arc-shaped Moulding Plaque 81
5.4 Rectangular Plaque Specimen 81
5.5 Arc-Shaped Specimen 82
5.6 Side-grooved Plaque Specimen 82
5.7 Thermal History Rig [5] 83
5.8 Heating and cooling rate for top half [5] 84
5.9 Interpreting Load-Displacement traces on a specimen surface having dimensions of 12×12mm, with a notch of 3mm 84
5.10 Observation of transition in the load displacement curve 86

5.11 U* Method 87
5.12 Misleading results can be obtained if the U* method is not applied correctly 87
5.13 Load Ratio Method 88
5.14 Percentage Crystallinity Results for C-Series PE Resins for varying cooling rate conditions 90
5.15 Modulus (E') versus Temperature for C-Series PE Resins, 10Hz . . 91
5.16 Modulus (E') (0°C, 10Hz) versus Density for C-Series PE Resins . . 91
5.17 Processing, Geometry and Plane Stress Effects on Load Displacement Curves: (a) Effect of Processing (PE-3) (b)Effect of Processing (different cooling rates) (PE-4) (c) Effect of Geometry (PE-6) (d) Effect of Plane Stress (PE-4) 93
5.18 Impact Fracture Resistance (G_c) versus temperature plots of C Series PE resins 94
5.19 *(Cont.)* Impact Fracture Resistance (G_c) versus temperature plots of C Series PE resins 95
5.20 Relationship between G_c and Modulus 96
5.21 Moulded arc-shaped specimens 97
5.22 Effect of processing conditions on G_c 98
5.23 Investigation of Error range in G_c, PE-6 98
5.24 Investigation of Error range in G_c, PE-8 99
5.25 Effect of processing conditions on G_c 100
5.26 Possible error in determination of G_c (demonstrated for PE-3, 20°C) 100
5.27 Effect of M_W on G_c values, 0°C 101
5.28 Comparison of T_{BT} Values for C-Series PE resins 102
5.29 Comparison of T_{BT} Values with S4 T_c Values 103
5.30 Modulus (E') versus Temperature for D-Series PE Resins, 10Hz . . 105
5.31 Modulus (E') (0°C, 10Hz) versus Density for D-Series PE Resins . . 105
5.32 Effect of density on the load-displacement traces 106
5.33 Effect of Density on Brittle-Tough Transition Temperature 106
5.34 Effect of Temperature on G_c for D-Series PE Resins 107
5.35 Effect of M_w on impact load-displacement traces at 0°C 108
5.36 Effect of M_w on the load-displacement traces 108
5.37 Effect of CB addition on impact load-displacement traces at 20°C . 110
5.38 Investigation of Carbon Black Effect 110

6.1 Reversed Charpy Test arrangement 114
6.2 Rectangular Specimen 114
6.3 Arc-shaped Specimen 115
6.4 High speed photographs of specimens during fracture [2] 116
6.5 High speed photographs of specimens during fracture [2] 116
6.6 Reversed Charpy Load-Displacement Trend 118
6.7 Effect of Notching Technique on the Load-Displacement Trace . . . 119
6.8 Effect of Temperature on Plane Stress Resistance for C-Series PE Resins 120
6.9 Effect of Temperature on Yield Stress 120
6.10 Effect of Processing Conditions on yield stress and plane stress fracture resistance, 0°C 121
6.11 Effect of Temperature on Reversed Charpy test parameters for Density series 122
6.12 Effect of Density on Reversed Charpy Test parameters, 0°C 122
6.13 Effect of MW on Reversed Charpy load-displacement traces 123
6.14 Effect of Temperature on Reversed Charpy test parameters for M_W series 123
6.15 Effect of M_W on Reversed Charpy Test parameters 124
6.16 Effect of Carbon Black additon on Reversed Charpy Test parameters 125

7.1 Typical Stress-Strain Curve for a ductile semicrystalline polymer . . 133
7.2 Considère's Construction Curves 135
7.3 Eyring model of solid Flow 136
7.4 Haward-Thackray Spring-Dashpot Model, ($\sigma_t = \sigma_y + G_p(\lambda^2 - 1/\lambda)$) 137
7.5 Mushroom ends from a PET fibre broken at high strain rate [6] . . 140
7.6 Load-Displacement Trace Comparison between Reversed Charpy and Tensile Test, 20°C, PE-8 143
7.7 Yield stress Comparison between Reversed Charpy and Tensile Test (6 mm/min, ($4 \times 10^{-3} s^{-1}$)), 20°C 144
7.8 (a) Spherulitic structure at entry to the neck (b) One-third of the way into the neck (c) Two-thirds of the neck (d) Fully developed drawn texture at the base of the neck [7] 146

7.9 Eyring Plot: Yield Stress and Stress Hardening Modulus as a function of the logarithm of nominal strain rate (based on gauge length of 25 mm; 1.6× $10^{-4}s^{-1}$, 8× $10^{-4}s^{-1}$ and 4× $10^{-3}s^{-1}$) at three temperatures 150
7.10 Tensile Specimen Geometry 151
7.11 Determination of adiabatic drawing stability β_c using Considère's condition, 20°C, 1 s^{-1}, PE-3 (CR0.5) 154
7.12 Effect of Cross-Head Speed (mm/min) on the Tensile Deformation at Constant Temperature, 20°C 155
7.13 Effect of Temperature on the Tensile Deformation at a constant rate, 10 mm/min (6.66 × $10^{-3}s^{-1}$) 155
7.14 Effect of Cooling rate on the Tensile Deformation at a constant rate, 6 mm/min (4 × $10^{-3}s^{-1}$) and temperature 20°C 156
7.15 Effect of cooling rate on strain hardening modulus and yield stress, based on data of 6mm/min (4 × $10^{-3}s^{-1}$), 20°C 157
7.16 The effect of cooling rate on the adiabatic drawing stability 159
7.17 Effect of assumed adiabatic strain rate and initial temperature on adiabatic drawing stability, CR1.5 159
7.18 Correlation between adiabatic drawing stability and plane stress fracture resistance (reversed Charpy), at 0°C 160
7.19 Critical strain rate determination method (CR1.5) 161
7.20 Relationship between critical strain rate and adiabatic drawing stability (CR1.5) 161
7.21 Effect of Density on the Tensile Deformation at a constant rate, 1.2 mm/min (8 × $10^{-4}s^{-1}$) and temperature 40°C 162
7.22 Effect of density on strain hardening modulus and yield stress, 6mm/min (4 × $10^{-3}s^{-1}$) 163
7.23 Observation of Necking Behaviour 163
7.24 Correlation between adiabatic drawing stability and plane stress fracture resistance, at 0°C 164
7.25 Effect of density on adiabatic drawing stability 164
7.26 Effect of MW on the Tensile Deformation at Constant Temperature, 20°C and crosshead speed 1.2mm/min (8 × $10^{-4}s^{-1}$) 165
7.27 Effect of MW on strain hardening modulus and yield stress, 1.2 mm/min (8 × $10^{-4}s^{-1}$) 166

7.28 Correlation between adiabatic drawing stability (20°C, 1/s) and plane stress fracture resistance (0°C) 166
7.29 Effect of MW on adiabatic drawing stability, (20°C, 1/s) 167
7.30 Relationship between the parameters 168
7.31 Sensitivity analysis on adiabatic drawing stability 170
7.32 Effect of parameters on adiabatic drawing stability 173
7.33 Effect of ratio of V* on β_c 174

List of Tables

3.1 Integral Constant values, C_0EB, $a/W = 0$, for PE material 51
3.2 Uncracked compliance of arc-shaped specimens from pipes of various geometries, C_0EB 54

4.1 S4 Critical Temperature Values (°C) 71
4.2 Extrusion information 72
4.3 S4 Critical Temperature Values (°C) 75

5.1 Molecular Characteristics of C-Series PE Resins 89
5.2 Molecular Characteristics of D-Series PE Resins 104
5.3 Brittle-tough Transition Temperature values of D-Series PE Resins 107
5.4 Molecular Weight information of Polymer Resins 107
5.5 Effect of structural changes on ISO CD 17281 Impact Bend Test parameters 111

6.1 Effect of structural changes on Reversed Charpy test parameters . . 126
6.2 Determination of plane stress plastic zone size and the percentage of plane stress fracture resistance 127

7.1 Eyring rate constants for the HT model parameters 158
7.2 Effect of structural changes on Tensile test parameters 169
7.3 Base data used for sensitivity analysis 169
7.4 Eyring rate constants for the HT model parameters 172

8.1 Effect of structural changes on test parameters 177

Chapter 1

Introduction

The continuous growth of mankind no longer allows settling close to natural resources, so that transporting goods has become an important issue. When it comes to transporting fluids, pipelines are the most efficient, quick and economical way. Historically, pipes have been made of various materials including concrete, clay, metal and plastic. The first pipes made out of stone or clay were replaced by metal ones (which included steel, cast iron, ductile iron or aluminum) and recently, research has been directed to the use of plastics as piping materials. For most low-pressure pipe systems, thermoplastics are now the material of first choice.

Various factors are taken into account when it comes to choosing a pipe material. From durability and structural performance over time to fitting issues such as integrity of joints, hydraulic performance, ease of construction and availability; many aspects play an important role and are investigated in the search for an optimum material. The introduction of new polymers to the pipe industry is aiming to overcome various issues in this area through the continuous development of resin types.

Because some thermoplastic polymers tend to fail by fracture, the fracture resistance of plastic pipes in terms of their material properties and morphologies have been a topic of general interest for many researchers. The polymer suppliers seek a rational and economical way of comparing the toughness of their products, while

the pipe producers wish to translate toughness data into predictions of critical conditions. The ultimate goal is to find a common point that would satisfy both criteria.

The main aim of this project is to investigate the effect of structural parameters on the fracture properties of the plastic pipe material, while trying to develop test techniques for the ranking of materials. Pursuing this aim, materials differing in their overall structure, density, crystallinity, molecular weight, carbon black content and thermal history have been tested by performing S4 tests in addition to Instrumented Charpy, Reversed Charpy and Tensile Tests. Materials are characterised taking various aspects of fracture behaviour into account, and a new technique of analysing tensile tests to explain plane stress resistance is proposed. Each test method is considered in a separate chapter after the basic polymer chemistry and fracture mechanics definitions have been introduced.

1.1 Use of PE in the Pipe Industry

Having their origins in basic chemical elements such as carbon, oxygen, hydrogen, nitrogen, chlorine, or sulphur; plastic materials have been continuously improving through the discoveries in polymeric materials as shown in Fig. 1.1.

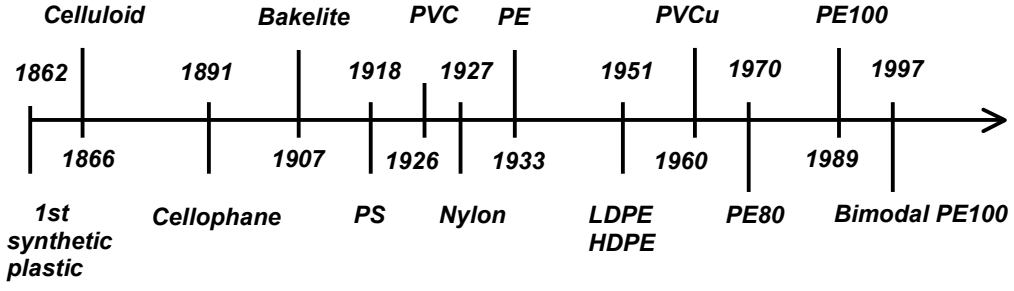


FIGURE 1.1: Timeline of Polymer Discoveries

When it comes to piping applications, polyethylene (PE) is often preferred because of its unique combination of strength and flexibility when compared with its main competitor, polyvinyl chloride (PVC). Its excellent toughness and flexibility

guarantees that PE pipe applications will continue to grow not only in terms of functionality, but also in terms of the processes for which it can be used [8, 9]. Studies in this area in combination with developments in the catalyst polymer technology area improve pipe performance continuously [10].

Pipe materials are generally classified on the basis of a minimum required strength (MRS), which is the long term hydrostatic strength extrapolated to 50 years life at 20°C. Pipes made from PE that have an MRS of 10.0 MPa are referred to as PE 100, while those having an MRS of 8.0 MPa are referred to as PE 80 [11]. Apart from material properties, geometry is another parameter for classifying pipes. Standard Dimension Ratio (SDR) standing for the ratio of outside diameter to wall thickness is used for this purpose and together with MRS this determines pressure capacity.

1.2 Defining Failure Characteristics and Transition behaviour

The two basic fracture possibilities for a pipeline system are *rapid crack propagation* (RCP) and *slow crack growth* (SCG). While rapid crack propagation could at any time immediately affect a significant length of pipeline, slow crack growth is a long term failure mode resulting in a local failure.

This study covers the RCP aspect, which has been an active research field during the recent years. RCP involves a long crack extending axially along the pipe length at speeds greater than 100 m/s. During RCP, the rapid escape of compressed gas or water may cause severe and costly damage to surrounding areas (*eg.* roads).

To be able to overcome such a disaster, it is necessary to predict and understand the underlying mechanism of fracture behaviour. The resistance and the ability of a polymer to exhibit plastic deformation and resistance to a load without failure, depends on temperature, pressure, load type and material properties such as

molecular weight, polydispersity, packing, chain entanglements, crystallinity and heterogeneity.

Most thermoplastic polymers are able to behave in either a ductile or a brittle manner. At some temperature, depending on the structure and morphology of the polymer, test type, speed or other energy input, the polymeric material undergoes a transition called brittle-tough transition temperature, T_{BT}. Transition behavior can be explained using the idea of a competition between fracture stress and yield stress and the type of failure is determined by the limiting stress that is reached first [12]. This brittle-tough transition is a subject of major interest of research on the mechanical properties of polymers including this current study.

1.3 Thesis Outline

- Chapter 2 gives a background on PE material defining the structural parameters that play an important role in determining the material's performance.
- Chapter 3 reviews the basic fracture mechanics concepts and includes a study of geometry factor determination calculations for arc-shaped specimen geometries used in this project.
- Chapter 4 introduces the S4 pipe test for RCP, presents results and discusses the effect of processing and extrusion conditions on pipe performance.
- Chapter 5 discusses Instrumented Charpy test and the parameters affecting impact fracture resistance (G_c) and brittle tough transition temperature (T_{BT}).
- Chapter 6 includes the measurement of plane stress fracture resistance via Reversed Charpy test and the effect of structural parameters on the results.
- Chapter 7 reviews basic Tensile Test definitions and deformation mechanisms, introduces a new approach for the analysis of the test results from which a good correlation is found between Reversed Charpy and Tensile Test results.

- Chapter 8 presents the main conclusions of the study in addition to the recommendations for the future work.

Chapter 2

Review of Polyethylene Structure

Polyethylene copolymers differing in their density, crystallinity, molecular weight and carbon content have been the main subject of this study. Before moving on to the effects of the material properties on pipe performances, in order to interpret the meaning of these results, the basic concepts regarding the structure will be reviewed.

2.1 Structure of Polyethylene

Like all other types of polymers, characteristics of PE depend upon the arrangement of the molecular chains. PE is made by the linking of thousands of monomeric units of ethylene (Fig. 2.1). Regardless of the polymerisation type, the chemical reaction is always the same but structural variation can be introduced by growing *long* side chains of the same structure, or *short* chain branches constructed from a comonomer as shown in Fig. 2.2 [1, 13].

The degree of chain branching is an important factor affecting the density and crystallinity of polymers. The number and length of branches are controlled by the type and parameters of the polymerisation process (temperature, pressure, type and amount of catalyst or initiator and of comonomer, *etc.*), and affects the ability of the polymer to crystallise. Branch points prevent the polymer chains

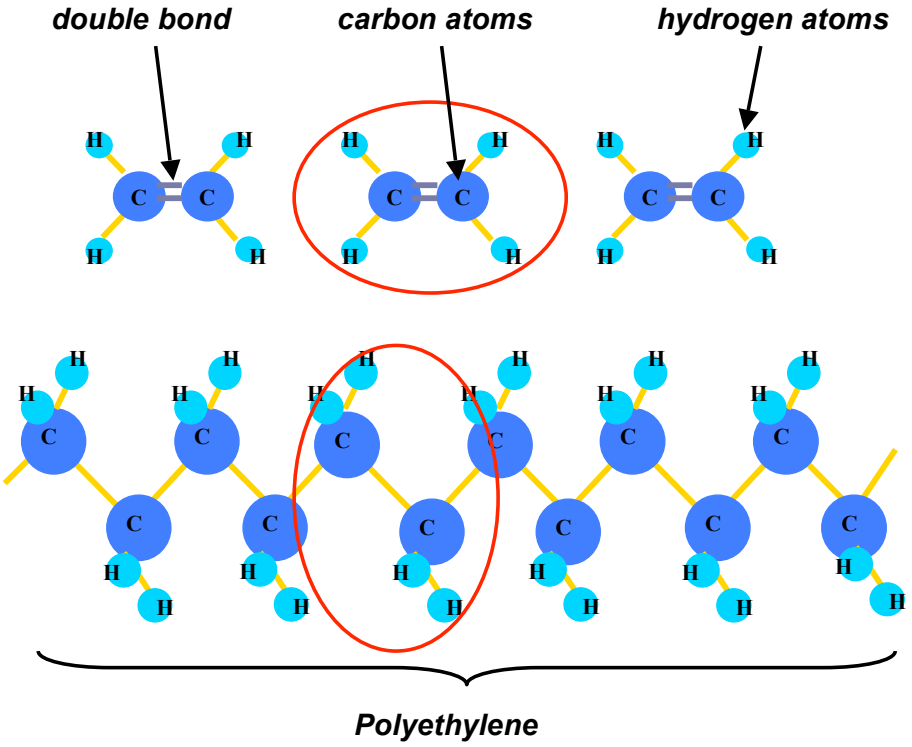


FIGURE 2.1: Polyethylene Formation

from packing together regularly and closely, and as a result have a predominant effect on the density of PE. Based on this, density can be considered as the first indication of the degree of branching, implying that the lower the density the higher the degree of branching [13, 14, 15].

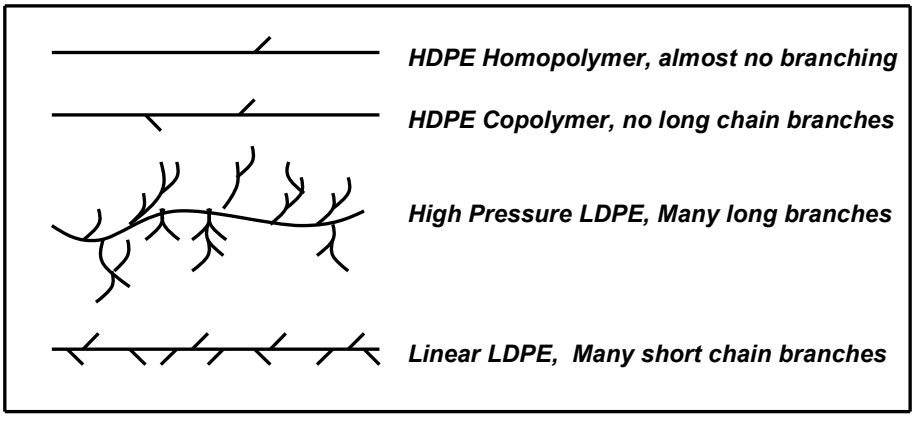


FIGURE 2.2: Chain structure of Polyethylene

The number, size and type of these side chains also determine the properties

of stiffness, tensile strength, flexibility, hardness, brittleness, elongation, creep characteristics, and melt viscosity of PE pipes.

2.2 Molecular Weight

The size of a polymer chain is represented by its molecular weight, whose importance comes from its great influence on the processability and the final physical and mechanical properties of the polymer (*eg.* durability).

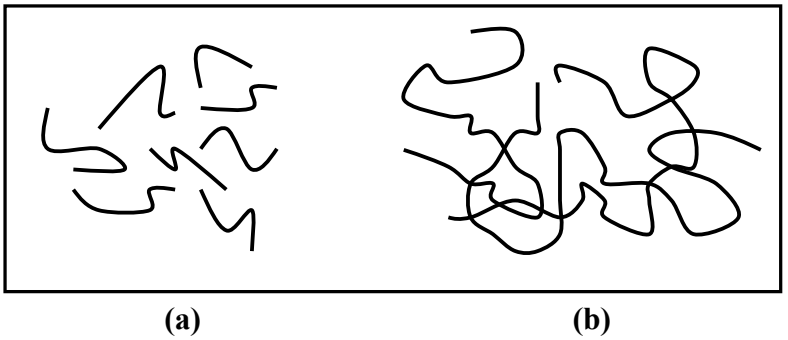


FIGURE 2.3: Entanglement of polymer chains (a)Low molecular weight, no entanglement (b) High molecular weight, chains are entangled

Molecular weight is controlled during synthesis by the catalyst, conditions of polymerisation, and type of the process used. Not all molecules grow to the same length and the molecular weight is usually expressed as an average value. There are various ways to express average molecular weight, but the most common is the number average,

$$M_n = \frac{Total\ weight\ of\ all\ molecules}{Total\ number\ of\ molecules} = \frac{\Sigma w_i}{\Sigma n_i} \tag{2.1}$$

and weight average,

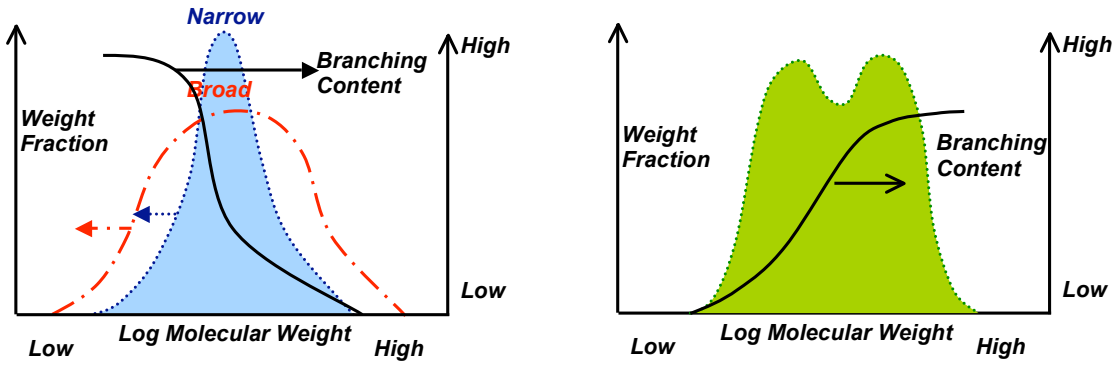
$$M_w = \frac{(Total\ weight\ of\ each)(Respective\ weights)}{Total\ weight\ of\ all\ molecules} = \frac{\Sigma w_i M_i}{\Sigma w_i} \tag{2.2}$$

where M_w is always larger.

In the case of long chain lengths at high molecular weights, entanglements are observed (Fig. 2.3). These are the main factors holding the material together under the application of stress. As to give an example, the increase in the entanglement density results in a reduction in the mobility leading to a lower draw ratio (ratio between the final and initial length of the material) and higher strain hardening (increase in the strength of material due to plastic deformation) [16, 17, 18].

2.2.1 Molecular Weight Distribution & Branching: PE 80 *vs.* PE 100

In PE 80, the low MW fraction of the material contains the highest branching which disappears as the MW increases (Fig. 2.4(a)). Most PE 80 materials are unimodal, having a single peak in molecular weight distribution (MWD) which can be narrow or broad depending on the grade. A polymer having narrow MWD means that it contains molecules that are nearly the same in molecular weight, resulting in a higher and more uniform rate of crystallisation. On the other hand, a polymer that contains a broader range of chain lengths, from short to long, is said to have a broad MWD. Resins of this type have good Environmental Stress Crack Resistance (ESCR), good impact resistance, and good processability due to the combined advantages of different chain lengths [2].



(a) PE 80 (b) PE 100

FIGURE 2.4: MW and chain branching distribution in unimodal PE 80 and bimodal PE 100

PE 100 was the first bimodal polyethylene developed [19] and its being bimodal comes from its polymerisation process including two stages resulting in a two-peak distribution. Having this structure, PE 100 benefits from the advantages of both parts in terms of ease of processibility due to low molecular weight sections and high impact toughness due to high molecular weight sections including tie molecules and entanglements [20]. Contrary to the behaviour of PE 80 resins, which tend to concentrate branching in low molecular weight fractions, PE 100 has a high degree of short chain branching in high molecule weight fractions. Having more branching on the longer chains forces them into the amorphous region of the polymer and thus increases the probability that they will act as tie molecules, holding the semi-crystalline polymer matrix together. In this manner the strength of polymer is greatly improved in many ways [10].

2.3 Crystallinity

PE is a semi-crystalline polymer, made up of both crystalline regions that are highly ordered, layered and densely packed, and amorphous regions that are tangled molecular chains, randomly arranged with lower density (Fig. 2.5). Since the density of a semicrystalline polymer is a measure of the proportion of crystals within its mass, the actual crystal density being less than that of a perfect crystal indicates that in PE, perfect crystals do not exist and that some amount of amorphous polymer is present between them. Polymers cannot be 100% crystalline for kinetic reasons, since their molecules cannot disentangle and line up properly in a finite period of cooling or annealing.

Various models have been proposed to explain the arrangement of molecular chains in polymers. One early model, accepted for many years, is the *fringed-micelle* model. This model proposes that a semicrystalline polymer consists of small crystalline regions, each having a precise alignment, which are firm within the amorphous matrix composed of randomly oriented molecules (Fig. 2.6). The chains wander from the amorphous region through a crystallite, and back out into the

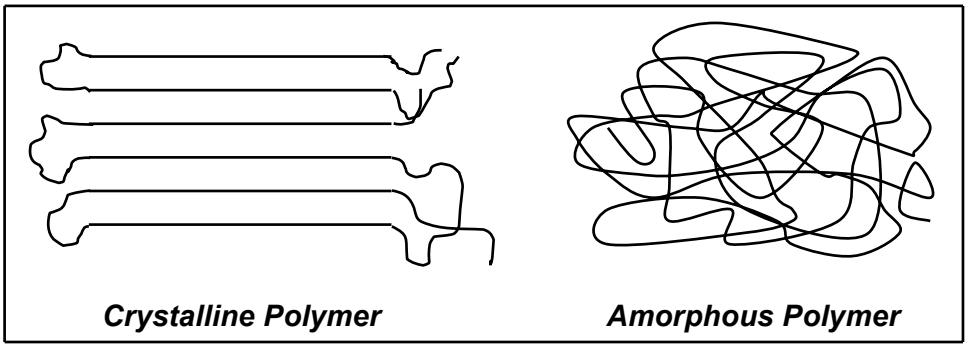


FIGURE 2.5: Crystallinity in Polyethylene

amorphous region. The chains are long enough to pass through several crystallites, binding them together. Thus a single chain has different crystallinity regions as well as amorphous regions. This model explains the behaviour quite well if the amount of crystallised material is less than about half [14].

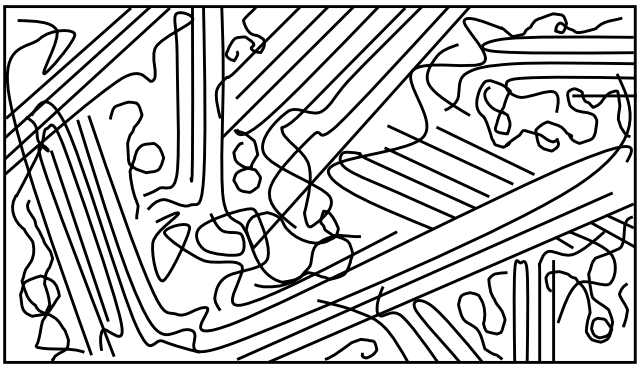


FIGURE 2.6: Fringed-micelle model of crystallites in amorphous matrix [1]

Crystals grown from dilute solutions: Single Crystals

For the case of highly crystalline polymers such as polyethylene, investigations are centered on polymer single crystals grown from dilute solutions in which the molecules are isolated from one another. Well-defined polymer crystals that can only be obtained in this way, are regularly shaped thin platelets (or lamellae) of approximately 10 to 20 nm thick [1, 21]. The most important parameter affecting

the thickness of a lamella is temperature. The degree of undercooling, ($\Delta T = T_m$-T_c, where T_m is the melting temperature and T_c the crystallisation temperature) also determines the number of nuclei [14] present in the solution.

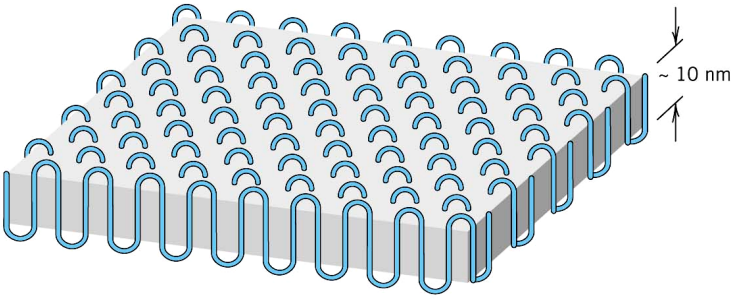


FIGURE 2.7: The chain-folded structure for a plate-shaped polymer crystallite [1]

Since most molecules are many times longer than the lamellar thickness, it was thought that they must be folded back and forth many times on a plane perpendicular to the surface of the lamellae. In order to explain this phenomena, Keller [22] proposed *the chain-folded* model, which states that thin plates or lamellae are formed with molecules ordered through the thickness by chain folding as seen in Fig. 2.7. Another model, *switchboard model*, proposed by Flory [23], suggests that the chains do not have a reentry into lamella by regular folding; they rather reenter more or less randomly [14]. Although it is generally agreed that folding takes place [3, 21, 22, 23], there is no clear conclusion on the mechanism of folding which is why additional studies are required in the area.

Crystallisation from melt: Spherulite Structure

In the case of crystallisation from dilute solution, the polymer coils are isolated from each other aggregating lamellar crystals as explained before. But in a melt, chain entanglements are of extreme importance and consequently, the crystals that form are more irregular than those obtained from dilute solutions. The chains, which are random and entangled in the viscous liquid, must assume an ordered configuration. For this to occur, sufficient time must be allowed for the chains

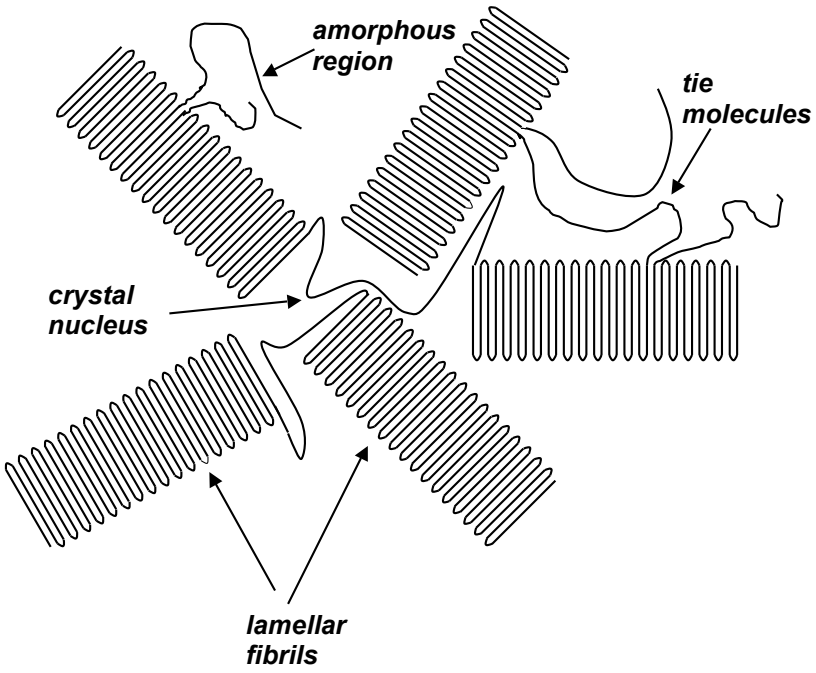


FIGURE 2.8: Polymer crystalline spherulite

to move and align themselves. That is the reason why slow cooling enhances the crystallinity of the material.

In many bulk polymers that are crystallised from a melt, the lamellae form *spherulites* (Figs. 2.8 - 2.9). These spherulites nucleating as a stack of lamellae grow at different points within a sample. They contain ribbon-like chain-folded crystallites that radiate from center to outward which are separated by amorphous material. Tie-chain molecules act as connecting links between adjacent lamellae and pass through the amorphous regions as shown in Fig. 2.8. Spherulites maintain their spherical shape till they start to impinge on one another towards the completion of crystallisation.

Spherulitic growth is highly dependent upon the polymers molecular weight, and it was observed that as molecular weight goes up, spherulitic radius goes down [24]. During the studies on HDPE, only early stage spherulites were observed [24], where in the case of PE 100 only one out of four resins have been found to develop spherulitic structure [25]. This can be explained by the fact that, in PE 100, the existence of high number of branches, entanglements and tie molecules resist any

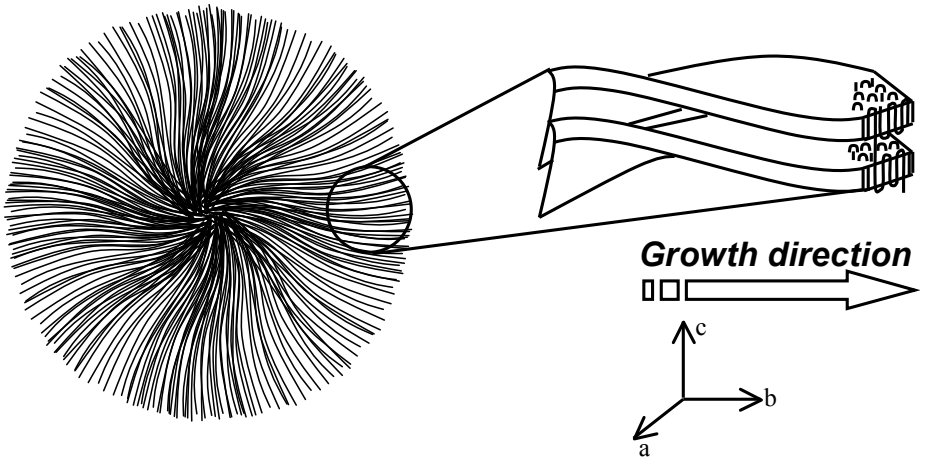


FIGURE 2.9: Polymer crystalline spherulite [2]

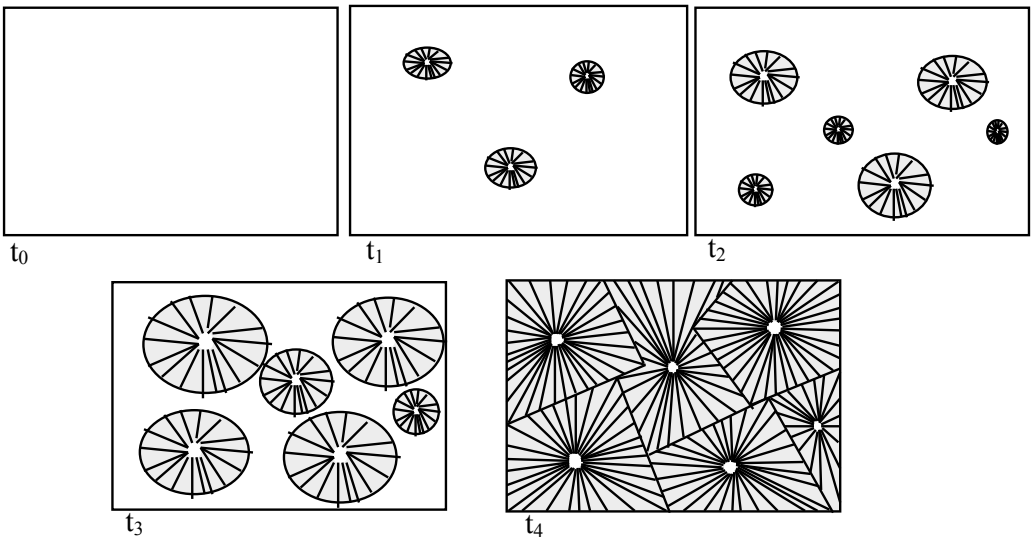


FIGURE 2.10: Stages of spherulitic growth during melt crystallisation of PE [3]

degree of order and this makes it more difficult for a fully developed spherulite to appear when compared with HDPE [2].

To sum up, although spherulitic growth can be developed in some PE 100 under slow cooling conditions, it can be said that in most of the materials studied so far, spherulites did not appear and when they did it was under slow cooling conditions. Transferring the argument to the pipes, and taking in to account that especially in small diameter pipes cooling is relatively quick, it can be concluded that the possibility of finding spherulites is even smaller. Only in large diameter pipes,

above 400mm, and with specific PE 100 materials, it may be possible to grow spherulites, but still the possibility is rare [2].

2.3.1 Degree of Crystallinity

Crystallinity χ_c, is defined as the mass fraction of the crystals in a semi-crystalline polymer. This can vary from 40 to 90 percent and is a parameter with a strong effect on the mechanical properties of the material. It is known [26] that quantities like yield stress (σ_y), Young's modulus (E), strain hardening modulus (G_P) and brittle to tough transition temperature (T_{BT}) have almost linear relationships with χ_c. Having the influence on these parameters, crystallinity itself depends on the molecular structure (chain configuration), molecular weight, branch content as well as the thermal history upon cooling from melt, such as the cooling rate and temperature.

While crystallisation is more easily accomplished for linear polymers, branched polymers are never highly crystalline and network polymers are almost totally amorphous. As a key, it can be said that the simpler the molecular structure, the easier for it to crystallise. Side chains, bulky side groups, branching and irregularity of the atomic alignment are the factors preventing crystallisation. For example, by decreasing the number of branches in PE, crystallinity changes from about 40% to 70% [21].

In linear PE, as molecular weight (MW) increases, crystallinity is found to decrease [27, 28]. Alamo and Mandelkern [21] have found that for a fixed branching content at isothermal conditions, lower molecular weight fractions crystallise more rapidly and grow more crystals than high molecular weight fractions. In the case of PE 100, even though the material is considered to be a high molecular weight polymer, its crystallinity can be quite high. This is due to the fact that PE 100 is bimodal and that its low molecular weight fraction crystallises rapidly.

Degree of crystallinity can be measured by several methods [14]. The first involves the determination of the heat of fusion of the whole sample by calorimetric methods

such as DSC (differential scanning calorimetry). In this method the difference in the amount of heat required to increase the temperature of a sample and reference are measured as a function of temperature. The second method is density based. It relies on the determination of the theoretical density of the crystalline portion via X-ray analysis of the crystal structure, and of the amorphous material by extrapolation of the density from the melt to the temperature of interest. Following this, the volume fraction crystallinity of a sample of density ρ_{x} can be determined by,

$$\%\chi_c = [\frac{\rho_x - \rho_a}{\rho_c - \rho_a}] \times 100 \tag{2.3}$$

where ρ_x is the experimantal density, and ρ_a and ρ_c are the densities of the amorphous and crystalline portions respectively.

The third method is the wide-angle X-ray scattering (WAXS) which uses the fact that the intensity of X-ray diffraction depends on the number of electrons involved and is thus proportional to the density.

When these methods are compared, the exact same answer is not obtained for a given sample, but a surprisingly good agreement is obtained [14].

2.3.2 Mechanism of Crystallisation

The molecules that make up polyethylene are in constant motion. There is enough free space within the polymer to allow local molecular movement even though the molecules are entangled. As the temperature falls below the melting point, T_m, also known as the crystallisation temperature, there is a decrease in molecular movement and volume [1].

In the case of rapid cooling, crystallisation is controlled by molecular kinetics and the rate at which crystals nucleate and grow becomes important as will be discussed in the following section.

Crystallisation itself consists of two stages; *nucleation* and *growth*. The first stage occurs during the cooling down of the molten polymer, where molecules start to

form the first crystals. Nucleation can either be homogeneous, when all nuclei form uniformly and randomly in the melt; or heterogeneous, when nuclei form around the impurities. At temperatures in excess of the melting temperature, these nuclei are unstable due to the thermal atomic vibrations that tend to disrupt the ordered molecular arrangements. The second stage occurs subsequently, when crystal nuclei grow by the increase in chain-folded layer of lateral dimensions or by the increase in the spherulite radius [1].

2.3.3 Kinetics of Crystallisation

The rate of crystallisation under different conditions of temperature, molecular weight, and structure have been investigated via different theories providing strong predictions in the area. It is observed that the rate increases as the temperature is decreased due to the increase in the driving force. These observations can be done microscopically by measuring the growth of the spherulites as a function of time. In order to explain this behaviour and to predict the mechanism, three different theories have been recognized in the polymer crystallisation kinetics field [13].

The first theory is based on the work of Avrami [29, 30, 31], which adapts the metallurgy formulations to polymers. The evolution of the degree of crystallinity is related to the time under isothermal conditions by,

$$\chi(t) = 1 - exp(-kt^n) \tag{2.4}$$

where n is the Avrami exponent describing the type of nucleation, growth control and geometry having a value between 1 and 4, and k the rate constant for the particular crystallisation process. Equation 2.4 manages to predict the initial portions of polymer crystallisation correctly but lacks providing information on the molecular organization of the crystalline regions.

The second theory was developed by Keith and Paden [32], and provides a qualitative understanding of the rates of spherulitic growth by taking the radial growth

rate of the spherulite into account without taking the thermodynamics and kinetics into account. The most recent theory was introduced by Hoffman [33], who developed a kinetic nucleation theory of chain folding, which provides an understanding of how lamellar structures form from melt. It is based on the change of Gibb's free energy during nucleation.

In a recent review by Mandelkern [27], it was surprisingly found that these complicated kinetic equations are not any better than the simplest free-growth theory introduced by Goler and Sachs [34], where each center starts growing independently once is initiated. The fact that there is no mechanism to terminate the transformation is a drawback of this model. But, this incomplete transformation does not affect the actual growing motion, so its predictions are not very different than Avrami's.

Chain entanglements and other topological defects have been shown to play a major role in influencing the course of crystallisation [21, 27, 28].

2.4 Glass Transition

Although the glass transition is not of interest to the current project, it is important to distinguish it from the ductile to brittle transition which will be referred to many times. In order to clarify the difference, the glass transition is briefly described here.

The glass transition occurs in amorphous regions, and is due to a reduction in motion of large segments of molecular chains with decreasing temperature. The temperature at which the polymer transforms from a rubbery to a rigid states is termed the glass transition temperature.

The basis of glass transition is the coordinated molecular motion in the polymer chain in an amorphous state. At low temperatures, where only vibrational motions are possible, the polymer is hard and glassy. In the glass transition region,

the polymer softens, the modulus of elasticity drops by about three orders of magnitude, and the amorphous glass becomes rubbery. The intermolecular forces, intrachain steric hindrance, and bulky side groups increase T_g, while flexible chain groups and symmetrical substitution decrease T_g [14].

2.5 Carbon Black Filler

Ultraviolet (UV) radiation can alter the physical and mechanical properties of polymers. The function of UV stabilizers is to inhibit the physical and chemical processes of UV-induced degradation. There are two separate issues when dealing with UV protection. The first is weatherability, which is defined as the capability of the resin to resist changes in the physical properties when exposed in an outdoor environment. The other parameter is the colour fastness [1].

The prime UV stabilizer used in the polyethylene pipe industry is finely divided *carbon black*, which is the most effective additive capable of stopping these UV-induced reactions, as well as being low in cost. Having a particle size ranging from 10 to 120 nm, its absorption of visible and UV light increases by decreasing particle size due to increase in the surface area [35].

Carbon black can affect mechanical properties such as tensile strength, impact strength, thermal conductivity, and other related properties of compounds depending on the morphology, loading of the carbon black in the compound and the dispersion of carbon black in the carrier resin.

2.6 Conclusion

One of the main objects of this study is to investigate the effect of structural parameters on the fracture properties of plastic pipe material. Based on this, in order to be able to interpret the experimental results correctly, some of the main structural parameters of pipe grade PE that are mentioned in the project

are introduced in this chapter. In the following experimental sections, the effect of density, molecular weight, crystallinity, and carbon black addition on the test parameters such as S4 critical temperature, impact fracture resistance, ductile to brittle transition temperature, yield stress and plane stress fracture resistance values will be investigated in detail on different groups of PE resins.

Chapter 3

Fracture Mechanics

Fracture can be defined as the creation of new surfaces within a solid body. It is different from deformation in the sense that it does not preserve the continuity of the material. Any component under load contains stored energy and fracture will occur only when the resulting release of this energy is sufficient to propagate an existing defect (crack or flaw), meaning that it is sufficient to overcome the fracture resistance of the material. The nature of these defects may be material based or may be a result of the post production damage, which can be microscopic or macroscopic in size. Therefore, the structural integrity of a given structure or a material depends on the level of applied stress, the presence and size of flaws and the resistance of the material to crack initiation and growth and the aim of fracture mechanics is to find a quantative relationship between these factors.

Fracture in polymers occurs by means of separation or disentanglement of the molecules at the tip of the propagating crack. If the fracture time and/or the test temperature are high enough for relaxation of the molecular structure, disentanglement is assumed to predominate, as in polymer melts. That is why, for pipes in the heating industry, the materials are cross-linked to reduce disentanglement at low stresses and high temperatures, resulting in extended life times [36].

Due to the wide range of fracture behaviours being observed in plastics, numerous fracture mechanics concepts have been proposed and applied to characterise the failure behaviour in terms of specific fracture parameters [37].

In this chapter, the basic concepts will be reviewed and arc-shaped geometry factor calculation for various pipe geometries is introduced.

3.1 Linear Elastic Fracture Mechanics, (LEFM)

The first approach, Linear Elastic Fracture Mechanics, (LEFM), assumes that the material is an isotropic and linear elastic solid until fracture occurs. This method can be used as long as plastic deformation is small compared to the size of the crack. It deals with plane strain and plane stress conditions associated with the three basic modes of loading (opening, sliding and tearing) on a cracked body and relates the crack driving force to the externally applied load and its displacement, or stress area.

3.1.1 Energy Based Analysis

Proposed by Griffith [38] for brittle materials, this method was developed by Irwin [39] and Orowan [12] independently, who applied Griffith's work to ductile materials by taking the plastic deformation energy into account. This approach states that the energy released during the fracture process is equal to that required to create two new surfaces in a thermodynamically irreversible manner. By applying an energy conservation approach to the fracture of an elastic body, the difference between the energy given to the system (U_1) and the energy dissipated (U_2) within it can be related to the change in the potential (U_p) and kinetic energy (U_k) of the system (Fig. 3.1) by,

$$\frac{\delta U_1}{\delta A} - \frac{\delta U_2}{\delta A} = \frac{\delta U_p}{\delta A} + \frac{\delta U_k}{\delta A} \tag{3.1}$$

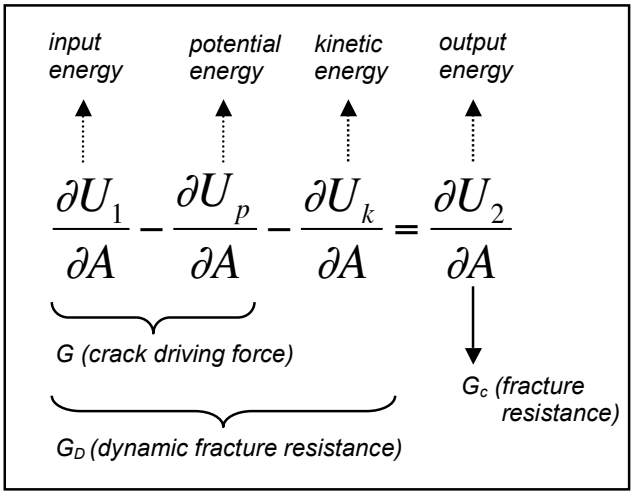


FIGURE 3.1: Energy Based Analysis Definitions

The energy dissipated by the system can also be defined as the fracture resistance, G_c,

$$G_c = \frac{\delta U_2}{\delta A} \tag{3.2}$$

And the energy release rate which provides the crack driving force, G, can be defined as,

$$G = \frac{\delta U_1}{\delta A} - \frac{\delta U_p}{\delta A} \tag{3.3}$$

At low rates where kinetic terms can be neglected, $G = G_c$, but in the case of RCP, the kinetic term is significant and G_D is defined standing for dynamic fracture resistance, is defined as,

$$G_D = \frac{\delta U_1}{\delta A} - \frac{\delta U_p}{\delta A} - \frac{\delta U_k}{\delta A} = \frac{\delta U_2}{\delta A} \tag{3.4}$$

G_D is the work which must be supplied to a fast-running crack front to separate a unit area of material and is a function of crack speed. While G_D is defined for the case of a running crack in a dynamic case, G_c is related to the load at initiation and is a quasi-static parameter. Taking a linear-elastic cracked plate of thickness B, subjected to load P, G can be defined by,

$$G = P\frac{du}{dA} - \frac{\delta U_p}{\delta A} \tag{3.5}$$

where u is the displacement of the load-application point. This reduces to,

$$G = \frac{1}{2}P^2\frac{dC}{dA} = \frac{1}{2}\frac{u^2}{C^2}\frac{dC}{dA} \tag{3.6}$$

where C is the compliance defined as displacement per load (u/P). Further rearrangement of terms will lead to,

$$G = \frac{U}{CBW}\frac{dC}{d(a/W)} = \frac{U}{BW\phi(a/W)} \tag{3.7}$$

where a is the crack length, U is the elastic energy stored and ϕ is the geometry factor defined as,

$$\phi = \frac{C}{dC/d(a/W)} \tag{3.8}$$

3.1.2 Stress Based Analysis

The second approach to the fracture problem deals with the mechanical environment near the tip of a flaw, which will initiate a growing crack. It is based on the analysis of the stress state near the tip of a sharp crack requiring either load-displacement record or directly measured critical energy values [37].

Irwin states that the stress concentration around a sharp crack tip in an elastic body can be characterised by a Stress Intensity Factor, K, which is,

$$K = Y\sigma\sqrt{a\pi} \tag{3.9}$$

where Y is a dimensionless parameter that depends on both the crack and specimen size and geometry, as well as the manner of load application, σ is the applied stress and a is the crack length. The stress intensity factor, K, is used in design by taking the critical value term K_c, which depends on the material of the specimen, as a limiting criterion. Crack growth is assumed to occur when the value of K that exists in the stressed specimen exceeds this critical value, K_c.

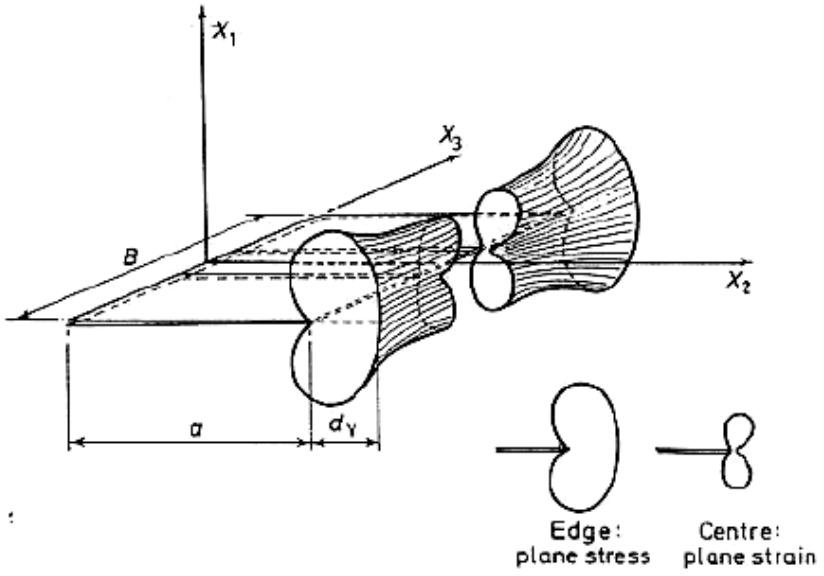


FIGURE 3.2: Plastic zone ahead of crack in a plate of finite thickness [1]

3.1.2.1 Plane Stress *vs.* Plane Strain

There are two extreme cases for a crack front under loading: plane stress and plane strain conditions. In *plane stress* conditions, principal stresses are always parallel to the given plane and are uniform or zero in the normal direction. This occurs in relatively thin bodies where the stress through the thickness cannot vary appreciably due to the thin section. However, the region of the material that is away from the free surface of a relatively thick component is not free to deform. The stress state under these conditions is *plane strain*. Under these conditions, the displacements in the body are parallel to its plane and they do not depend on the distance perpendicular to the plane.

The elastic stress field around a sharp crack tip can be used to trace the boundary of the plastic zone within which a chosen shear-yield criterion is satisfied. The radius of the plastic zone, r_p, can be estimated for a Von Mises criterion from the uniaxial yield stress, σ_y, by,

$$r_p = \frac{1}{2\pi}\left(\frac{K}{\sigma_y}\right)^2 \tag{3.10}$$

in plane stress conditions. For plane strain conditions,

$$r_p = \frac{1}{6\pi}\left(\frac{K}{\sigma_y}\right)^2 \tag{3.11}$$

applies. The smaller value of r_p under plane strain conditions (Fig. 3.2) is consistent with the fact that the triaxial stress field limits the amount of plastic deformation [2]. The material remains relatively elastic until the fracture stress is reached.

The criterion for the specimen thickness required to satisfy plane strain condition is,

$$B \geq 2.5\left(\frac{K_c}{\sigma_y}\right)^2 \tag{3.12}$$

where σ_y is the materials yield stress. Depending on the stress states at the crack tip, K and G parameters are interrelated by,

$$K^2 = GE \qquad (\textit{plane-stress}) \tag{3.13}$$

$$K^2 = \frac{GE}{1-\upsilon^2} \qquad (\textit{plane-strain}) \tag{3.14}$$

where υ is the Poisson's ratio and E is the Young's Modulus.

3.1.2.2 Determination of plane strain and plane stress fracture resistance

Experimentally, the *plane strain dynamic fracture resistance*, G_D, of a material can be determined by the high speed double torsion test (HSDT) [40] or using the hydrostatic S4 test (which uses a water-pressurised pipe) [9, 41]. The *impact fracture resistance*, G_c can be determined using instrumented impact bend test, ISO CD 17281, which is a form of Instrumented Charpy test.

In the case of Instrumented Charpy testing, the fracture analysis for the determination of G_c is valid for a brittle fracture mode and any elements of ductility

influencing test results should be discarded in order to obtain valid fracture toughness values. In this study the initial tests performed on specimens having the dimensions of $12(B) \times 12(W) \times 70(l)$ mm (as given in Fig. 3.3) showed traces of shear lip formation on the edges. In order to control and eliminate the formation

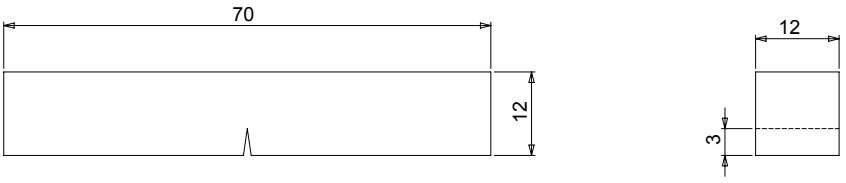


FIGURE 3.3: Rectangular Plaque Specimen

of these shear lips and promote plane strain fracture conditions, the *side-grooving* technique has been used. Extensive studies have been done by Youd [42] on the

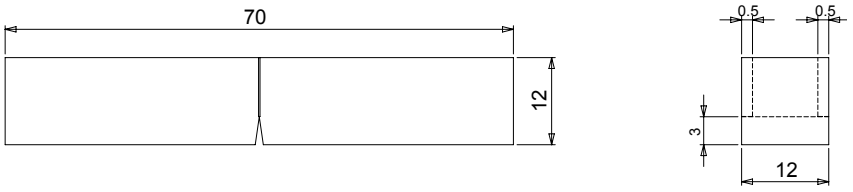


FIGURE 3.4: Side-grooved specimen

sharpness and the size needed for these side grooves and for a PE specimen having dimensions of 12 mm (W) $\times$ 12 mm (B), 0.5 mm side grooving is suggested.

Based on this, by notching the specimens with a razor blade perpendicular to the impact direction, 0.5 mm, down the width of the sample at both side of the notch (Fig. 3.4), the shear lips are eliminated. For the calculations, the corrected width of the specimens was taken into account according to,

$$B_{\text{effective}} = \sqrt{B \times B_c} \tag{3.15}$$

where B is the original width of the specimen, and B_c is the width remaining after side notches. In Chapter 5, the results from these side-grooved samples are compared with those from standard notched ones to see the effect of shear lip resistance during impact.

On the other hand, the measurement of *plane stress* fracture requires the removal of plane strain regions, so that the shear lips can be studied in isolation. For this project, a detailed study of shear lips and plane stress effects was undertaken using the Reversed Charpy Test, which will be introduced in Chapter 6.

3.1.2.3 Prediction of plane stress and plane strain fracture resistance

Apart from experimental methods, the *thermal decohesion model* proposed by Leevers [43, 44, 45, 46] can be used to predict impact fracture resistance parameters. Although not being the main subject of this study, the thermal decohesion model will be briefly explained since it helps to develop an insight about the relationships between the fracture resistance parameters and material properties.

This model allows the prediction of resistance to the initiation and rapid propagation of brittle fracture from bulk material properties by proposing that fast crack fracture in semi-crystalline thermoplastics occurs by adiabatic decohesion of the fibrillated region, or craze, ahead of the moving crack. As a craze is formed, fibrils are drawn from the adjacent bulk material and plastic work is dissipated as heat. In the case of rapid plastic deformation, drawing fibrils causes intense local heating, and even melting in extreme cases [47].

Propagation conditions (plane strain dynamic fracture resistance, G_D)

The model predicts a steeply falling G_D as crack velocity increases towards a transition value. Between the low speed (isothermal) and high speed (adiabatic) conditions, at which crack resistance is high, lies a broad, flat minimum with a value of [46]:

$$G_{D-min} = \rho \overline{s}_w [5C_p(T_m - T) + 2\Delta H_f] \tag{3.16}$$

where $\overline{s}_w$ is the weight average chain contour length, ρ is the mass density, C_p is the specific heat, T_m is the melting temperature, and ΔH_f is the latent heat of fusion.

Initiation conditions (impact fracture resistance, G_c)

G_c, being the instantaneous rate of energy flow to a crack tip at the moment of the start of rapid propagation, is related to the load at fracture initiation. The resistance to impact fracture initiation is generally greater than that to propagation and can also be predicted using adiabatic decohesion model, by applying it to predict instability of an extending craze under impact. Using heat conduction analysis, assuming plane stress conditions, the following equation is obtained [44],

$$G_c = E^{-1/3}(\pi\kappa)^{2/3}[\frac{3}{2}\rho C_p(T_m - T)]^{4/3}\psi(\alpha)W^{1/3}\dot{v}^{-2/3} \tag{3.17}$$

where E is the tensile modulus, κ is thermal diffusivity, $\psi(\alpha)$ is a dimensionless geometry factor and $\dot{v}$ is the load point impact speed.

Further details of this model can be found in the literature [43, 44, 45, 46].

3.1.3 Geometry Factor Determination for Arc-Shaped Geometry

The experimental determination of correct G_c values depends on the precision of the parameters in Eq. 3.7. For this, the geometry factor, ϕ, needs to be determined so as to reflect the correct geometry of the sample. For the case of rectangular SEN(B) specimens, ϕ values are given in the literature [48]. However in this study, it was necessary to test arc-shaped specimens (Fig. 3.5) directly cut out from pipe, enabling us to measure the properties of the materials in the state subject to RCP behaviour in the field. It was suspected that for the arc-shaped geometry, the geometry factors were not well enough established.

In this study ϕ was determined using the LEFM approach equations in combination with FEM analysis done by Argyrakis [49], and the results were validated by experimental measurements.

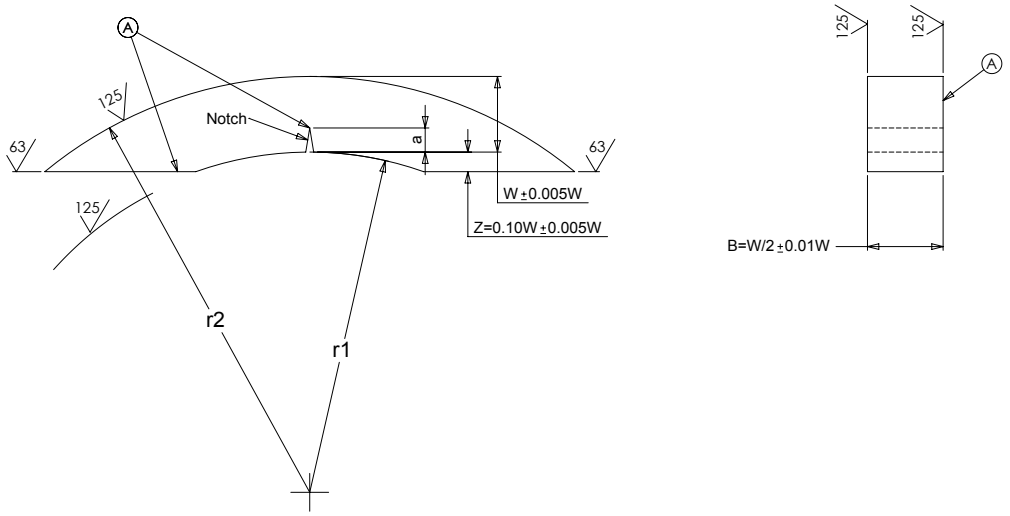


FIGURE 3.5: Standard arc-shaped geometry as suggested by ASTM 399-90

3.1.3.1 Derivation of Equations

As given in Eq. 3.8, for the calculation of ϕ, it is necessary to compute the compliance factor first. From Eq. 3.9 and 3.13,

$$K^2 = E'G = Y^2\sigma^2 a\pi \tag{3.18}$$

where E'=E in plane stress conditions, and E'=$E/(1-\upsilon^2)$ in plane strain conditions. Relating Eq. 3.6 and 3.18,

$$E\frac{P^2}{2B}\frac{dC}{da} = Y^2\sigma^2 a \tag{3.19}$$

can be obtained. Since a constant relationship exists between the remote stress (σ) and applied load (P) for any given geometry, σ/P can be defined as α/BW, where α is a dimensionless constant. For the SEN(B) specimen, the remote stress can be defined as the surface stress [50] so that

$$\alpha = \frac{3}{2}\frac{S}{W} \tag{3.20}$$

where S is the span and W is the width of the specimen. Rearranging Eq. 3.19,

$$\frac{dC}{d(a/W)} = \frac{2\alpha^2}{BE} Y^2(a/W) \tag{3.21}$$

can be obtained and compliance can be calculated by integrating Eq. 3.21,

$$C = \frac{2\alpha^2}{EB} \int Y^2(a/W) d(a/W) + C_0 \tag{3.22}$$

where C_0 is the integration constant, representing the uncracked compliance that can be found through finite element analysis or experimental measurements. By combining Eq. 3.8 and 3.22, ϕ can be expressed as,

$$\phi = \frac{C_{\text{int}} + C_0}{dC/d(a/W)} \tag{3.23}$$

where C_{int} stands for,

$$C_{\text{int}} = \frac{2\alpha^2}{EB} \int Y^2(a/W) d(a/W) \tag{3.24}$$

Following ASTM E 399-90 for arc-shaped geometries, K can be determined by,

$$K = \frac{PS}{BW^{3/2}} [1 + (1 - r)(h(a/W)] f(a/W) \tag{3.25}$$

where r is the ratio of the inner to outer diameter of the pipe, and $h(a/W)$ and $f(a/W)$ are the geometrical correction factors. These factors are provided in the standard for differing S/W ratios as given below:

- For S/W=3;

$$h_1(a/W) = 0.29 - 0.66(a/W) + 0.37(a/W)^2 \tag{3.26}$$

$$f_1(a/W) = [0.677 + 1.078(a/W) - 1.43(a/W)^2 + 0.669(a/W)^3]/(1 - a/W)^{3/2} \tag{3.27}$$

- For S/W=4;

$$h_2(a/W) = 0.20 - 0.32(a/W) + 0.12(a/W)^2 \tag{3.28}$$

$$f_2(a/W) = [0.644 + 1.11(a/W) - 1.49(a/W)^2 + 0.73(a/W)^3]/(1 - a/W)^{3/2} \tag{3.29}$$

From Eq. 3.18 and 3.25, one can define Y by,

$$Y = \frac{2}{3}(\frac{a}{W})^{-1/2}[1 + (1 - r)(h(a/W)]f(a/W) \tag{3.30}$$

3.1.3.2 Calculation of Integral and Derivative expressions using Matlab and Maple

Substituting $h(a/W)$ and $f(a/W)$ expressions into Eq. 3.30, and then into Eq. 3.22, C_{int} and $dC/d(a/W)$ can be determined by carrying on the calculations symbolically in Maple and Matlab Software Programs (the results obtained from each program were found to be in perfect agreement).

3.1.3.3 Determination of the Integral Constant (C_0) using ANSYS

C_0 can be determined from an unnotched arc-shaped specimen by taking the ratio of applied load to the corresponding displacement. Having many models in ANSYS, it is important to be able to choose the right condition representing the experimental case: the three point bend impact test case. For this current project, FEM analysis was undertaken by a colleague [49] in order to have a complete study combining empirical, experimental and modeling approaches.

It is important to choose a mesh which can reflect the real situation as precisely as possible. Initally, both rectangular and triangular elements (8-node) were used [49]. Varying the size of triangular elements was found not to have a significant effect on the compliance calculation, since this geometry can resemble the current

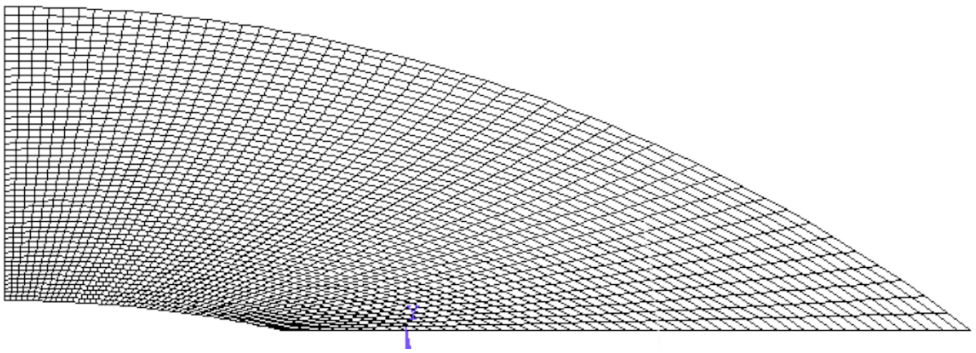
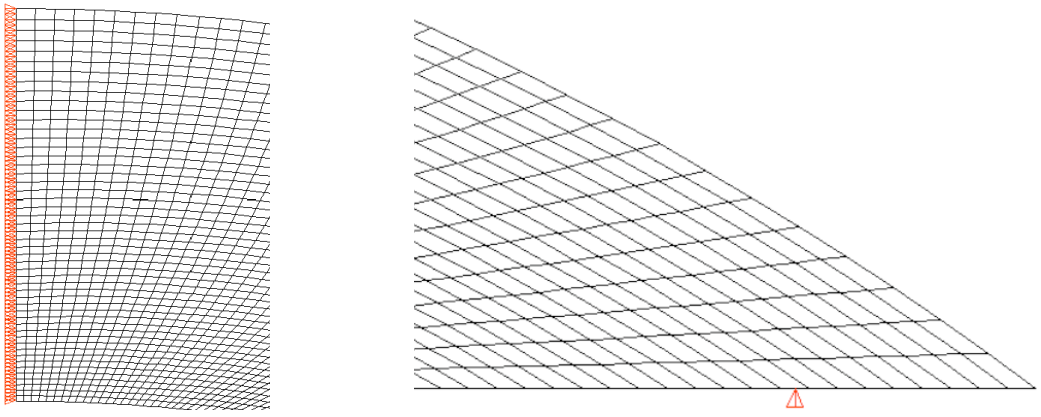


FIGURE 3.6: FEM Model of an unnotched arc-shaped specimen

geometry of the problem satisfactorily. On the other hand, the size of the rectangular elements affected the mesh sensitivity; the smaller the size of the rectangular elements, the better the model would fit, since having small element size enables the curvature section to be defined as close to reality as possible. Finally, it was decided to use a fine rectangular mesh, in order to have more integration points. When compared with the triangular case, the difference in the compliance values was observed to be less than 3% [49]. (The ANSYS model of the arc-shaped specimen is shown in Figs. 3.6-3.7).



(a) Impact point detail (b) Support detail

FIGURE 3.7: FEM model details

The validity of model conditions were tested using S/W=6 geometry, on an aluminium material with a known E (70 GPa). The experimental compliance is

found to be 74.2. Modeling the same case in ANSYS, with plane stress with thickness in the case of boundary conditions limited to 1 degrees of freedom (U_y), the compliance value is found to be 66.57.

The reason why the experimental compliance value is more than the model result can be explained by the fact that the compliance of the testing machine where the experiments were performed was also affecting the results. Although the loads and strains applied to the specimens were extremely low, the compliance of a testing rig using steel grips and impactors has an effect. Another reason might be the experimental samples not being as precise as the ones used in the model. In the model, the contact point is a single point, where in the experiment it is not as sharp and well defined. The point force applied can not be reproduced during experimental procedures. It was decided that the overall error can be neglected and this modeling condition can be used in confidence.

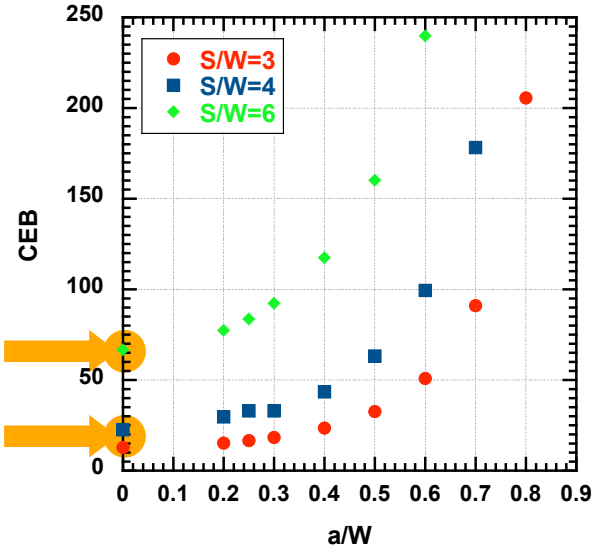


FIGURE 3.8: Compliance values obtained from ANSYS for PE, differing S/W ratios [49]

Based on this, PE is modeled in ANSYS and CEB values were determined for differing a/W values where the values corresponding to $a/W = 0$ were taken as the integral constants (Table 3.1) as shown in Fig. 3.8.

for $a/W = 0$	S/W=3	S/W=4	S/W=6
C_0EB	12.8	22.6	66.6

TABLE 3.1: Integral Constant values, C_0EB, $a/W = 0$, for PE material

3.1.3.4 Determination of ϕ

Combining and replacing all the values into Eq. 3.23, the geometry factor (ϕ) can be determined for S/W=3 and S/W=4 conditions.

Determination of ϕ for S/W=6

ϕ value of S/W=6 geometry can be determined through extrapolation (based on S/W=3 and S/W=4), as was suggested by Williams [48] for SEN(B) geometry. Figure 3.9 shows the extrapolated results.

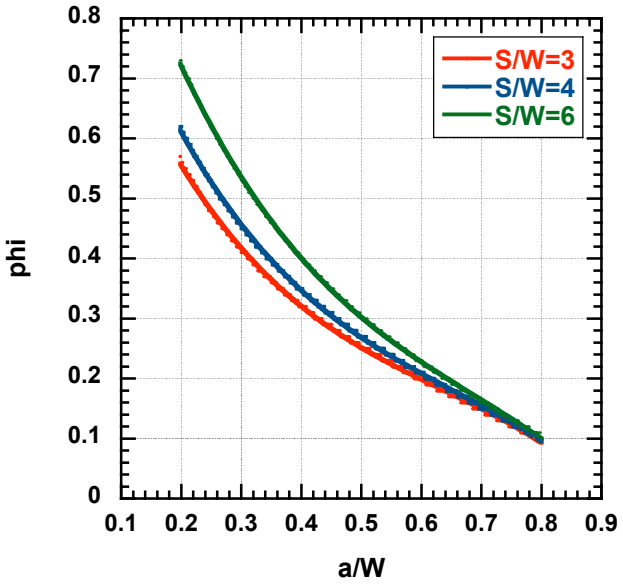


FIGURE 3.9: Geometry factor (ϕ) values determined for arc-shaped specimens

By fitting polynomials to these curves, equations for ϕ can be obtained, as given below (for the case of SDR 11, where B/W=1 and L=70 mm),

$$\textbf{S/W=3} \Longrightarrow \phi = -2.00(a/W)^3 + 3.80(a/W)^2 - 2.89(a/W) + 0.99 \qquad (3.31)$$

$$\mathbf{S/W{=}4} \Longrightarrow \phi = -2.05(a/W)^3 + 4.02(a/W)^2 - 3.15(a/W) + 1.09 \qquad (3.32)$$

$$\mathbf{S/W{=}6} \Longrightarrow \phi = -2.16(a/W)^3 + 4.44(a/W)^2 - 3.66(a/W) + 1.29 \qquad (3.33)$$

The idea of extrapolation was questioned since this was a suggested method for the case of SEN(B) geometry, and not for the arc-shaped geometry. In order to check the validity of this method's applicability, some further calculations were carried on by Argyrakis [49].

Defining the overall compliance (C) of S/W=6 with an equation (based on the ANSYS results given in Fig. 3.8), ϕ can be calculated by Eq. 3.23. The comparison of ϕ values obtained via extrapolation and ANSYS equation fitting methods is given in Fig. 3.10. As can be seen, these methods are in a very close agreement, reassuring that the extrapolation method is valid for this geometry as well.

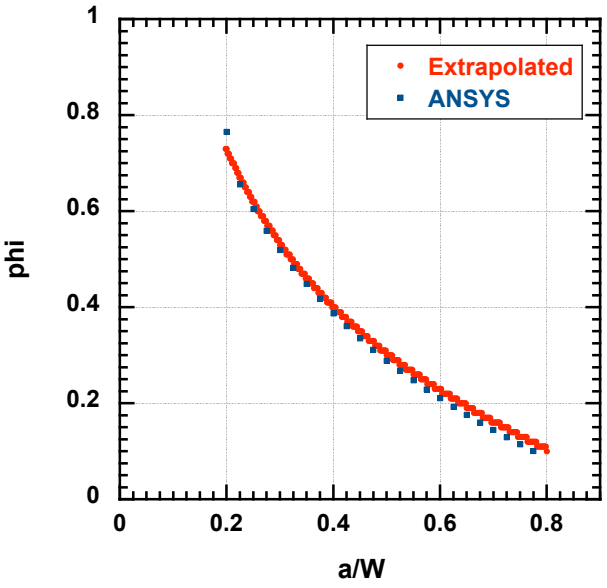


FIGURE 3.10: Checking the validity of extrapolations

When the geometry factors of rectangular SEN(B) specimens (taken from literature [48]) and the and arc-shaped specimens (based on the current findings) are compared, (for the case of S/W=6), it can be seen that arc-shaped specimens are more compliant (as shown in Fig. 3.11), and this leads them having a higher energy storage. So, in order to stop a crack in such a specimen requires more energy

absorption by the shear lips, effectively increasing the temperature of transition. These effects will be discussed further in Chapter 5.

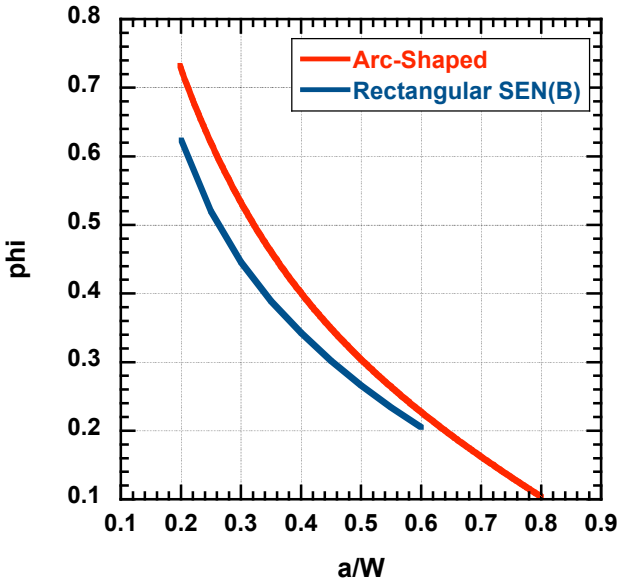


FIGURE 3.11: Comparison of ϕ values of arc-shaped and rectangular specimens

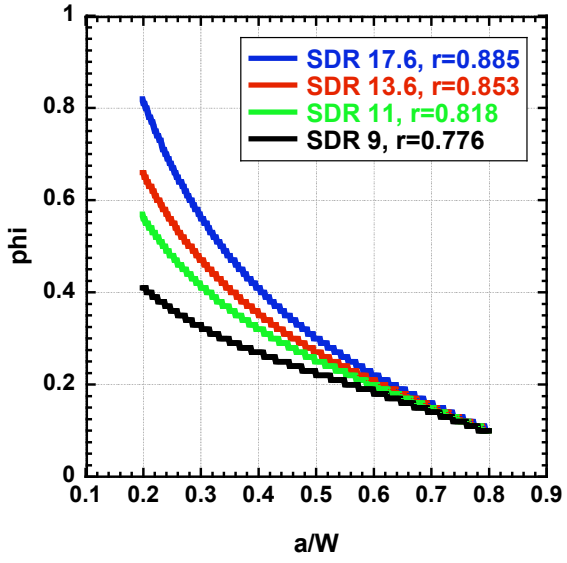
3.1.3.5 Generalizing calculations for other pipe geometries

Calculations are generalized for other standard pipe sizes; SDR 17.6, SDR 13.6 and SDR 9. The study is based on pipes having 110 mm outer diameter, for which the wall thicknesses are given as 6.3, 8.1 and 12.3 mm respectively. Noticing the change of radius ratio, r, for different geometries, FEM analysis were again carried out for each case to obtain the uncracked compliance value, C_0. The sample dimensions were taken based on the ASTM 399-90 standard, where B/W ratio is taken as unity. The results are given in Table 3.2 in the dimensionless form C_0EB.

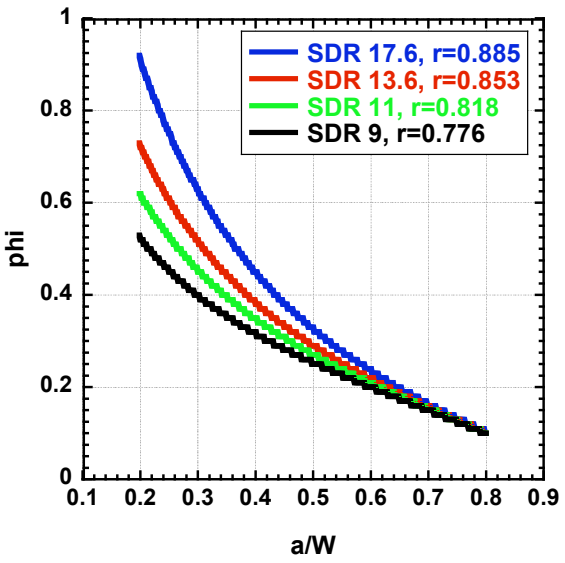
Carrying on the calculations, geometry factor (ϕ) was determined for each pipe for S/W ratios of 3 and 4 and the results were extrapolated to S/W=6 ratio as can be shown in Fig. 3.12.

SDR	S/W=3	S/W=4
9	9.1	18.6
13.6	15.1	26.9
17.6	18.1	35.1

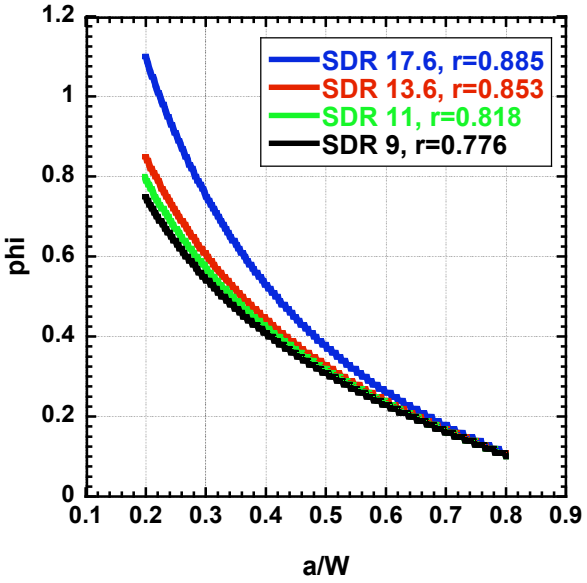
TABLE 3.2: Uncracked compliance of arc-shaped specimens from pipes of various geometries, C_0EB



(a) S/W=3



(b) S/W=4



(c) S/W=6

FIGURE 3.12: Geometry factor (ϕ) values for different pipe geometries

3.2 Elastic Plastic Fracture Mechanics, EPFM

The LEFM approach fails to provide valid fracture toughness values for ductile polymers because of the large plastic zone created at the crack tip. Except for cases where fracture occurs at very low stress levels, the fracture process results in non-linear plastic deformation. This problem led to improvements in non-linear fracture mechanics test and analysis methods.

3.2.1 Essential Work of Fracture (EWF) Method

The EWF method was developed by Cotterel and Reddel [51] following the idea of Broberg who proposed that, in ductile materials (which fracture under elasto-plastic conditions), the crack tip region can be divided in two parts: an inner fracture zone and an outer fracture zone. The applicability of the EWF method relies on the following assumptions,

- The ligament should completely yield prior to fracture initiation
- The essential fracture work W_e inside the inner fracture process zone is proportional to the ligament length, l
- The plastic work W_{pl} in the outer process zone should be proportional to the square of the ligament length, l^2

The total work of fracture (W_f) can be written as,

$$W_f = W_e + W_{pl} \tag{3.34}$$

where W_e is the essential work of fracture and W_{pl} is the non-essential, plastic work. W_f can be given by the related specific work terms by,

$$W_f = w_e lt + \beta w_{pl} l^2 t \tag{3.35}$$

$$w_f = \frac{W_f}{lt} = w_e + \beta w_{pl} l \tag{3.36}$$

where t is the thickness, w_e and w_{pl} are the specific essential work of fracture and specific plastic work respectively and β is the plastic zone shape factor. Since both w_e and w_{pl} are material constants, and are independent of l under plane stress conditions, w_f will vary in a linear manner with l. By extrapolating the curve of w_f-l to zero ligament length, w_e can be obtained [52].

To improve the accuracy of fracture parameters obtained from EWF method, a large number of measurements is required covering the greatest possible range of ligament size [53].

The EWF method for the determining w_e of ductile polymers in plane stress is now well accepted by many researchers. Since the introduction of extended EWF methodology to impact testing of ductile polymer blends by Mai *et al.* [54] there has been considerable interest in the application of the methodology [52, 53, 55-60].

In this study, we will be referring to the EWF approach in the Reversed Charpy analysis for measuring plane stress fracture resistance (w_{pl}) as will explained later in Chapter 5.

3.3 Conclusions

The primary aim of this chapter is to give a brief background on the fracture mechanics concepts. Using basic concepts, geometry factors for arc-shaped specimens have been calculated in order to determine correct impact fracture resistance values for the designated specimens and to fill a gap in this area of research.

In the following chapters, fracture resistance determination methods will be introduced with detailed results analysis sections where the concepts of this chapter will be referred to.

Chapter 4

Rapid Crack Propagation Tests on Pipe

Rapid Crack Propagation (RCP) was identified as a potentially catastrophic failure mode in high pressure steel pipes about 35 years ago [61]. It has been identified as one of the most dangerous failure modes of a PE pipeline and is characterised by high crack speeds of order 100m s^{-1} and above, a glassy fracture surface with little or no evidence of plastic deformation, a sinusoidal crack path, and a sharply defined critical pressure (P_c) at which crack length jumps from arrest to indefinite propagation for a small change in pipe pressure.

The aim of this chapter is to investigate the RCP behavior of polyethylene pipes using experimental techniques and to review the effect of structural and processing conditions on the resulting pipe performance. Before the experimental sections, a brief review is given on pipe fracture and on test methods in order to build a background for understanding and interpreting the experimental results.

4.1 RCP Phenomena and Test Methods

An RCP event is composed of two main processes, namely *crack initiation* and *propagation*. The initiation can be caused by third party damage, growth of a slow

crack or fatigue crack to a critical length, or from defects in fusion joints [9, 62]. Once the failure is initiated, it can either settle to a steady state and the crack will propagate indefinitely in the axial direction at speeds of 100m s^{-1} or more, or arrest. If the pipe pressure is high enough to overcome arrest in the initiation stage, steady state RCP may proceed until a discontinuity in the pipe is reached, and this is defined as *propagation* [62]. In the occurrence of RCP, the nature of the impact that initiates RCP, the pressure, the temperature, the geometry of the pipe, the pipe material and the contained fluid play an important role.

Although RCP failures in plastic gas pipelines have not been common, it has been universally accepted by gas and water utility companies that an RCP failure must never occur in service due to the heavy risks involved. In order to prevent possible failures, it is necessary to design against RCP. The maximum operating pressure of the pipeline in service is the key parameter since a gas pressurised pipeline can be thought as a thin shell wrapped around an enormous quantity of stored energy. However, Irwin and Corten [63] showed that the energy in the pipe wall itself is enough to sustain crack propagation at reasonable pressures.

In order to understand and simulate the RCP behaviour, Full Scale and Small Scale Steady State (S4) tests have been developed.

4.1.1 Full Scale Test

In order to minimize the risk of RCP failures, serious research activities started in early 1970s. The full scale method was developed by BG Technology to define the initiation of RCP and the pressure above which it propagates. As defined in ISO 13478 [64], this method simulates the actual conditions for a pipeline in service and hence is still used as the reference RCP test.

A 25 m long pipe specimen, of up to 500 mm in diameter is buried in gravel, of size 20-40 mm, to at least 100 mm above the upper surface to simulate real service conditions. The pipe is placed in a through with cooling water circulating around it to maintain a consistent test temperature.

The specimen is extended by a steel pipe of at least twice its length to simulate an infinitely long pipe, and is pressurised with nitrogen gas. A crack is initiated by a 400 mm long steel blade, driven to the pipe wall close to one end, where it has been cooled to approximately -60°C. If the crack extends more than 90% of the specimen length, then it is considered to be propagated, and if not it is considered to be arrested.

Since one test takes about 2-3 days including the laying of the pipe and data collection, and you need to have done at least six tests to have precise results, getting a result for a pipe can take around three working weeks. Following this, the time and financial cost of each test led to the search for more efficient methods.

4.1.2 Small Scale Steady State (S4) Test

In 1987, Yayla and Leevers [65] developed a laboratory test to study rapid crack propagation in tube specimens of plastics. Overcoming the cost disadvantage of the full-scale test method, this method then became a simulation of the full scale test at a small scale and is called the Small-Scale Steady State, S4, test. The success of this test led to it being adopted as an ISO standard method (ISO 13477) for gas pipes and to extensive use in subsequent research on RCP.

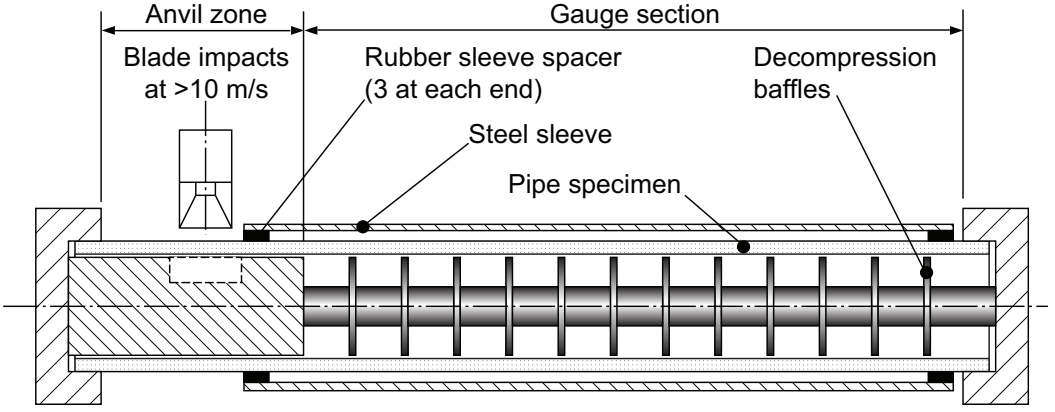


FIGURE 4.1: Schematic representation of an S4 Test [2]

A pipe specimen, 7 diameters in length, is sealed at both ends, pressurised with air and impacted radially near one end by a chisel ended projectile to drive a

fast running crack into the main section of the pipe. To suppress the decompression of the pipe, internal disc baffles are spaced along it and the flaring of the pipe is restricted by a containment cage surrounding the pipe. The containment cage is neither a liner or backfill representor nor a safety precaution. It is used to stabilize crack propagation above critical conditions and helps to define them unambiguously, without *false arrests* [66].

In an S4 test, the crack is said to have propagated if the crack length satisfies the condition of $a > 4.7d$ (d=outside diameter), where a is defined from the crack point. The crack arrests if the crack driving force is too small to overcome the fracture resistance of the material, and the crack propagates if the driving force is sufficiently high. In Fig. 4.2, a PE pipe subjected to the S4 test [2] above its critical pressure can be seen, where propagation is observed (for illustration, the cage has been removed).



FIGURE 4.2: PE pipe subjected to the S4 test [2] above its critical pressure

4.2 Determination of RCP Properties: Critical Pressure and Critical Temperature

Rephrasing previous sections, having been defined for Full Scale test originally, the critical pressure (P_c) is the pressure above which the crack propagates. As the temperature increases, there is a transition from brittle to ductile behaviour and above this transition, RCP can not occur at any attainable pressure. Based on

this, T_{c-S4} is defined as the lowest temperature at which the pipe is tough enough to arrest the crack and no longer shows a propagation.

If a sufficiently high test pressure is chosen and S4 test temperature is varied, T_{c-S4} can be measured. On the other hand, below T_{c-S4}, P_{c-S4} is almost constant while it increases rapidly above T_{c-S4} making RCP impossible (Fig. 4.3). Thus, the ideal pipe material is one that always operates above its T_{c-S4}.

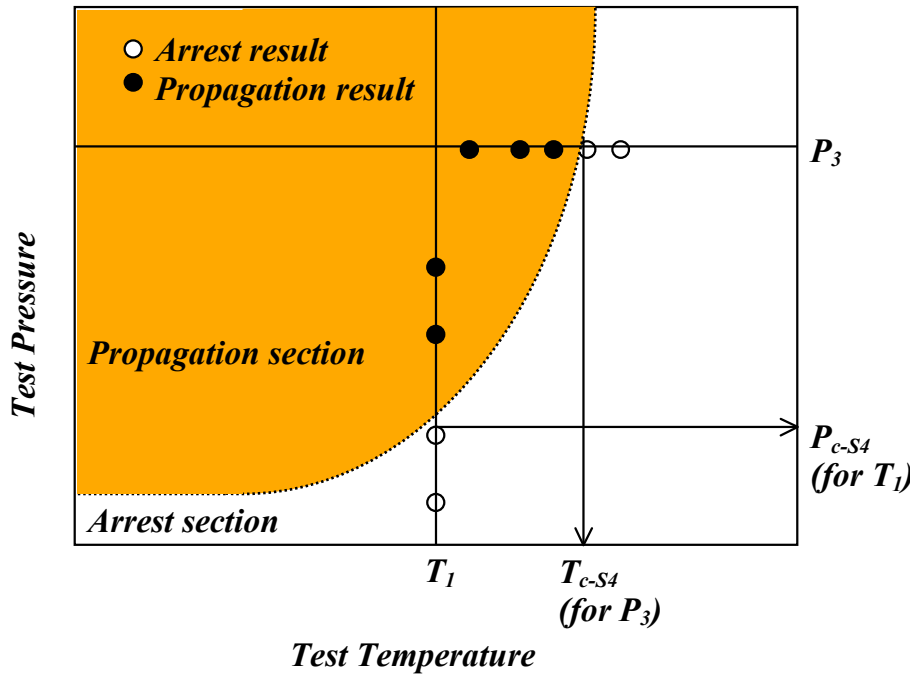


FIGURE 4.3: RCP boundaries determining critical conditions

4.2.1 Definition from Single Test Results

For the determination of critical pressure, pipe samples are tested at various pressures while keeping the temperature constant. The lowest pressure where propagation is observed is taken as the critical pressure, P_{c-S4}. For the determination of critical temperature (T_{c-S4}), the same method is used for each test, but instead of keeping temperature constant and pressure changing, this time pressure is kept constant, and the tests are done at varying temperatures. The application of this is shown in Fig 4.4, where the T_{c-S4} is taken as the first point below the critical

crack length as the temperature is increasing. In order to have a precise value, the interval between test temperatures should be kept as small as possible.

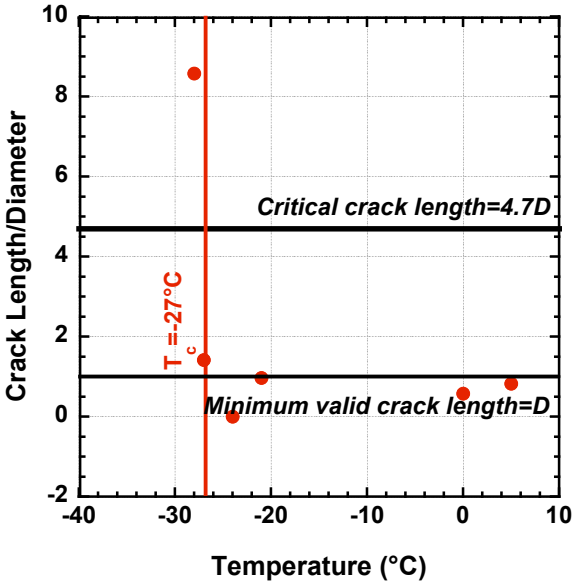


FIGURE 4.4: Determination of Critical Temperature (T_{c-S4}) at test pressure P=5 bar

Critical temperature is found to be thickness and pressure dependent, where critical pressure is found to be dependent on temperature, pipe dimensions, material and the pressurising medium [62].

In an S4 test, RCP is possible at low pressures because the pressurised air is unable to decompress by backflow and outflow through the crack that it creates. In a full scale test, during the propagation of crack, gas escapes and is replaced by the backflow from the uncracked region ahead [66].

The following conversion factor is used to relate the S4 Test results to full scale results, which is determined primarily by differences in gas dynamics and provides a good estimate for the lower bound of full scale critical pressure data so far available [67].

$$P_{c-FS} = 3.6 \times P_{c-S4} + 2.6(\text{bar}) \tag{4.1}$$

4.2.2 Explaining P_c in terms of material properties

As mentioned before in Section 3.1.1, the work that must be supplied to a fast-running crack front to separate unit area of material during axial propagation is defined as the dynamic fracture resistance, G_D. This is a material property and a function of crack speed, and as mentioned before, it can be determined from high speed double torsion test (HSDT) [40] or by hydrostatic S4 [9, 41] tests using a small-diameter pipe pressurised filled with water. The critical pressure found from hydrostatic S4 tests is related to minimum G_D by the Irwin-Corten relation [63] as,

$$P_c = \frac{1}{\mathrm{SDR}}\sqrt{\frac{8EG_D}{\pi D}} \tag{4.2}$$

where SDR is the standard dimension ratio, E is the tensile modulus of material, and D is the outside diameter. It must be noted that Equation 4.2 is only valid for water-pressurised pipe under special conditions, which can be achieved in the laboratory but not in practice [41]. Via this relationship G_D is equated to the critical pressure and pipe geometry.

For pipe pressurised by a compressible gas, rather than water, the crack driving force G depends on crack speed as well as pressure, which makes the measurement of G_D very difficult. Although water pipelines operate at higher pressures, their energy storing capacity is lower than gas pipelines. The critical pressure is therefore higher and increases even more due to faster decompression taking place in water [66].

4.2.3 Plane stress and plane strain fracture in pipes

In order to understand the RCP behavior in detail, one must know the primary cause of the propagation. When the specimens are investigated, it was seen that the brittle fracture was dominant but nevertheless there was a thin white zone near the bore representing large strain plastic deformation. Figure 4.5 demonstrates these plane strain and plane stress regions on the pipe surface. Above T_{BT}, shear

lips grow rapidly prior to crack arrest. This is the reason why, in order to overcome the effect of shear lip formation in the RCP, Yayla [65] introduced razor notching technique (Fig. 4.6). An internal notch is applied to the samples to eliminate the effect of the shear lips and to help initiate a crack. It is observed that the crack path follows the notch direction.

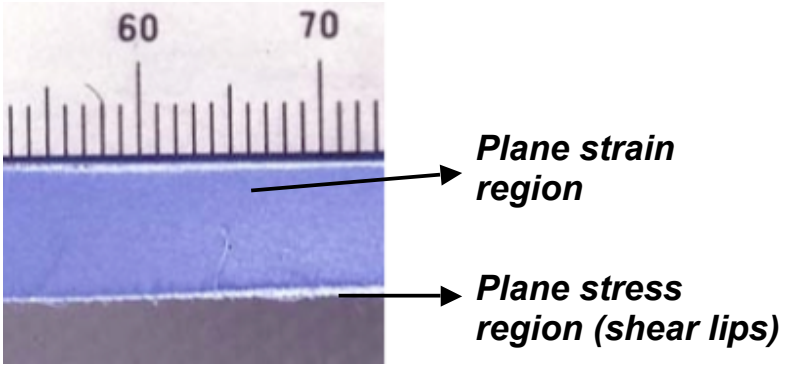


FIGURE 4.5: Plane strain and plane stress regions on an impacted fracture surface of a pipe (units in mm)

The plane stress region absorbs more energy per unit area than the plane strain surface. Plane strain G_{1D} and plane stress G_{2D} components together give the effective G_D, which can be expressed as,

$$G_D B = (B - 2s)G_{1D} + 2sG_{2D} \tag{4.3}$$

where s is the width of the plane stress region at each edge of a crack path of total width B.

For a PE pipe, the critical temperature increases with section thickness and decreasing diameter under other constant conditions [66]. This can be explained by the fact that as the thickness of the wall is decreased, it gets closer to the plane stress condition and the crack is less likely to propagate. Therefore, thinner sections have lower T_c.

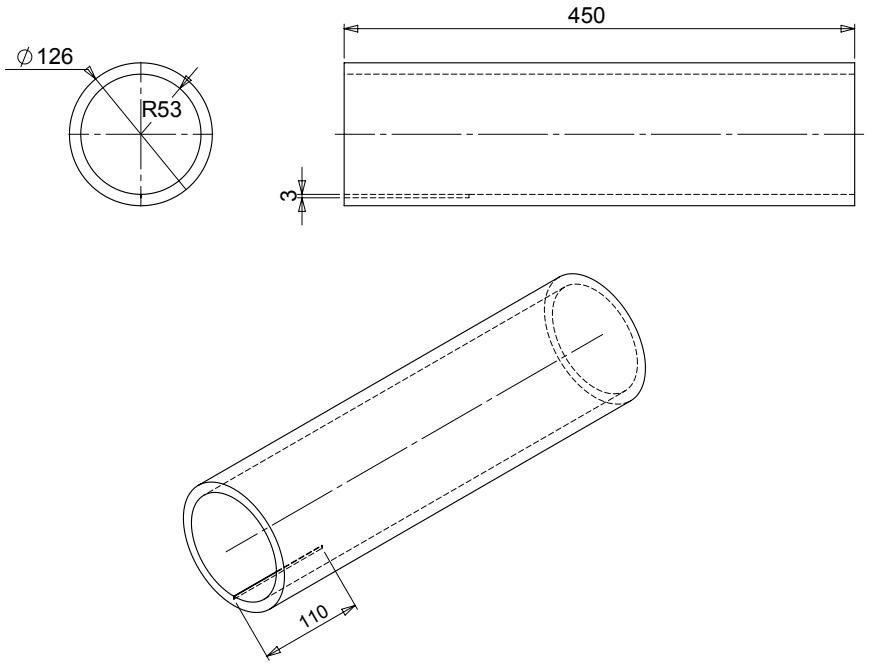


FIGURE 4.6: 110 SDR 11, S4 Test Pipe Specimen

4.3 S4 Test Results

As previous studies have shown, processing conditions have a significant effect on the resulting pipe performances, such as dual cooling increasing the T_{c-S4} compared with the single cooling case [61, 68]. In this study, in order to investigate the effect of processing conditions more in detail, S4 tests have been carried out at 5 bar aiming to see the effect of;

- Carbon black (CB) addition
- Extrusion screw type, and
- Extrusion rate and temperature

on the resulting T_{c-S4} value. These effects were investigated within two series of pipes consisting of 11 and 7 different conditions respectively. All pipes were extruded by Chevron Philips Chemical Company (CPC) having 59 mm OD with an SDR of 11 and their individual properties are given in the following sections.

The tests were carried out at 5 bar aiming to find T_{c-S4} value for each pipe. Although there were not enough test samples for some cases, the aim was to determine T_{c-S4} within an error range of $\pm 2°C$.

Since the final properties of the pipes are heavily influenced by the blending and mixing process that takes place during processing, the extruder screw types may have an important influence on the performance of the pipes. The screw types defined as low, medium and high shear stand for the shear stress (stress state that is parallel to the face of the material) applied to the material during extrusion. The design and geometry of the screws can alternate the mixing, melting and dispersity of the resulting product. Although the exact geometries of screw types studied in this project are confidential, Fig. 4.7 can be referred to give a basic understanding.

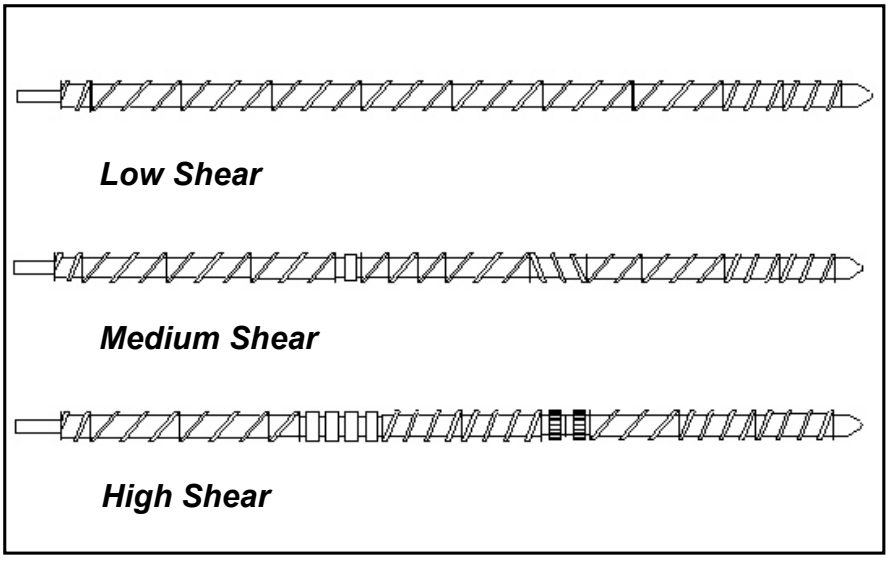


FIGURE 4.7: Extrusion Screw types [4]

4.3.1 Specimen Preparation

Pipe samples are deburred at both ends to make sure that the pipes clamp to the testing rig perfectly. The internal notches are made with care by using a notching bar, which is a metal bar having a razor blade at the tip. The razor blade of the

bar is changed periodically every 3 pipes in order to provide sharp notches. The usual depth of the notch is 2 mm.

The pipes are kept in the freezer at constant temperature that is 2°C lower than the testing temperature for at least 12 hours before testing and are tested within 3-min after being taken out of the freezer.

4.3.2 Experimental Results

4.3.2.1 S4-11: Effect of Carbon Black and Extrusion Screw Type

This pipe set consists of three base polymer materials (materials 1 to 3), which are converted into pipes having different CB amounts and pipes that have been extruded using different screw types enabling us to see the effect of CB and screw type on the resulting T_{c-S4} value. The data of these pipes are given in Fig. 4.8 emphasizing the differences between them.

As briefly mentioned before in Section 2.5, Carbon Black (CB) is usually added to gas pipes to enhance their weatherability and UV stability. In the USA, pipe fabricators physically mix the base PE and a CB masterbatch just prior to the extrusion (single-screw extruders) of the desired pipe. Consequently, the extrusion history (such as as screw type, extrusion rate, and temperature setting) affects the mixing and dispersion of the CB in the ultimate pipe. For the purposes of pipe industry, it is important to study the influence exerted by the quality of CB dispersion on the performance of the ensuing pipes.

To pursue this study, pipes have been extruded by Chevron Phillips Chemical Company and CB was added through a masterbatch that contains about 40 weight percent CB and about 60 weight percent of a medium density PE. This masterbatch is physically mixed with the base PE in a ratio that translates to about 2.5 weight percent CB in the final pipe.

T_{c-S4} values are determined as shown in Figs. 4.9-4.11, where the results are tabulated in Table 4.1. Overall comparison of the results is summarised in Fig.

	No CB	***CB***		
Material-1	**1N**	**3N**	**1B**	**1C**
Material-2	**2N**	**4N**	**2B**	**2C**
Material-3		**5N**	**3B**	**3C**
Carbon Black	0 wt%	2.5 wt%	2.5 wt%	2.5 wt%
Extrusion Screw Type	2-Stage, ***Low-Shear***	2-Stage, ***Low-Shear***	Barrier, ***Medium Shear***	Barrier, ***High-Shear***
Extrusion Rate (kg/hr)	68.2	68.2	68.2	68.2
Specific Rate (kg/hr/rpm)	0.82	0.84	0.78	0.72
Head Pressure (MPa)	7.7	8.7	10.9	11.0
Screw Torque (Amps)	51	51	60	61
Melt Temp. (°C)	234	234	236	236

FIGURE 4.8: Data for the pipe specimens

4.12. For the case of material 3 (including pipes 5N, 3B and 3C), it was not possible to find T_{c-S4} since the current conditioning units are not capable of going below -45°C, at which these pipes still arrest.

Effect of Carbon Black (CB) Addition

The effect of CB addition on the S4 performance can be determined by comparison of the results within the pairs, 1N and 3N, 2N and 4N (which differ in CB content while having the same extrusion conditions). Analysing the results given in Table 4.1, it is seen that for the first case (1N and 3N), T_{c-S4} remains the same, 8°C, where in the second case (2N and 4N), T_{c-S4} is found to decrease slightly (from -36°C to -38°C), resulting in a better performance with CB addition. In either

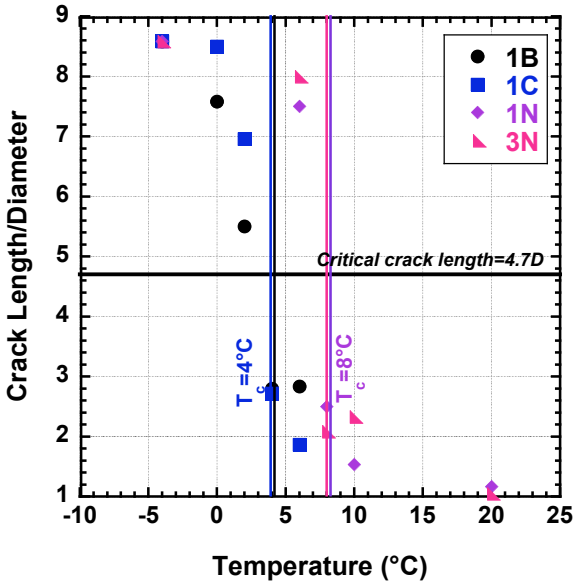


FIGURE 4.9: S4 Test Results for Material 1

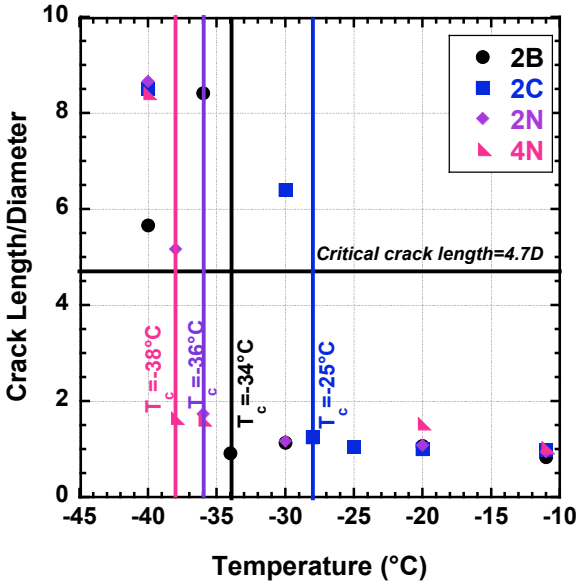


FIGURE 4.10: S4 Test Results for Material 2

case, based on the specimens tested here, it can be concluded that CB addition does not have a major effect on the S4 performance.

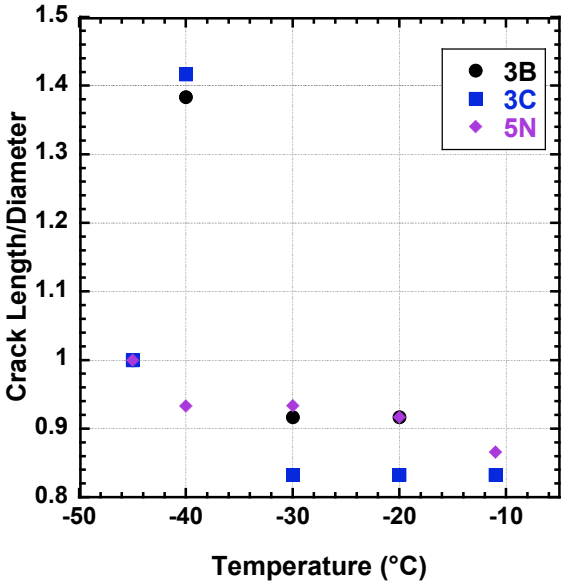


FIGURE 4.11: S4 Test Results for Material 3

Effect of Extrusion Screw Type

The effect of different screw types was investigated within each material group as plotted in Figs. 4.9, 4.10 and 4.11. From the results it is not possible to draw a general conclusion since they show different trends. For Material 1, the lower the shear, the worse the S4 performance (higher the T_{c-S4}), whereas for material 2, the lower the shear, the better the material (lower the T_{c-S4}) and finally for the third material, there is no change observed within the capacity of the current test conditions.

Based on these results, it can be concluded that the effect of extrusion screw type on S4 performance in terms of T_{c-S4} is material dependent according to our current understanding.

4.3.2.2 S4-7: Effect of Extrusion Rate and Extrusion Set Temperature

The mechanical properties of semicrystalline polymer materials are known to be affected by crystallinity which is highly dependent on the cooling rate of the material, as will be discussed more deeply in the later chapters. Extrusion conditions,

ID	B	C	N
1	4	4	8
2	-34	-28	-36
3	-45	-45	8
4	—	—	-38
5	—	—	-45

TABLE 4.1: S4 Critical Temperature Values (°C)

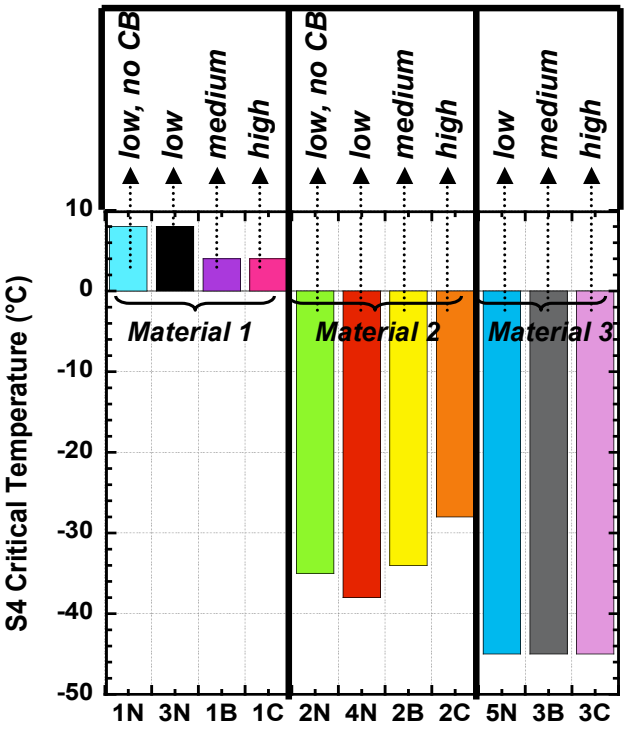


FIGURE 4.12: Comparison of S4 Critical Temperature Values for 3 materials as a function of carbon black content and shear

temperature and rate parameters are therefore considered to play an important role on the RCP performance.

Aiming to investigate this idea further, a single polymer is chosen, TR480X from which 7 different pipes were extruded by CPC under different extrusion conditions. The details of the processing conditions are given in Table 4.2.

Pipe ID	Extrusion Rate (kg/min)	Extrusion Set Temperature (°C)	Screw Torque (amps)	Extrusion Pressure (MPa)	Melt Temperature (°C)
A	0.75	193	59	11.44	205
B	1.13	193	69	14.34	205
C	1.51	193	78	15.50	204
D	0.75	250	54	10.40	261
E	1.13	250	66	12.26	262
F	1.51	250	74	13.71	261
G	1.13	227	70	13.43	240

TABLE 4.2: Extrusion information

Test results are plotted in a comparative manner within each extrusion set temperature in Figs. 4.13-4.14, and 4.15 and resulting T_{c-S4} values are tabulated in Table 4.3. Figure 4.16 summarises all the results from which comparisons can be made clearly.

Effect of Extrusion Rate

The effect of extrusion rate can be investigated within each extrusion set temperature group individually (at 193°C pipes: A, B and C; and at 250°C pipes: D, E and F). As can be seen from the results (Table 4.3), for each temperature, T_{c-S4} decreases with increasing extrusion rate indicating better performance, which was also observed by Davis [61]. This can be explained referring to the effect of the shear forces acting during pipe extrusion. The increased shear results in the molecules aligning in the direction of the extrusion process, which is effectively the direction of the running crack. As a consequence, these molecules oriented parallel to the direction of a running crack would not be capable of stopping the crack. In the case of increased extrusion rates, molecules will have not enough time to align in the direction of extrusion, which is advantageous in terms if increased fracture toughness, while decreasing T_{c-S4}.

Effect of Extrusion Set Temperature

The effect of extrusion set temperature can also be investigated within each extrusion rate group. For 0.75 kg/min, when pipes A and D are compared, it is seen that as the extrusion temperature increases, T_{c-S4} decreases. However for the other rates, 1.13 kg/min and 1.51 kg/min, T_{c-S4} increases with increasing temperature.

As a consequence, it can be concluded that changing extrusion temperature does not have a consistent influence on the S4 performance. At higher extrusion rates, extrusion temperature has a negative effect on the S4 performance while at lower rates it improves S4 performance.

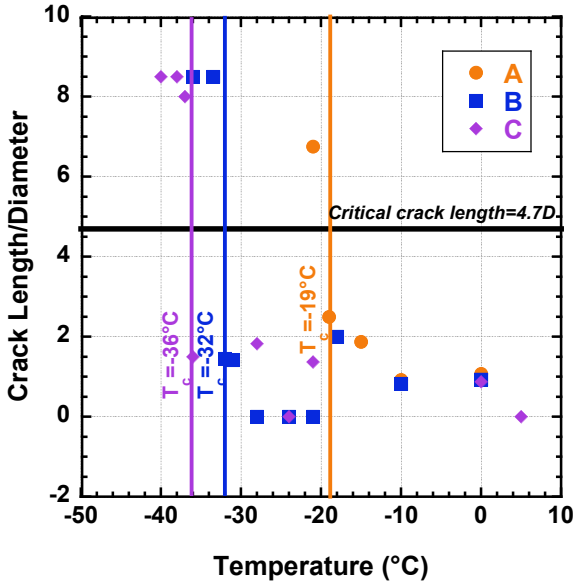


FIGURE 4.13: S4 Critical Temperature Values (°C) for pipes extruded at 193°C at different extrusion rates (see Table 4.2)

4.3.3 Conclusions

In this study, the S4 test results are analysed in a comparative manner without considering any details of the RCP phenomena.

The primary aim of this chapter is to investigate the effect of processing conditions on the pipes' RCP performances based on the S4 test results. The effect of

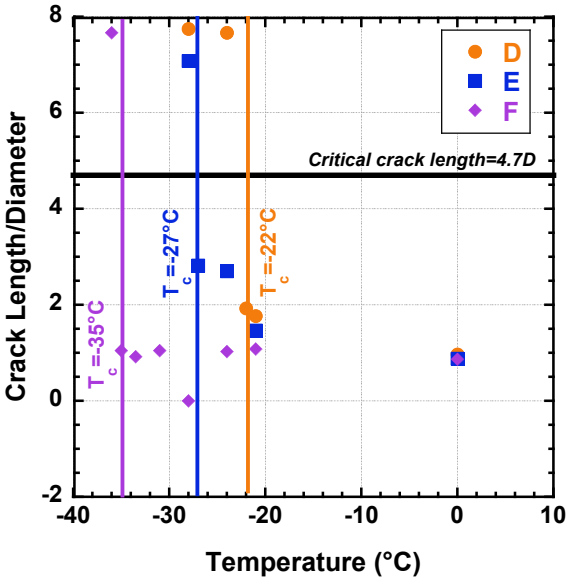


FIGURE 4.14: S4 Critical Temperature Values (°C) for pipes extruded at 250°C at different extrusion rates (see Table 4.2)

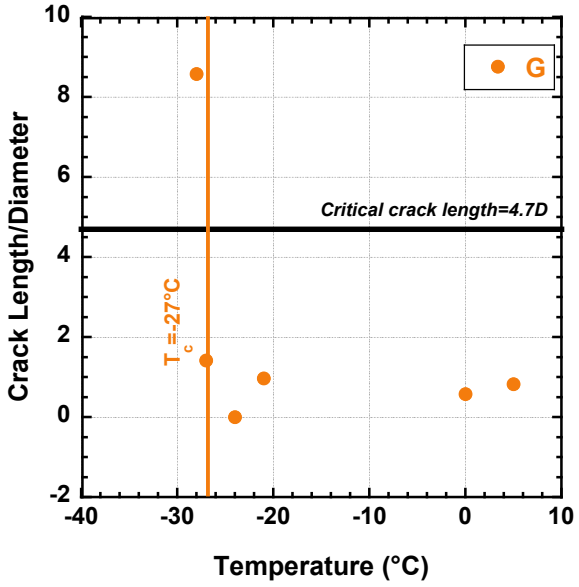


FIGURE 4.15: S4 Critical Temperature Values (°C) for pipe extruded at 227°C, having extrusion rate of 1.13 kg/min

extrusion rate, temperature, screw type and carbon black addition has been analyzed on two different pipe groups extruded by CPC. S4 tests were performed in order to find T_{c-S4}, and the obtained values are used for comparing the materials' performances.

Extrusion Rate (kg/min)	Pipe ID	T=193°C	Pipe ID	T=250°C	Pipe ID	T=227°C
0.75	**A**	-19	**D**	-22		
1.13	**B**	-32	**E**	-27	**G**	-27
1.51	**C**	-36	**F**	-35		

TABLE 4.3: S4 Critical Temperature Values (°C)

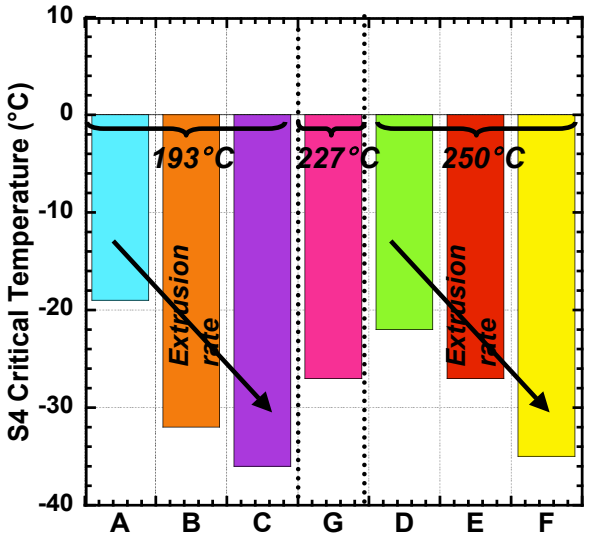


FIGURE 4.16: Comparison of S4 Critical Temperature values for various extrusion temperatures and rates

It can be concluded that CB addition either leads to a better S4 performance in terms of decreasing T_{c-S4} or does not have any effect on pipes' RCP performance.

By the increase in the extrusion rate, the molecules being unable to align in the direction of the extrusion, effectively result in increased fracture resistance and S4 performance of the pipes, which was also observed by previous researches in the area [61].

Comparing the effect of extrusion screw types (low, medium and high shear), it is not possible to draw a precise conclusion based on the materials tested here, since the effect of extrusion screw type varies for each material group.

Similar inconsistency was observed for the effect of extrusion set temperature since at lower rates, extrusion temperature was found to improve the performance while at higher rates, temperature was found to have a negative effect on the performance.

Chapter 5

ISO CD 17281 Impact Bend Test

In order to determine a pipe's performance and operating conditions, S4 tests were performed as described in the previous chapter. Although this test is small in scale compared to the full scale test, the search for an even smaller and more practical test has been continuing. A test method that would provide information on the performance of the polymer prior to extrusion into pipe would be the ideal case. With this idea, Instrumented Charpy tests were performed in this study on various groups of materials to determine the ductile to brittle transition temperature as well as the impact fracture toughness. The effects of thermal history, geometry, density, molecular weight and carbon black on the transition temperature and impact fracture resistance values have been investigated in detail.

The fracture toughness is associated with the energy release rate at crack initiation, whereas the transition behaviour of a material is related to the temperature dependence of the total measured impact energy absorption. The specimen geometry, notch depth and experimental setup have a strong influence on the results. Therefore, understanding the complex relationship between impact resistance, processing and/or molecular parameters requires that careful attention be directed to the impact measurement itself [69]. A comparative study concentrating on the material differences can only be carried out by testing specimens at the same conditions with the same geometry. For this reason, close attention is given to the

comparison of arc-shaped specimens cut from pipe and rectangular specimens cut from plaque.

5.1 Experimental Method and Specimen Preparation

The Charpy test is a three point bend impact test that requires a specimen containing a machined notch in the centre of the face facing away from the impacting device. As a basic idea, it measures the energy needed to fracture the specimen. Using a similar geometry, ISO 17281 [70] measures fracture toughness using an instrumented striker at loading rates up to 1 m/s, and was used for the purposes of this study. As can be seen from the test arrangement, Fig. 5.1, the notched specimen is placed on two supports having a specific span (in this case 60 mm), and impacted with a striker behind the notch with a given speed. The load displacement trace recorded during the test is then used for the analysis which will be discussed in Section 5.2.

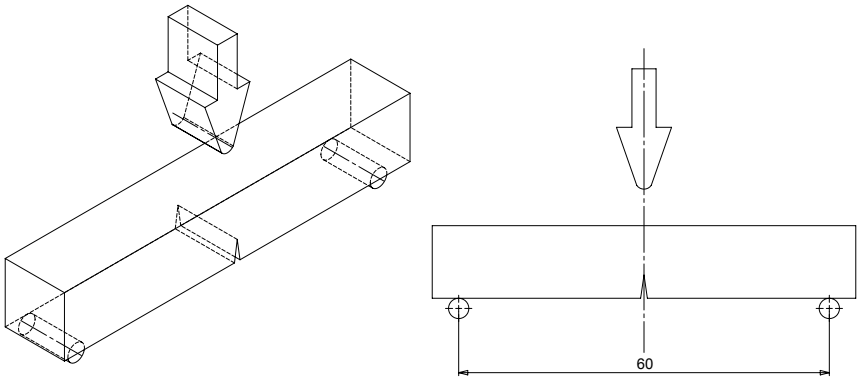


FIGURE 5.1: Three Point Bend Impact Test arrangement

In this project two basic types of specimens were tested: those prepared from moulded plaques (either rectangular or arc-shaped) and those prepared from pipe (arc-shaped).

The idea of testing samples directly from pipes comes from the fact that processing has a significant influence on the final performance of polymers, and material testing should be done on samples having the same processing history. Comparison of pipe test results with the moulded arc-shaped specimens reveals the effect of processing conditions without the risk of geometry effects. On the other hand, the comparison of the results between specimens of different geometries cut from the moulded plaques enables us to detect any effect of geometry on the results and to verify the geometry factor for precise calculations without the risk of a process history effect. An additional process history study is pursued by comparing the results from plaques that have been prepared by different cooling rates.

5.1.1 Preparation of the moulded plaque specimens

PE 100 materials which were received in granular form were compression moulded using a hydraulically driven hot press. The platens of the press were electrically heated but the mould was left to cool slowly by a natural cooling process so that crystallisation could approach the maximum possible.

The granules were left to melt at 160°C for 25 min with a low pressure, and then a force of 10 tonne was applied for 5 minutes in order to release trapped air and excess material. The excess material is squeezed out and the moulding pressure during cooling is only exerted on the frame, not on the material. The mould was then left to be cooled in the machine under 79 MPa pressure until the temperature reached 60°C. In order to see the effect of crystallinity on the resulting material properties, these plaques were further processed using a thermal conditioning press as will be explained in Section 5.1.3.

5.1.1.1 Moulding rectangular specimens

ASTM standard D-1928-96 was followed by using a picture frame type (length = 200mm, width = 200mm, thickness = 12mm) mould (flash type) with high thickness walls in order to minimise heat losses during cooling. The impact bend

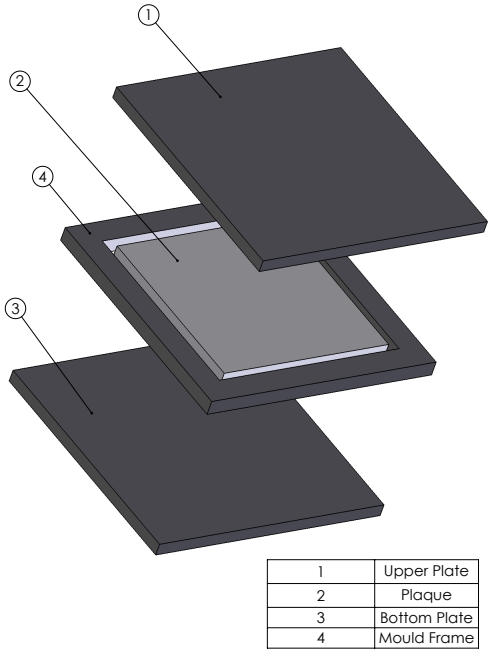


FIGURE 5.2: Compression Moulding Plaques

test specimens were prepared from these plaques with the dimensions of $12(B) \times 12(W) \times 70(l)$ mm as given in Fig. 5.4.

5.1.1.2 Moulding arc-shaped specimens

A new mould was designed (Fig. 5.3) forming segment shaped plaque samples, from which the specimens were machined to achieve an arc-shaped geometry (Fig. 5.5) matching the nominal dimensions of the pipe specimens ($10(B) \times 10(W) \times 70(l)$ mm).

5.1.2 Preparation of the pipe specimens

For the pipe specimens, samples were directly cut from the cross section of pipes resulting in an arc-shaped geometry with the dimensions of $10(B)$ x $10(W)$ x $70(l)$ mm, with the initial notch extending radially from the inside surface (Fig. 5.5).

All specimens were notched to 25% of their thickness with a razor blade following the standards, paying attention to avoid plasticity effects. To eliminate the effect

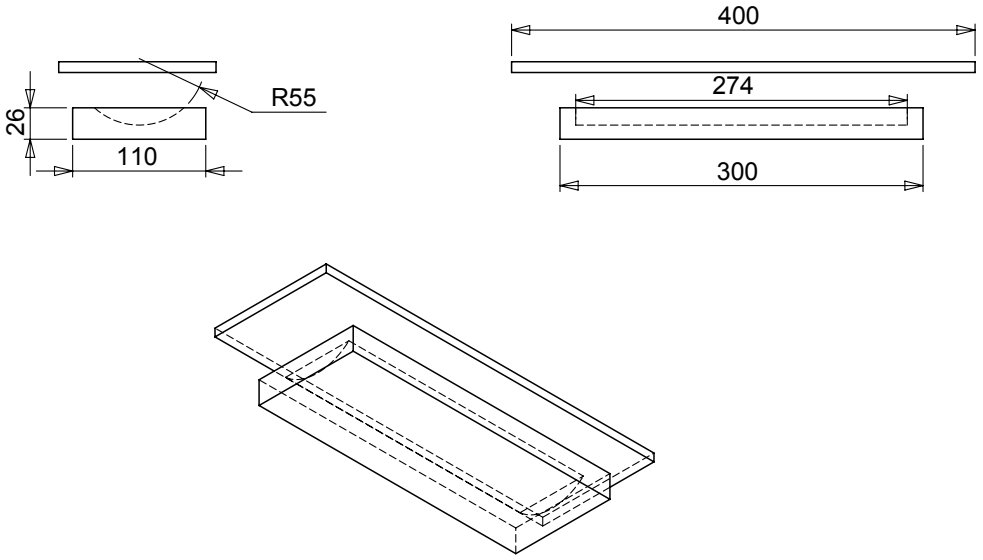


FIGURE 5.3: Arc-shaped Moulding Plaque

of shear lips side-grooving was applied to one set of plaque specimens (Fig. 5.6) and the results were compared.

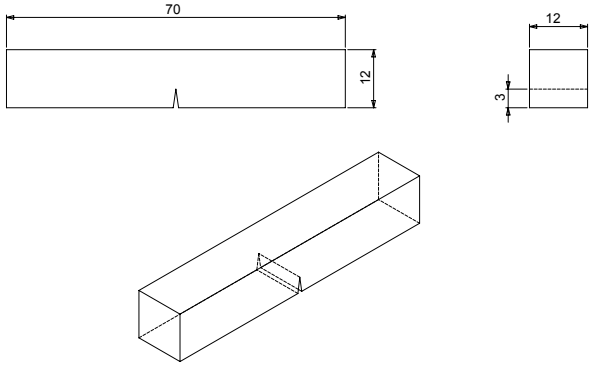


FIGURE 5.4: Rectangular Plaque Specimen

5.1.3 Thermal Conditioning Press

As mentioned before, one of the main parameters influencing polymer performance is crystallinity which can be altered by processing conditions, *ie.* cooling rate. For the purposes of this project, a thermal conditioning press (Fig. 5.7) designed and built by undergraduate students was used [5]. After each plaque had been moulded

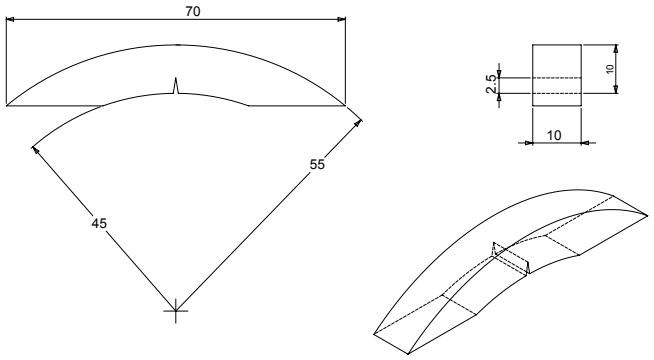


FIGURE 5.5: Arc-Shaped Specimen

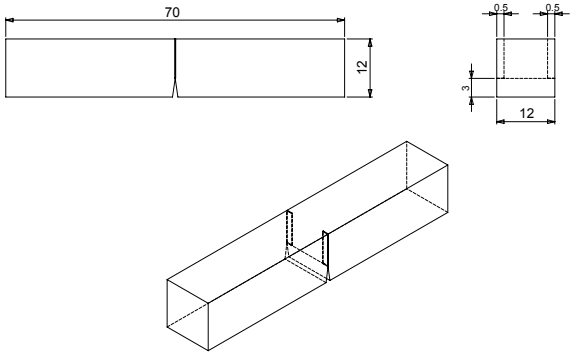


FIGURE 5.6: Side-grooved Plaque Specimen

from granulate, it was remelted using this apparatus and cooled at constant and controlled rate using a pulsed heater and water cooling system. Here it is important to control the cooling rate down to about 80°C, which is the temperature at which PE crystallisation is completed.

The apparatus consists of the press itself, a data acquisition unit (DAQ) and a controlling computer. The data acquisition unit houses the thermocouple amplifier circuits, used to amplify the voltage signals before being sent to the data acquisition hardware installed in the computer, and the solid state relays that are used to switch the heaters and cooling water valves [71]. The test consists of commanding a constant temperature, and measuring the maximum rate at which the surface temperature could be increased or decreased. The output of the system is demonstrated in Fig. 5.8, where the graph indicates that the heating rate is fairly linear up to the soak temperature whereas the cooling rate is linear down to

about 45°C. A wider linear range can be achieved by lowering the cooling water temperature.

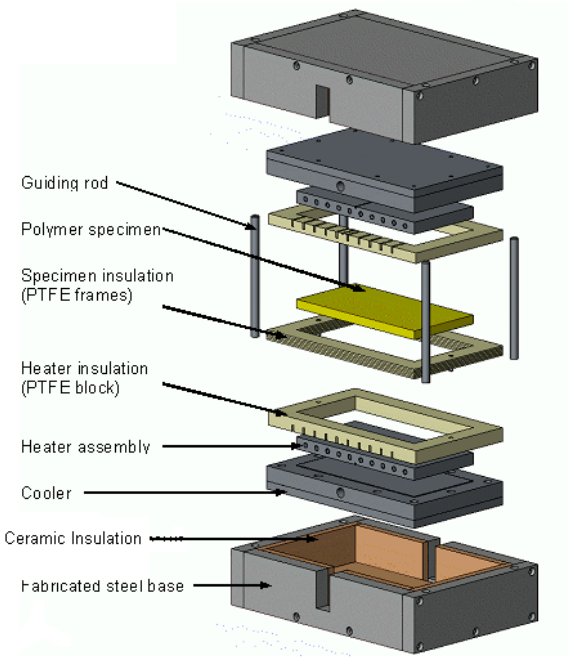


FIGURE 5.7: Thermal History Rig [5]

Further developments/modifications made on the rig by Pearson [71], as a part of a separate project, enabled the usage of the rig confidently with cooling rates of -0.5°C/min (*will be referred to as* CR 0.5) and -10°C/min (*will be referred to as* CR 10) complementing the cooling rate -1.5°C/min (*will be referred to as* CR 1.5-standard plaque) achieved by the hot press after moulding.

[Unless stated otherwise, all the results presented in this project are based on hot-press cooling rate, CR 1.5.]

5.2 Analysis of the Instrumented Charpy Impact Test

During the experiment, load *vs.* time data are recorded and later converted to load *vs.* displacement data by relating to the known impact speed. From this load

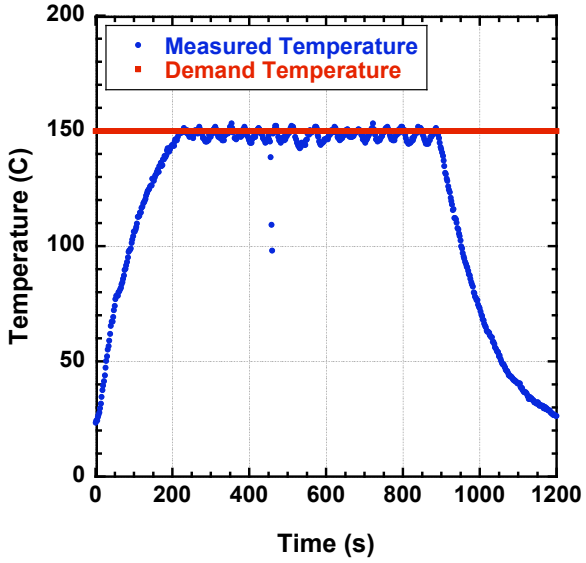
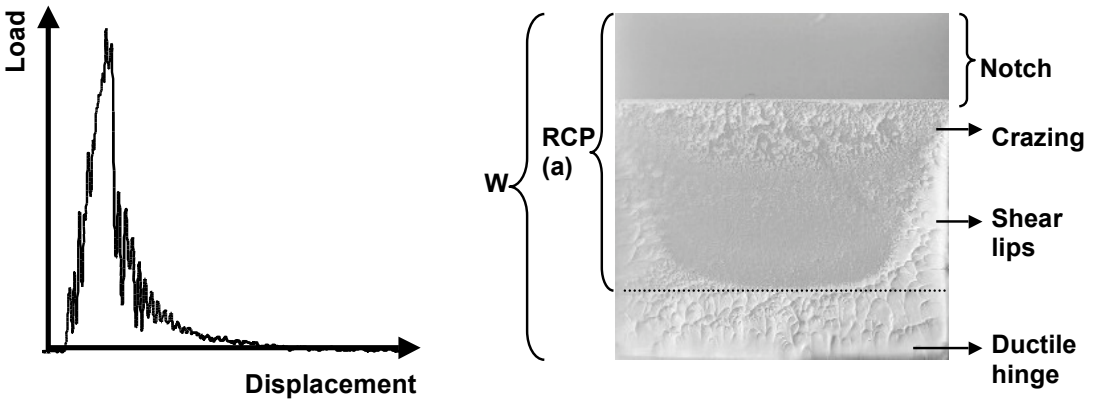


FIGURE 5.8: Heating and cooling rate for top half [5]

displacement curve (Fig. 5.9(a)) the energy absorbed during the fracture of the material is obtained by integrating the area under the curve. The data processing and integration is done using a Matlab program written for this purpose following the criteria in ISO CD 17281 for load oscillations.



(a) A typical Load-Displacement Curve of PE

(b) Fracture Surface of an impacted sample

FIGURE 5.9: Interpreting Load-Displacement traces on a specimen surface having dimensions of 12×12mm, with a notch of 3mm

After impact, the load increases at a rate corresponding to the notched compliance of the specimen. The first region of the plot up to the peak load represents the loading up to the fracture point, and may include the formation of a craze zone at the notch tip which is later seen on the fracture surface of the material

(Fig. 5.9(b)). After this initial loading, there is a rapid drop in the load, which corresponds to the development of a smooth zone in the center of the specimen, referred to as the brittle fracture or RCP region. Any further work done on the specimen is related to the extension of the shear lips and the rotation of a ductile hinge on the fracture surface of the material. Shear lips provide an effective mechanism of crack-arrest. As the temperature is decreased, the load-displacement records change and the marks on the fracture surface become less visible. The signs of ductility: the initial craze zones, the ductile hinge zones and shear lips eventually disappear, letting the fast crack run all the way through the specimen without arresting.

5.2.1 Brittle-Tough Transition Temperature Determination Methods

The transition temperature is related to the mechanism of energy absorption during fracture. In this study, different approaches, which are all based on the same idea, are used to determine the ductile-brittle transition temperature to confirm the validity of the results.

5.2.1.1 Observation of the Fracture Surface

After the tests, the rapid crack propagation zone is clearly visible (as seen in Fig. 5.9(b)) on the fracture surface as a much smoother area between initial craze extension and final crack arrest. The ratio of the length, a, of this RCP zone to the total length available, W, is plotted against temperature for each material. By definition, the crack is observed to propagate until complete failure if the test temperature is below T_{BT} and to arrest if the temperature is above T_{BT}. The transition temperature can be determined from the curve where it starts decreasing, representing the fact that RCP gains almost the whole surface and the crack arrest mark has vanished.

5.2.1.2 Observation of Load Displacement Traces, U^* Method

Observing the presence or absence of post-peak load indicates whether the test was above or below the transition temperature. For example, by analyzing Fig. 5.10, one can conclude that the transition occurs between -34°C and -36°C.

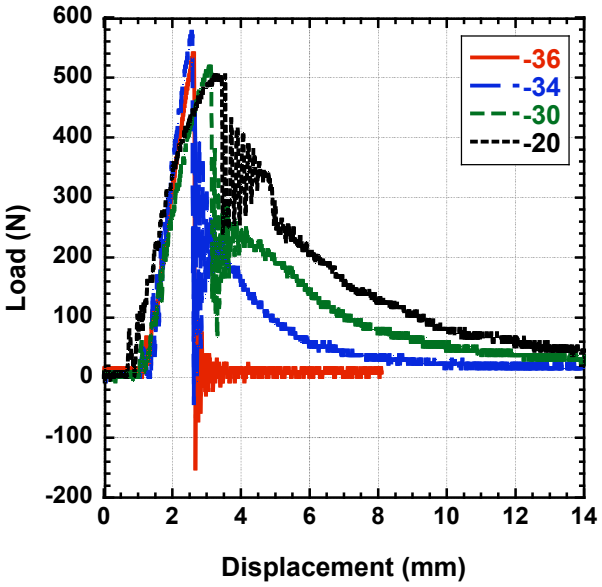


FIGURE 5.10: Observation of transition in the load displacement curve

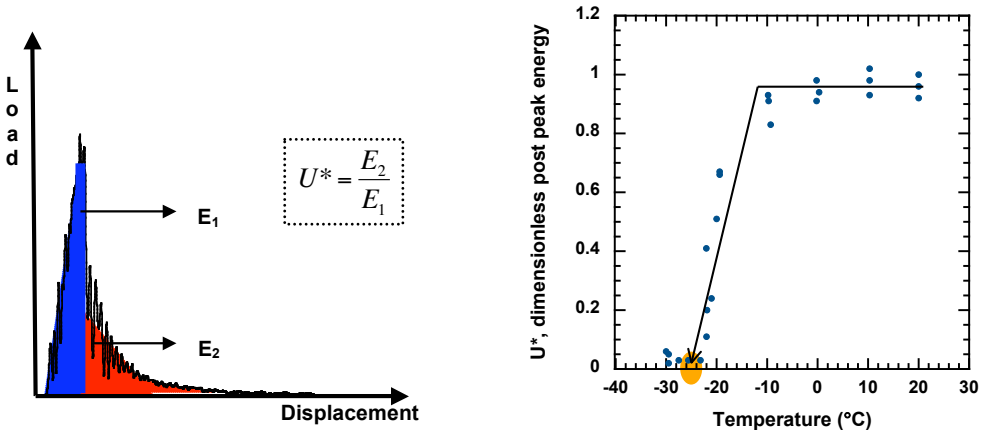
The U^* parameter suggested by Leevers [72] expresses the ratio of the energy values before and after the peak point of a load-displacement figure.

$$U^* = \frac{U_{tot} - U_{peak}}{U_{peak}} \tag{5.1}$$

As seen in Fig. 5.11(b), by drawing a trend-line between consecutive points that have the largest difference in U^* values in a U^* *vs.* temperature plot, transition temperature value can be determined for each material. This 'U^*' parameter indexes the effect of the ductile hinge on a load-displacement plot and uses this observable fact to determine the transition temperature value, below which the ductile hinge vanishes.

For the results of this method to be reliable, tests should be repeated in the range where the ductile hinge is observed to disappear. A large testing temperature

interval within the transition region can lead to very inaccurate results as can be seen in Fig. 5.12. With the additional tests done in between -20°C and -30°C, a more exact transition temperature can be determined (-25°C rather than -30°C).



(a) Energy Integration

(b) U* Method Application

FIGURE 5.11: U* Method

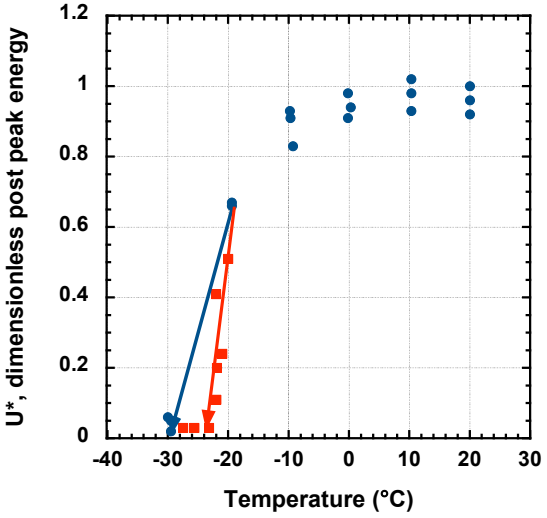
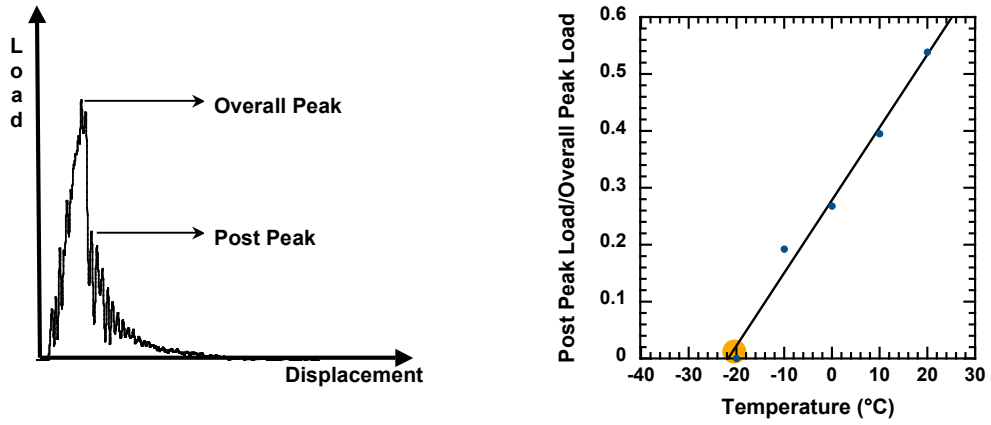


FIGURE 5.12: Misleading results can be obtained if the U* method is not applied correctly

5.2.1.3 Load Ratio Method

Load-displacement traces above the transition temperature often show a load plateau following the sudden drop at fracture initiation. This represents fracture arrest. An alternative method of determining T_{BT} is therefore to plot the ratio

of this post peak load to the overall peak load with respect to the temperature, extrapolating to the point at which arrest just begins to appear (as seen in Fig. 5.13). The overall peak load can be determined easily from the graphs, while the post-peak load is difficult to establish without smoothing the curves. This point is taken to be the point where the curve starts to form a tail representing the ductile behaviour of the material.



(a) Load Points

(b) Load Ratio Method Application

FIGURE 5.13: Load Ratio Method

5.3 Experimental Results

Four material sets (C-Series PE Resins, D Series PE Resins, MW series, CB series) consisting of 7, 4, 3 and 4 different polymer resins respectively were tested, and the results were investigated separately within each group. All the experiments were performed at a uniform speed of 1 m/s and using a span of 60 mm.

5.3.1 C-Series PE Resins

The relationship between molecular structure and ductile to brittle transition temperature was analysed using seven different kinds of polyethylene, PE-2 to PE-8 inclusive (Table 5.1), which were supplied both as granulate and in pipe form by Chevron Phillips Chemical Company [73] (The density values given in Table 5.1

refer to the density of the granules, not to the density of the processed plaques). A comparative analysis was carried out to investigate:

- The effect of processing conditions by comparing arc-shaped specimens cut from pipe and from a moulded disc sector (Fig. 5.17(a))
- The effect of geometry via comparing an arc-shaped moulded specimen and a rectangular plaque specimen (Fig. 5.17(c))
- The effect of processing conditions via comparing the plaque specimens processed at different cooling rates (CR 0.5, CR 1.5, CR 10) (Fig. 5.17(b))
- The effect of plane stress via comparing the impact fracture toughness of a standard notched rectangular plaque specimen and a side grooved rectangular plaque specimen (Fig. 5.17(d))

ID	**Density** (g/cm^3)	M_w **(kg/mol)**	M_w/M_n	M_z **(kg/mol)**
PE-2	0.946	349	31.9	3876
PE-3	0.950	263	19.1	1531
PE-4	0.949	257	18.4	1296
PE-5	0.954	341	21.2	3166
PE-6	0.950	188	6.3	1202
PE-7	0.964	135	5.7	1046
PE-8	0.951	440	50.8	3803

TABLE 5.1: Molecular Characteristics of C-Series PE Resins

5.3.1.1 Determination of Crystallinity: Differential Scanning Calorimetry (DSC)

The crystallinity of each plaque was measured by Chevron Philips Chemicals Company using the differential scanning calorimetry (DSC) technique. Three samples

were tested at each cooling condition and the obtained results are shown in Fig. 5.14.

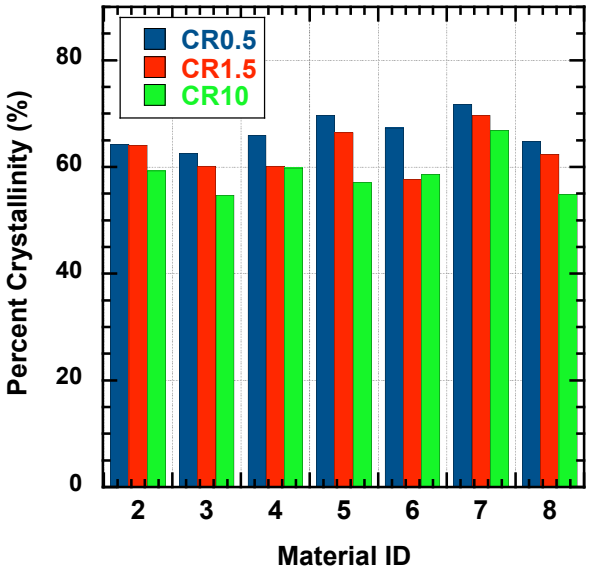


FIGURE 5.14: Percentage Crystallinity Results for C-Series PE Resins for varying cooling rate conditions

The results confirm the expectation that as the cooling rate decreases, the crystallinity of the sample increases.

5.3.1.2 Determination of Tensile Modulus: Dynamical Mechanical Thermal Analysis (DMTA)

For the purposes of this project, DMTA analysis was used to compare the tensile modulus values of different materials in a certain temperature range and to use this information for further interpretation of the G_c values obtained. Only the CR1.5 samples were tested at frequencies of 1 and 10 Hz in the temperature range of -60°C to 60°C.

Based on the modulus values at 0°C, the samples are ranked as,

$$\mathrm{PE}-2 < \mathrm{PE}-8 < \mathrm{PE}-3 \sim \mathrm{PE}-6 \sim \mathrm{PE}-4 < \mathrm{PE}-5 < \mathrm{PE}-7 \qquad (5.2)$$

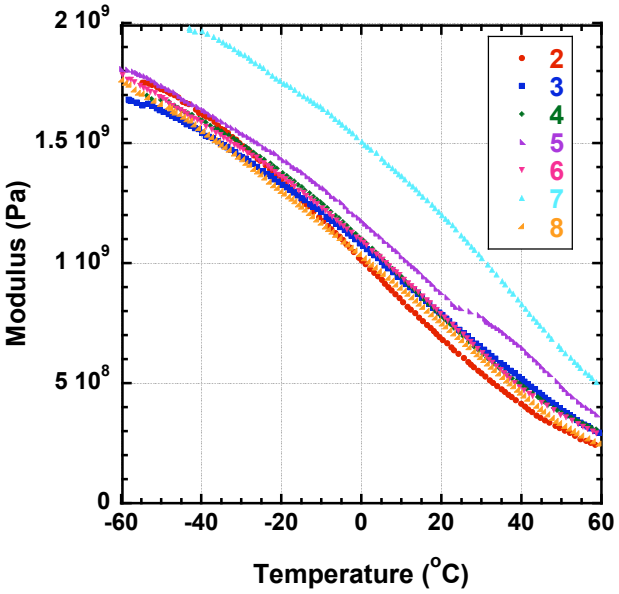


FIGURE 5.15: Modulus (E') versus Temperature for C-Series PE Resins, 10Hz

The relationship between the 0°C modulus values and the density is given in Fig. 5.16, where a kind of linearity is observed.

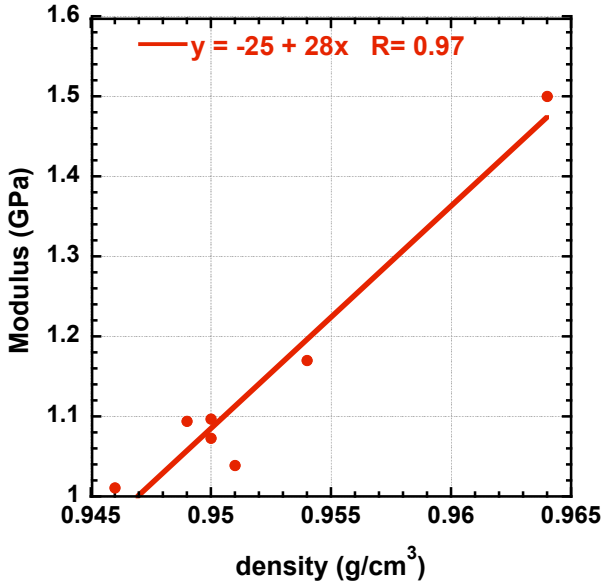


FIGURE 5.16: Modulus (E') (0°C, 10Hz) versus Density for C-Series PE Resins

5.3.1.3 Load-Displacement Plots

Load-displacement traces recorded at 0°C are compared in Fig. 5.17. Both Figs. 5.17(a) & 5.17(b) show that the ductile hinge is larger in the case of a slow cooled specimen. The area under the curve up to the peak point is somewhat similar not showing any significant differences.

Arc-shaped specimens, having a smaller average depth, have a larger compliance (as previously obtained in Chapter 3), which causes them to be loaded more slowly than the plaque specimen as can also be seen from the initial slope of the curve (Fig. 5.17(c)). This is why the geometry factor ϕ should be determined correctly to obtain the correct G_c values.

In order to eliminate the plane stress effect, 0.5 mm side-grooved specimens were tested, which were previously defined in Section 3.1.2.2. As seen in Fig. 5.17(d), the ductile part of the curve disappeared completely confirming that side-grooving eliminates the ductility caused by shear lips. The peak energy, which is observed to be the same in both conditions, is expected to give the same G_c value for both cases.

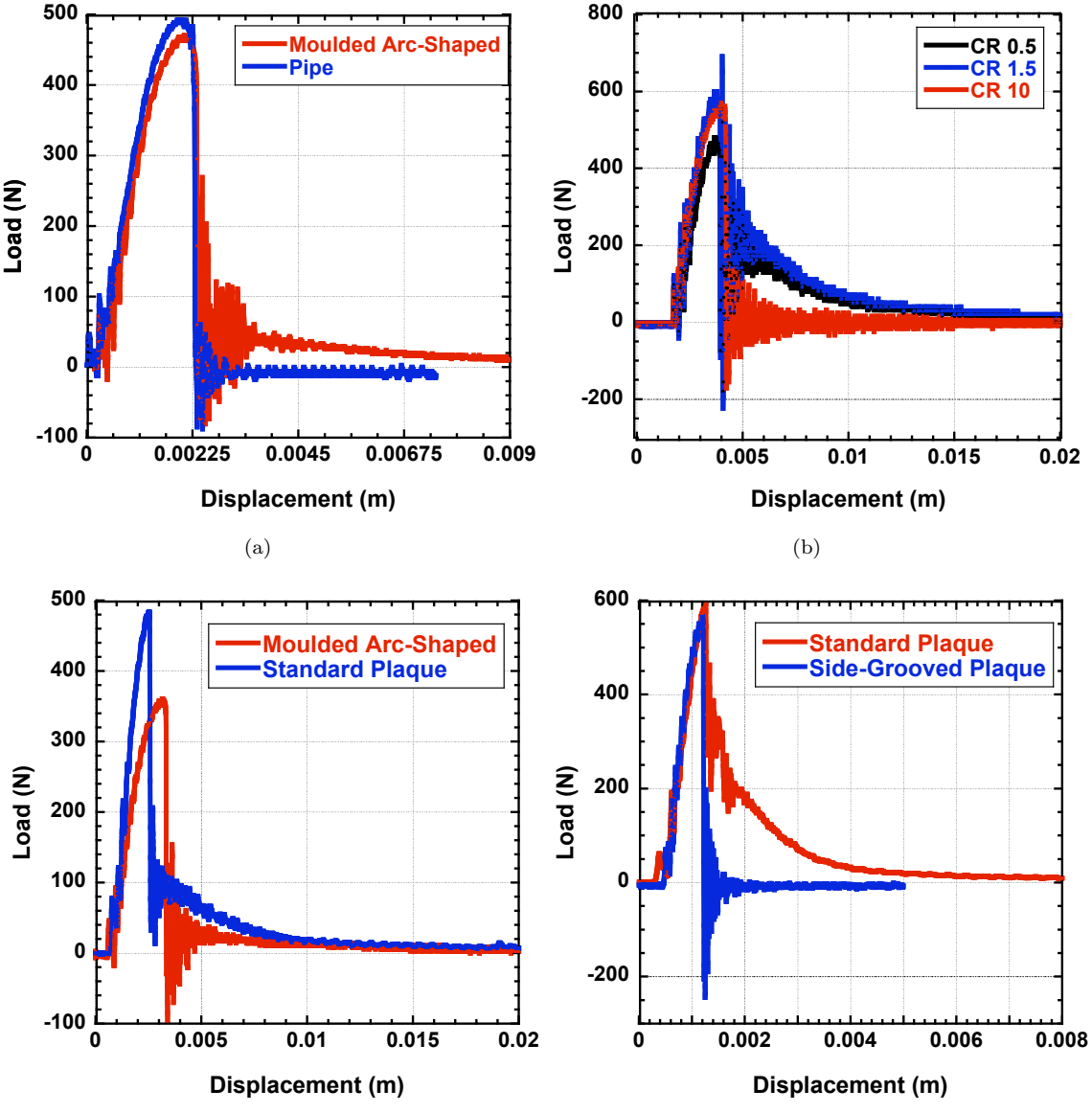
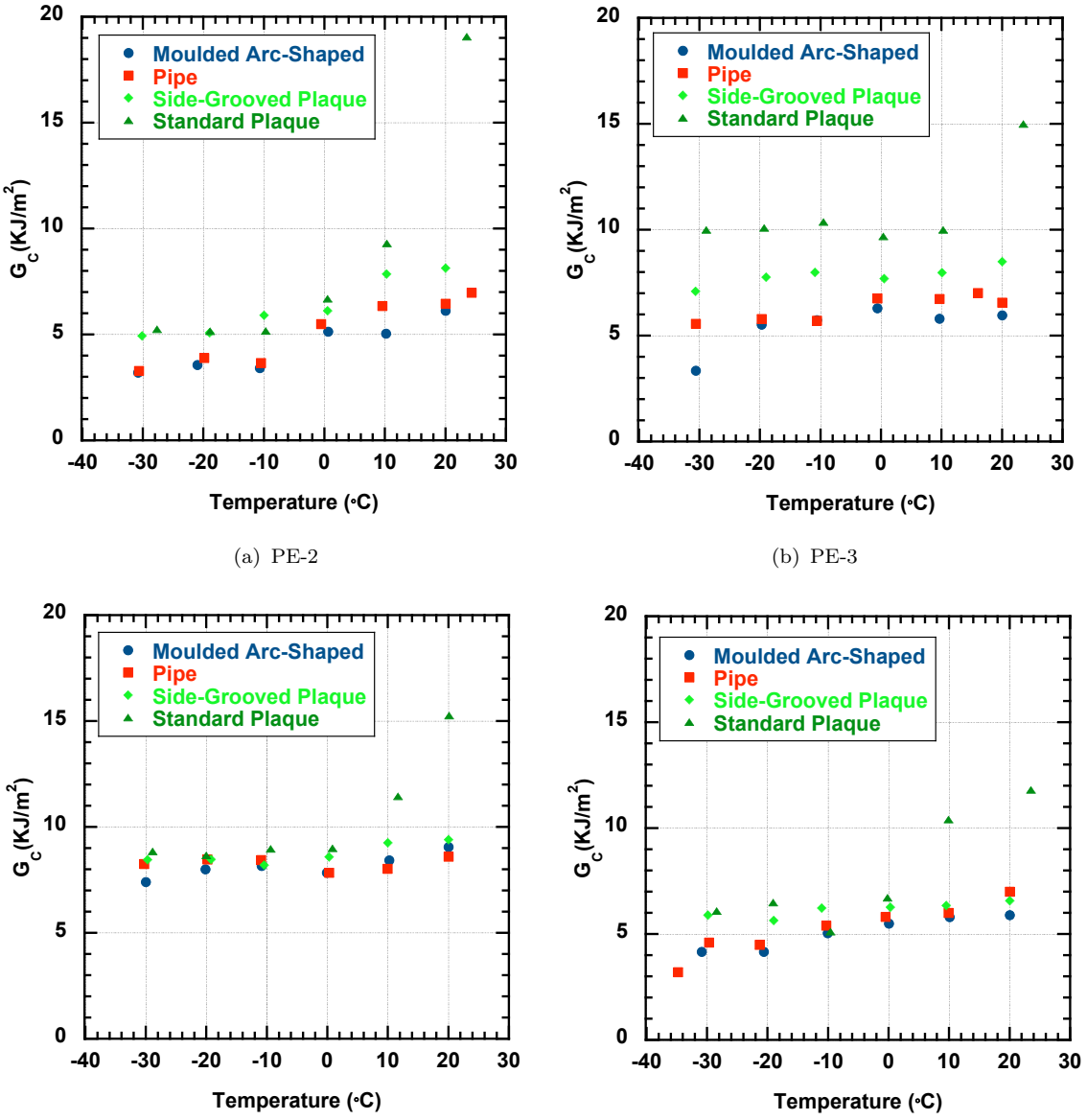


FIGURE 5.17: Processing, Geometry and Plane Stress Effects on Load Displacement Curves: (a) Effect of Processing (PE-3) (b)Effect of Processing (different cooling rates) (PE-4) (c) Effect of Geometry (PE-6) (d) Effect of Plane Stress (PE-4)

5.3.1.4 Impact Fracture Resistance (G_c)

The effect of temperature on G_c results can be seen clearly in Figs. 5.18 and 5.19 for each PE sample.



(a) PE-2

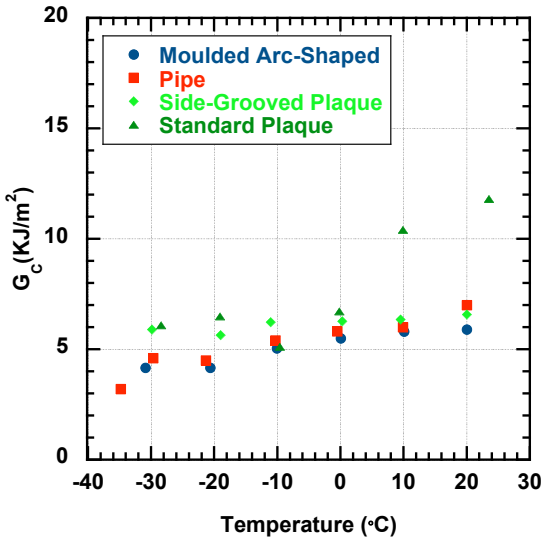
(b) PE-3

(c) PE-4

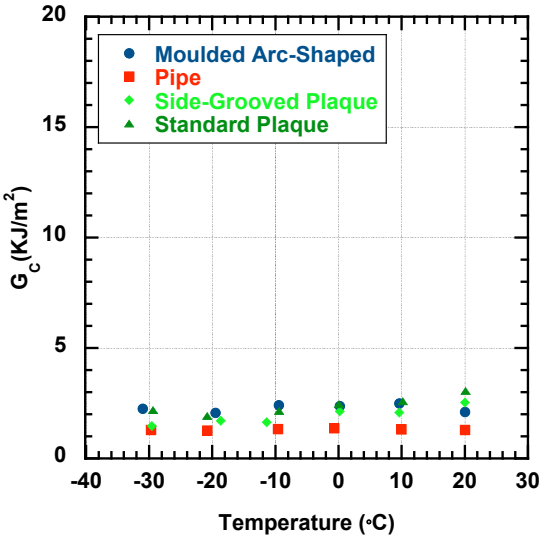
(d) PE-5

FIGURE 5.18: Impact Fracture Resistance (G_c) versus temperature plots of C Series PE resins

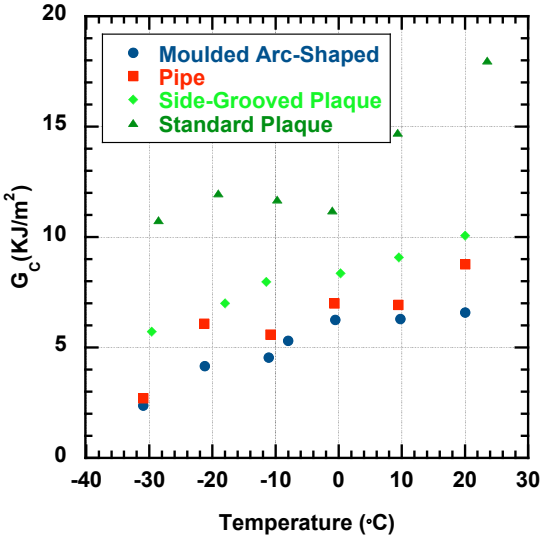
By observing Figs. 5.18 and 5.19, it can be seen that the G_c values are much higher at 10 °C and 20 °C for most of the materials. This can be attributed to the high ductility of these materials at these temperatures and possible errors in the



(a) PE-6



(b) PE-7



(c) PE-8

FIGURE 5.19: *(Cont.)* Impact Fracture Resistance (G_c) versus temperature plots of C Series PE resins

determination of G_c due to the nature of ductile load-displacement figures (this will be discussed in detail in Section 5.3.1.4).

On the other hand, a slight increase in G_c with increasing temperature is expected and can be explained by refering to thermal decohesion model (Section 3.1.2.3). As given in Eq. 3.17, this model predicts that when other factors are constant, G_c is proportional to $E^{-1/3}$. Since temperature increase results in a decrease in E, G_c is expected to increase according to the model, as is observed experimentally.

Based on this, PE-7 having the lowest G_c is not surprising since it has the highest E (as seen in Fig. 5.15).

Although the trend of decreasing G_c with increasing E can be explained by this model, the proposed relationship is not observed. As seen in Fig. 5.20, the slope is around -3.5 opposing to the proposed slope value of -0.33. Based on this, it would not be wrong to conclude that thermal decohesion model does not fully explain all the variations in G_c and some more studies are required in the area.

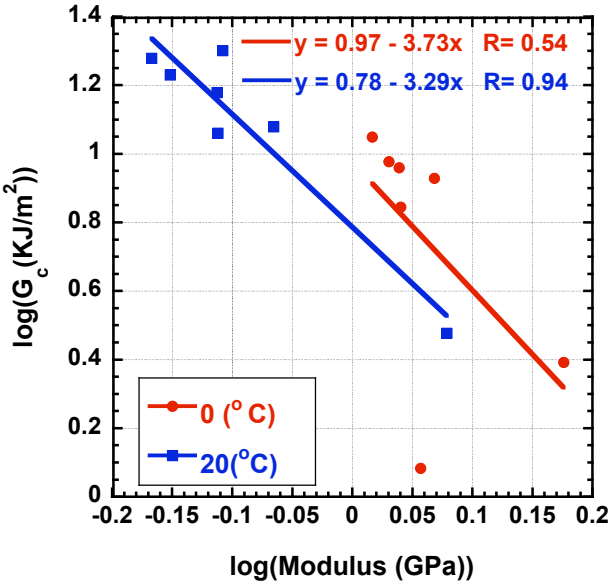


FIGURE 5.20: Relationship between G_c and Modulus

Effect of processing conditions and geometry

G_c *vs.* temperature plots were compared within each material to see the effect of processing conditions. As can be seen in Fig. 5.22 (only two of the materials' results are plotted for simplicity), taking the error range into account, it can be concluded that crystallinity does not have a major influence on G_c. A slight decrease in G_c is observed with decreasing cooling rate or in the case of moulded arc-shaped specimens. Both of these can be related to the high crystallinity of these samples. Moulded arc-shaped specimens are prepared from a sector-shaped plate mould by machining the inside of the arc. And as can be seen in Fig. 5.21,

the impacted section comes from the middle of the mould (depth-wise), which had been cooled more slowly when compared with the surface.

Slow cooling improves crystallinity, while rapid cooling, decreasing crystallinity, increases tie molecule concentration [74]. The low crystallinity promotes a lower yield stress, making the initiation of the damaged zone easier. Once initiated, the damage zone fibrillates and subsequent initiation of a crack would be difficult. This is attributed to the drawing ability and strength of the fibrils, which was suggested to depend on the rate of disentanglement of fibrils [75], controlled by tie-molecules. Thus more energy will be absorbed in this zone and G_c will be increased.

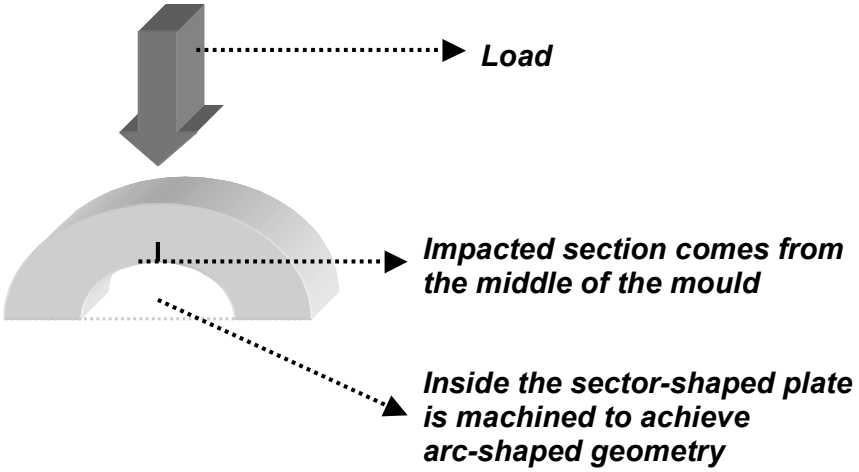
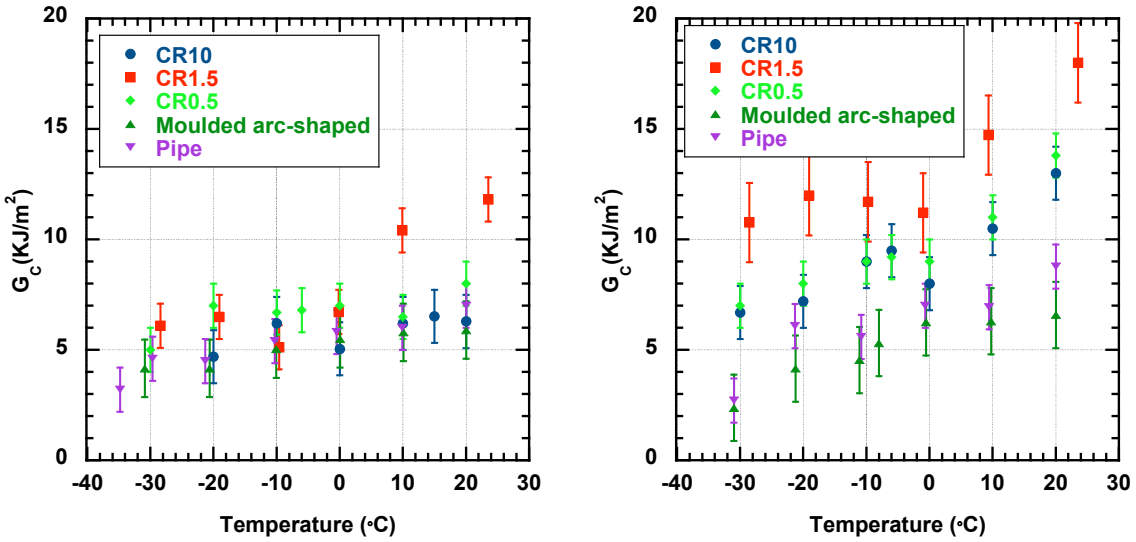


FIGURE 5.21: Moulded arc-shaped specimens

Investigation of scatter

The cause of the observed scatter (in Fig. 5.22) is investigated by testing specimens from the same plaque while keeping the test conditions the same (23°C, 1 m/s). Initially it was thought that the cooling process might have been nonuniform during plaque processing. In order to keep track of this, PE-6 and PE-8 specimens were numbered prior to being cut from the plaque and the obtained G_c values were compared. Resulting G_c values are shown in Figs. 5.23-5.24 in correspondence with their relative places on the plaques. The standard deviation was found to be 1.13



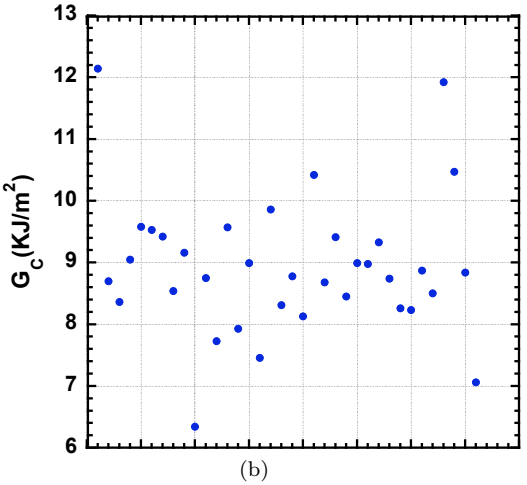
(a) PE-6 (b) PE-8

FIGURE 5.22: Effect of processing conditions on G_c

(for PE-6) and 1.75 (for PE-8) where the mean values were found to be 8.90 and 12.20 respectively. The outstanding G_c values are highlighted and it is observed that the majority of these come from the edges of the plaques. Having observed this difference in the edge-samples, the remaining errors can be categorised as experimental, occurring during testing or measurement of the specimens.

12.14	10.42				
8.70	8.31				
8.36	8.78				
9.05	8.13	8.50	8.87	8.23	8.26
9.58	9.88				
9.53	8.68				
9.42	9.41				
8.54	8.45				
9.16	8.99				
6.34	8.98	7.06	8.84	10.47	11.92
8.75	9.33				
7.73	8.74				
9.57	8.26				
7.93	8.23				
8.99	8.87				
7.06	8.50				

(a) Plaque of PE-6

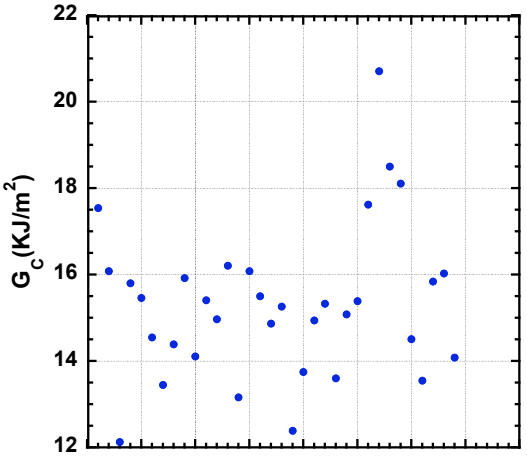


(b)

FIGURE 5.23: Investigation of Error range in G_c, PE-6

17.54	12.39			
16.08	15.50			
12.13	14.87			
15.80	15.26	13.55	14.51	18.11
15.46	12.39			
14.55	13.75			
13.45	14.94			
14.39	15.33			
15.92	13.60			
14.11	15.08	14.08	16.03	15.84
15.41	15.39			
14.97	17.62			
16.21	20.71			
13.16	18.50			

(a) Plaque PE-8



(b)

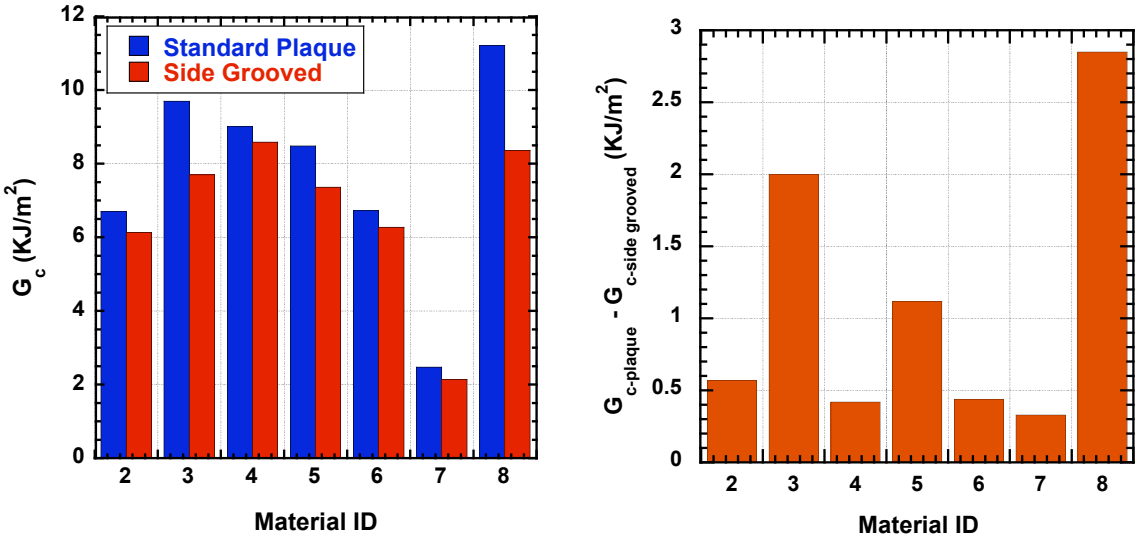
FIGURE 5.24: Investigation of Error range in G_c, PE-8

Effect of Side-Grooving

As was already observed in Fig. 5.17(d), side-grooving eliminates the effect of shear lips in the energy absorption mechanism while having the same peak point. But as can be seen in Fig. 5.25(a), in most cases, G_c values are lower for side-grooved specimens. (Figure 5.25(b) shows us that the material that is affected the most is PE-8 followed by PE-3, while PE-7 is hardly affected.) This might be related to a possible error in the determination of G_c. In some cases, where high ductility is observed (especially in higher temperatures), the load signal up to peak point does not exhibit a linear behaviour, but a curve instead (as can be observed in Fig. 5.26). The area under the curve giving the G_c value is based on the assumption that the specimen will load linearly up to the peak point, exhibiting a triangular area as stated in the ISO Standard. But, in the case of a curved load-displacement signal, the energy value calculated by taking the area under the curve will include the *excess section* leading to incorrect results.

Effect of Molecular Weight

When it comes to fracture resistance properties of a material, MW is one of the main factors playing an important role [21, 76]. Having very different properties within the group, the C-Series of PE resins was not designed to study the effect of



(a) Effect of side grooving on G_c values

(b) Change in the G_c values when a standard plaque specimen is side-grooved

FIGURE 5.25: Effect of processing conditions on G_c

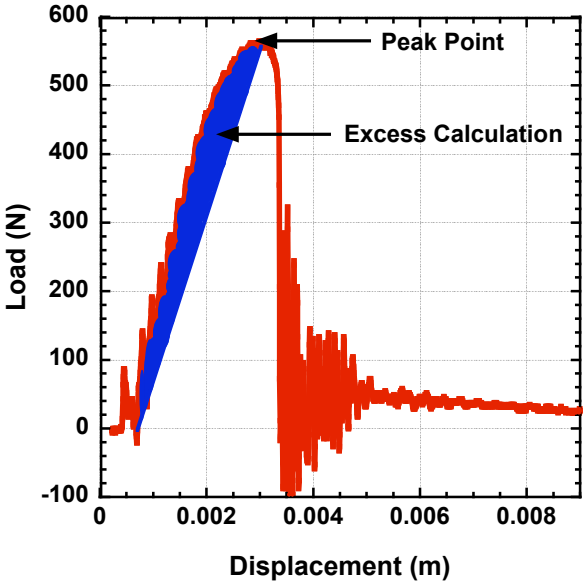


FIGURE 5.26: Possible error in determination of G_c (demonstrated for PE-3, 20°C)

MW. Yet, when it is investigated, a relationship was found as given in Fig. 5.27. At low MW, there is a kind of linear relationship observed up to a certain point, above which G_c stays almost constant.

Prentice [77] studying PMMA had also observed similar behaviour and related this to a model of crack propagation, which is considered to be related to a pull-out

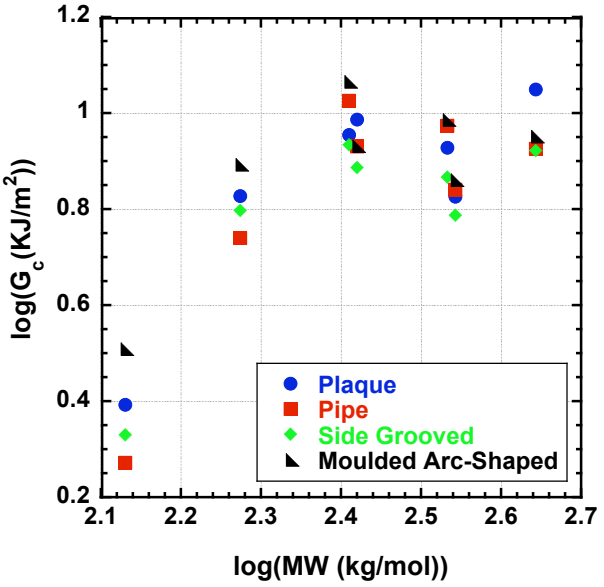


FIGURE 5.27: Effect of M_W on G_c values, 0°C

mechanism up to a critical chain length. As the MW increases, the increasing entanglements restricts the movement of chains, and after a certain MW value, it becomes more difficult, above which it stays constant, as does the G_c value [77].

5.3.1.5 Brittle-Tough Transition Temperature Analysis

The results obtained from different T_{BT} measurement methods explained in Section 5.2.1 were found to agree within an error range of ±1.5°C for all specimen types tested.

The results plotted in Fig. 5.28 show that the general ranking is the same for all materials in terms of the effects of the process/geometry conditions. It is seen that the best performance is obtained from slow cooled standard plaque specimens, CR 0.5, followed by CR 1.5.

The moulded arc-shaped specimens have higher T_{BT} values than plaque specimens (CR1.5), leads to the conclusion that arc-shaped geometry has a negative effect. This might be related to a previous study in the area by Leevers *et al.* [46], where crack arrest is considered as a competition between RCP driving energy in the specimen, and the energy absorbed by the shear lips. The arc-shaped specimen

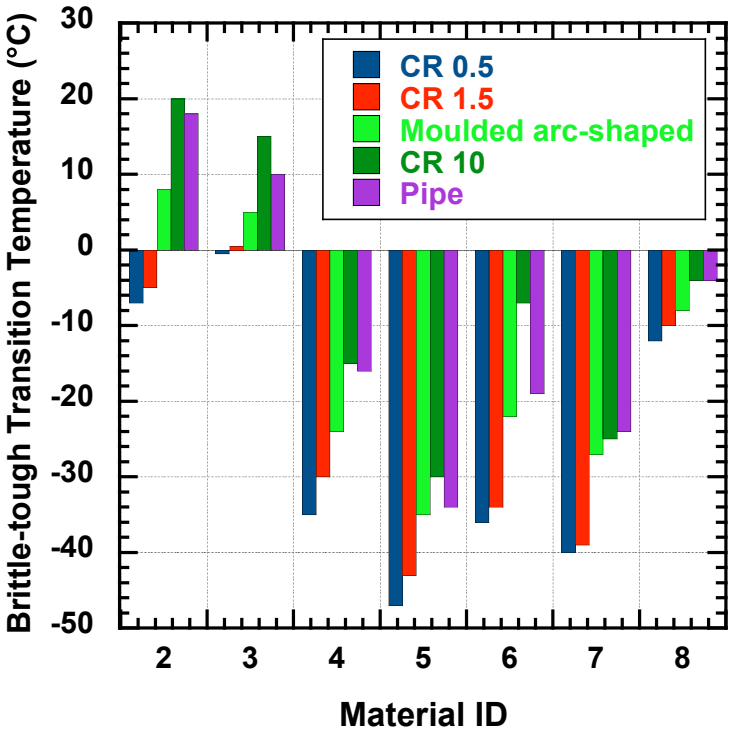


FIGURE 5.28: Comparison of T_{BT} Values for C-Series PE resins

being more compliant (as can be seen in Fig. 3.11) has a higher ϕ, resulting in a higher energy storage. To stop a crack in this type of specimen requires more energy absorption by the shear lips, and effectively higher temperature [46].

Pipe specimens show the next highest transition temperature, and the highest of all is observed in the case of CR 10 plaque specimens.

To sum up, we can conclude that slow cooling rate improves the brittle-tough transition temperature and the arc-shaped geometry shows a higher transition temperature than the rectangular geometry. Similar studies that have been done previously also showed that slow cooling results in a decrease in T_{BT} [61, 68].

Pursuing the study further, T_{BT} results found here are compared with the given S4 T_c results in Fig. 5.29, since one of the aims of this study is to find a smaller scale test for the determination of pipe performance. The best correlation is obtained from the arc-shaped specimens. A previous study by Clutton *et al.* [78] showed a reasonable agreement between these two test methods and further studies were

done by Krishnaswamy *et al.* [73]. The correlation obtained in each case was different indicating that it is dependent on the material group tested and on the cooling rate applied. It is also not clear whether the same specimen size has been used in each case. So, it is not possible to define a direct relationship between the two test results.

This is an expected result due to the nature of the RCP behaviour. RCP in pipe is resisted by two distinct modes, one under plane strain conditions leading to a brittle surface and one under plane stress conditions leading to a ductile surface. The same is true for an impact specimen in which RCP has been initiated, but it is difficult to separate the contributions of plane stress and plane strain in stopping the crack. Therefore, finding a small scale test correlating with the S4 results requires taking both aspects into account carefully.

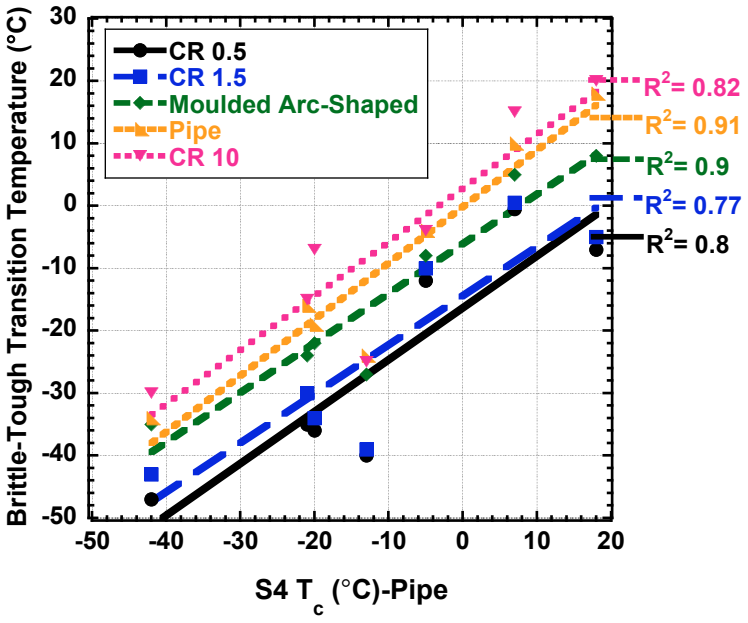


FIGURE 5.29: Comparison of T_{BT} Values with S4 T_c Values

5.3.2 Effect of Density: D-Series PE Resins

In order to analyse the effect of comonomer type on the ductile-brittle transition temperature of polyethylene, four PE batches which were structurally similar but

differed in density, D157, D139, D350, D449, supplied as granulate by Chevron Phillips Chemical Company, were compression moulded into plaques and tested. The information supplied on the materials is given in Table 5.2. (The given density values are being used as proxies for comonomer content, and are not referring to the actual densities of the samples tested here. Additional crystallinity data is given based on Eq. 2.3, where ρ_a and ρ_c are taken as 0.853 and 1.004 g/cm^3 respectively.)

Material ID	**Density (g/cm^3)**	M_w **(kg/mol)**	M_w/M_n	M_z **(kg/mol)**
D157	0.922	128	2.4	230
D139	0.918	116	2.2	205
D350	0.933	136	2.3	256
D449	0.945	139	2.5	266

TABLE 5.2: Molecular Characteristics of D-Series PE Resins

The tensile modulus of the specimens was determined by DMTA, and the results in the range of -60 to 60 °C are given in Fig. 5.30. The relationship between the 0°C modulus values and the density is given in Fig. 5.16, where a kind of linearity is observed.

To see the effect of density on ISO 17281 impact fracture resistance load-displacement traces, Fig. 5.32 is plotted by taking 20°C tests as a reference. The traces are smoothed to remove the effect of oscillations and to make the distinction clearer. From this plot, it can be observed that the initial load gradient shows an increase with density confirming the relationship observed in Fig. 5.31.

When T_{BT} values are analyzed, it is seen that transition temperature decreases with density. This is consistent with the observation that slow cooling (increasing crystallinity) results in lower T_{c-S4} as observed by others [61, 68], and supports the findings in the previous section, where decrease in the cooling rate decreases T_{BT} as well.

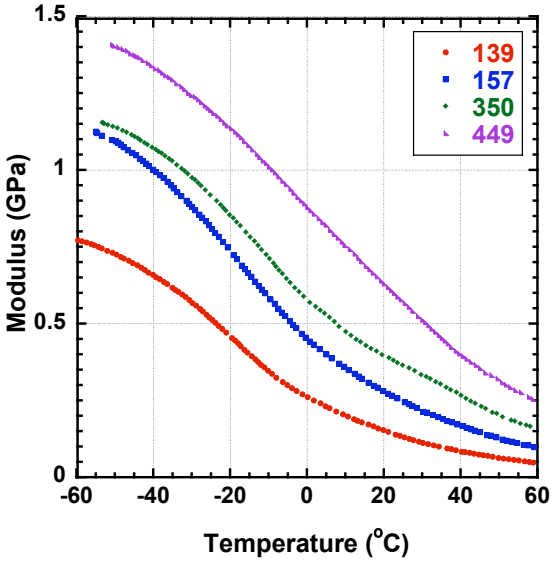


FIGURE 5.30: Modulus (E') versus Temperature for D-Series PE Resins, 10Hz

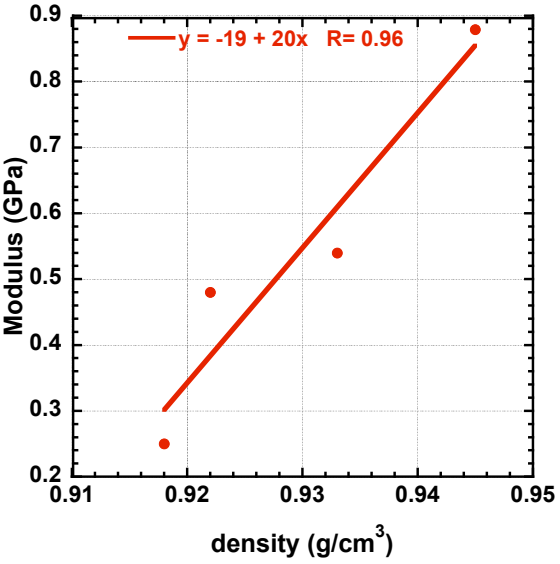


FIGURE 5.31: Modulus (E') (0°C, 10Hz) versus Density for D-Series PE Resins

Figure 5.34 showing temperature *vs.* G_c for each material, enables us to see the effect of density. Observing the increase in E with density in Fig. 5.31, the decrease in G_c with density can be explained by referring to thermal decohesion one more time (Eq. 3.17). Another possible approach would be to relate increasing crystallinity with the decrease in tie molecule concentration, which are the parts absorbing energy when it comes to impact fracture [74]. So, as the crystallinity

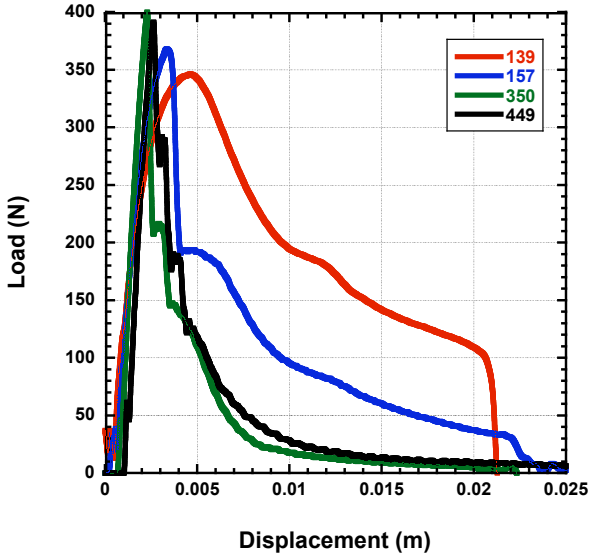


FIGURE 5.32: Effect of density on the load-displacement traces

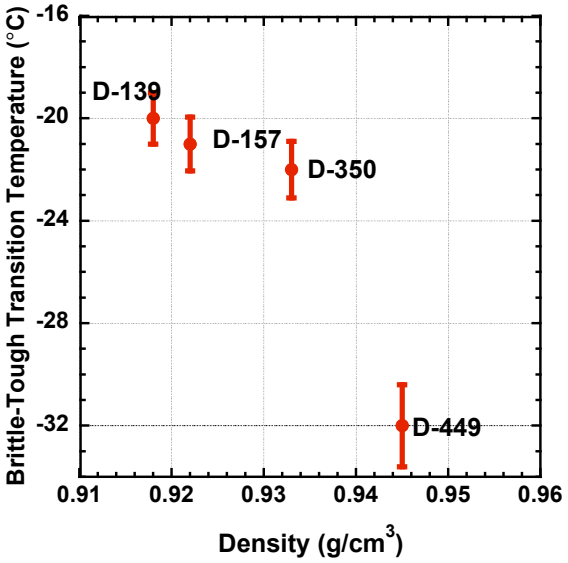


FIGURE 5.33: Effect of Density on Brittle-Tough Transition Temperature

increases, G_c decreases due to the decrease in tie molecule concentration.

5.3.3 Effect of Molecular Weight: MW-Series PE Resins

In order to investigate the effect of molecular weight on the impact properties, three homopolymers, MW-4, MW-5, and MW-6 were prepared by Chevron Phillips

Material ID	T_{BT} (°C)
D157	-21.2 ±1.5
D139	-20 ±1.5
D350	-22±1.5
D449	-32±1.5

TABLE 5.3: Brittle-tough Transition Temperature values of D-Series PE Resins

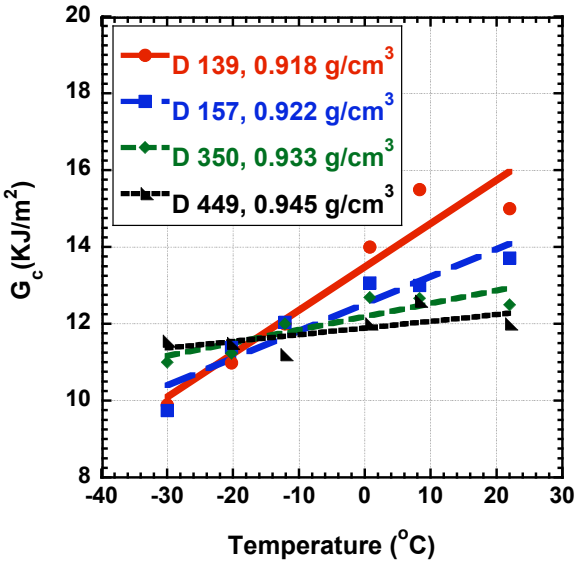


FIGURE 5.34: Effect of Temperature on G_c for D-Series PE Resins

Chemical Company and supplied in granular form. The relavant information on the materials is given in Table 5.4.

Material ID	M_w (kg/mol)	M_w/M_n	M_z (kg/mol)
MW-5	191	3.1	438
MW-6	303	3	689
MW-4	409	3.4	901

TABLE 5.4: Molecular Weight information of Polymer Resins

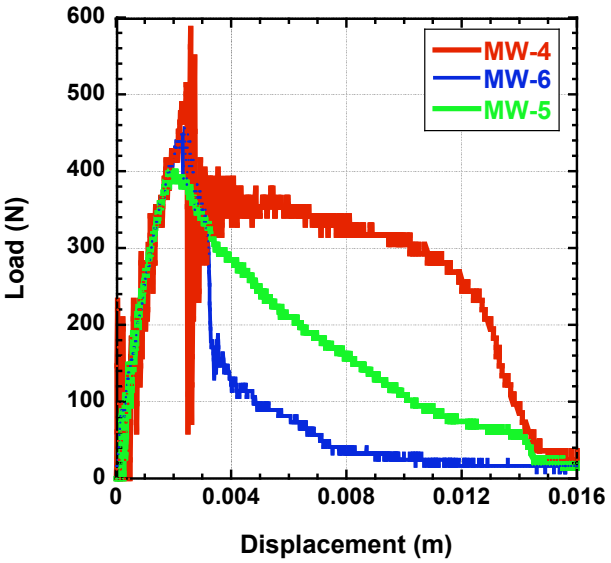


FIGURE 5.35: Effect of M_w on impact load-displacement traces at 0°C

As seen from the load displacement traces in Fig. 5.35 recorded at 0°C, as MW increases, the area under the curve increases both before the peak load (indicating increasing G_c) and in total (indicating increasing shear lip resistance). The increase

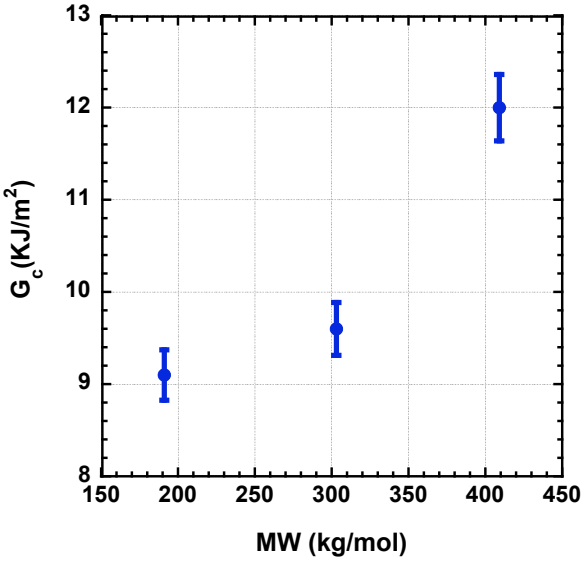


FIGURE 5.36: Effect of M_w on the load-displacement traces

in G_c with increasing M_w, shown in Fig. 5.36 (for simplicity and consistency, 0°C values are given), was also observed in the C-Series. The effect of MW on G_c becomes more dominant at the higher MW range. As previously studied [21, 75],

in polyethylene, the influence of increasing MW is to increase the concentration of tie-molecules spanning the amorphous regions, which effectively increases the toughness of the material. The increase in the entanglement density is the major factor in terms of influencing G_c values [21, 76].

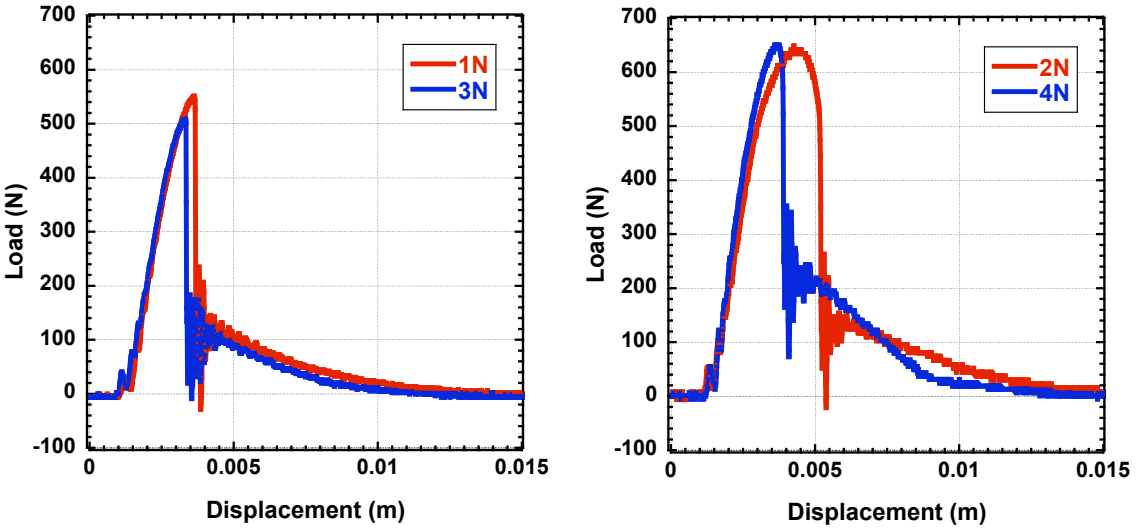
All MW-series materials were found to be highly ductile even at -35°C. Due to the lack of material, T_{BT} could not be determined within the given conditions.

5.3.4 Effect of Carbon Black Dispersion

In this study, the effect of carbon black addition was investigated by testing materials that are identical except for their carbon black content. Materials 1N and 2N are each modified by adding 2.5% CB, resulting in materials 3N and 4N respectively, supplying two pairs for the comparison study. These materials received in pipe form (having 59 mm OD with an SDR of 11) were compression moulded into plaques using hot press. In order to isolate the influence of CB effect, all tests were performed before any UV exposure.

From the load-displacements plots given in Fig. 5.37, it can be observed that the first pair, 1N-3N, behave very similarly under impact, while 2N-4N behave very differently. In the latter case, 2N exhibits a wider area under the curve leading to a higher energy absorption. This leads to the G_c results given in Fig. 5.38.

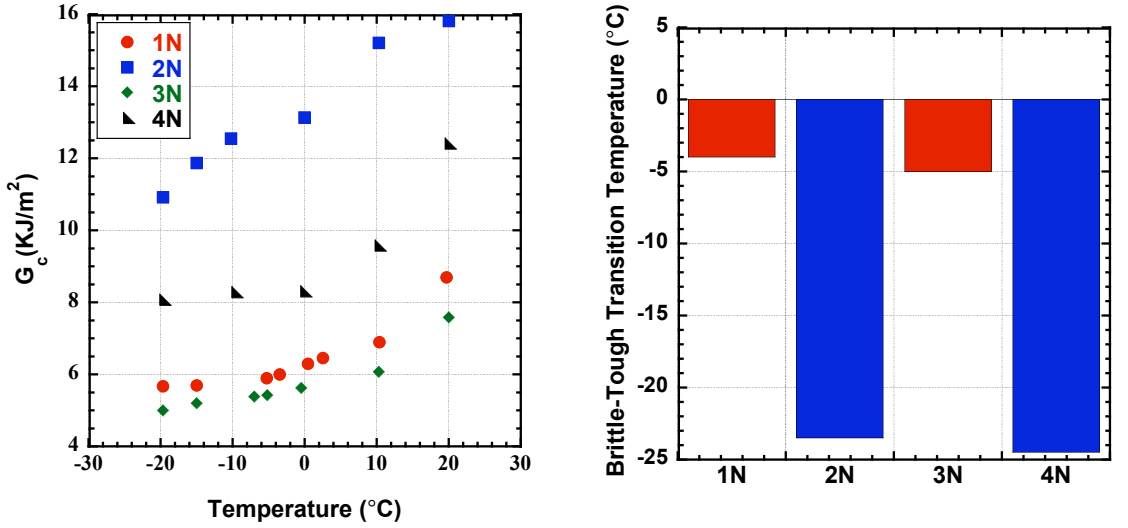
In both cases, the black materials (3N and 4N) have lower G_c and T_{BT} values. But on the scale of the changes, it can be concluded that CB does not have a significant effect on the material performance with the exception of the G_c value in the case of 2N and 4N. Unfortunately due to the lack of information on the material properties, the reasons of the observed results could not be investigated any further.



(a) 1N-3N

(b) 2N-4N

FIGURE 5.37: Effect of CB addition on impact load-displacement traces at 20°C



(a) Effect of Carbon Black on Impact Fracture Resistance Value

(b) Effect of Carbon Black on Brittle-Tough Transition Temperature

FIGURE 5.38: Investigation of Carbon Black Effect

5.4 Discussion & Conclusions

Although ISO 17281 impact bend tests seem to be easy and straightforward, extensive work is required on experimental procedures and data analysis, since dynamic effects may obscure the actual load experienced by the crack. Detailed analysis is necessary in order to obtain precise and informative results.

Since this study mainly consists of comparisons within the specimen groups or the effects of certain variables on the resulting material performances, it was ensured that all the cases were treated the same following the appropriate standards.

As stated before, the main aim of this chapter is to investigate the effect of processing conditions, geometry, crystallinity, density, molecular weight and carbon black addition on the impact fracture resistance and transition temperature values.

G_c as a material property is the crack driving force at which unstable fracture initiates. For a parameter to be a material property, it must have the same value in different specimen geometries. This is why arc-shaped specimens were studied for the determination of correct geometry factor and then used experimentally alongside the usual rectangular ones.

Based on the findings of this study, Table 5.5 summarises the effect of structural changes on the ISO CD 17281 Impact Bend Test parameters.

Parameters	G_c	T_{BT}
Crystallinity ↑	very slight ↓	↓
Density ↑	↓	↓
Molecular Weight ↑	↑	n/a
Carbon Black Addition ↑	↓	↓

TABLE 5.5: Effect of structural changes on ISO CD 17281 Impact Bend Test parameters

Realising the importance of shear lip energy absorbing capacity, the next step will be to investigate plane stress mechanism in detail. Following this aim, Reversed Charpy and Tensile Testing techniques will be introduced, using which it was attempted to define and determine the plane stress resistance.

Chapter 6

Reversed Charpy Test

PE, like many thermoplastics, has a relatively little resistance to plane strain at crack speeds exceeding 100 m/s and temperatures below 0°C. On the other hand, the plane stress region adjacent to each free surface continues to resist even at high speed and low temperatures. The ductility and volumetric nature of deformation here is indicated by deep stress whitening and a pronounced shear lip. Two shear bands develop from each side of the ligament; while one shear band develops resulting in two matching specimen pieces after fracture.

The mechanism is largely governed by the post-yield drawing behaviour of PE and is sensitive to both rate and temperature [68, 79, 80]. As the test temperature decreases, it is observed that the volume of the material that is subject to the deformation decreases. If the plane stress plastic zone is wide enough and sufficiently ductile at high rates, the pipe wall thickness as a whole will be able to arrest RCP. If plane stress is suppressed by notching [79] or otherwise, RCP resistance will be seriously reduced.

Founded on these, it would not be wrong to conclude that the brittle-tough transition is related to the presence of the shear lips. Shear lips form above T_{BT}, resulting in a ductile manner of fracture. Below T_{BT}, shear lips are not observed, while the manner of fracture is brittle.

Recognizing the importance of shear lips, one must understand this mechanism to be able to bring a full explanation to the RCP behaviour. Although plane strain fracture is well characterised using concepts and methods of fracture mechanics [48], no test method for plane stress conditions had yet gained general acceptance. The instrumented Charpy test on thin specimens (as suggested by Harry and Marshall [81] and developed by Brown [82]) has some disadvantages with respect to investigating shear lips. The process is not steady state, the shear lip formation rate and thickness are controlled by the growth of internal brittle cracks and the results therefore cannot be used to predict quantitatively how the pipe T_{c-S4} will change with pipe wall thickness. This led to the development of another technique: Reversed Charpy Test.

Aiming to study shear lips in isolation, Ritchie [68] introduced the new testing technique which is going to be the subject of this chapter. The aim of this test is to simulate shear lip growth during rapid fracture of pipe material, while reproducing the geometry, constraint and rate under which the plane stress zone develops.

Four groups of materials are tested (C-Series PE Resins, D-Series PE Resins, MW Series and Carbon Black Resins) to understand the effect of structural properties in the shear lip energy absorbtion. Process history, density, molecular weight and carbon black effects on the test parameters are investigated and compared.

6.1 Experimental Method

As shown in Fig. 6.1, specimens that are notched to about 85% of their depth, are placed in a *reversed* position relative to the striker in comparison with a normal Charpy test. They are impacted at an offset distance from the center, in order to promote consistently asymmetrical shear lip growth of the specimen.

The aim of this test is to measure the resistance to separation of the surface layer of the polymer material under rapid extension adjacent to a planar crack. This is expressed as plastic work dissipation, w_{pl}, work per unit volume, which

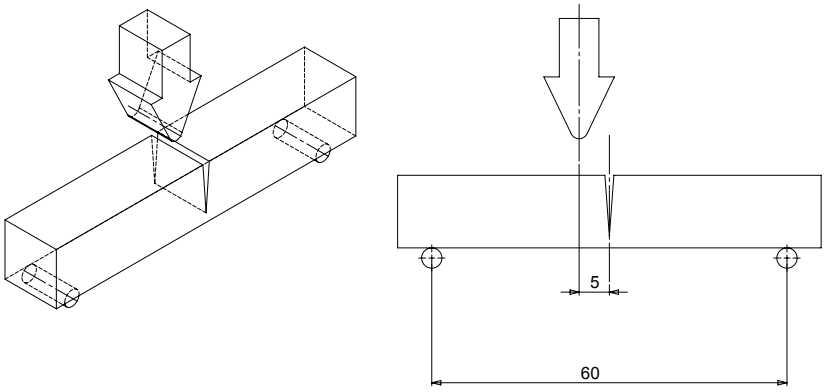


FIGURE 6.1: Reversed Charpy Test arrangement

is used to describe the plane stress fracture by Ward and coworkers [26] and by Hillmansen [80]. As proposed by Ritchie [68], the Reversed Charpy test is a method of measuring w_{pl} at high rates and as a function of temperature.

The notching of the Reversed Charpy specimens should be done carefully in order to avoid plasticity effects at the tip of the notch that may affect the results. Related studies are done on the notching technique as a part of this study and will be discussed in the experimental sections. The maximum ligament size is $W/4$, which is to limit the stress on the upper surface of the specimen. The notched area of a specimen represents a brittle crack whereas the volume under the notched bit, which is the ligament, represents the rapid crack propagation.

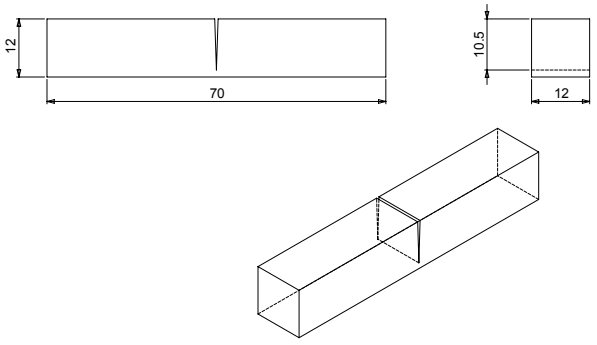


FIGURE 6.2: Rectangular Specimen

Two types of specimens are used in this study: specimens from moulded plaques with the dimensions of $12(B) \times 12(W) \times 70(L)$ mm and specimens directly cut

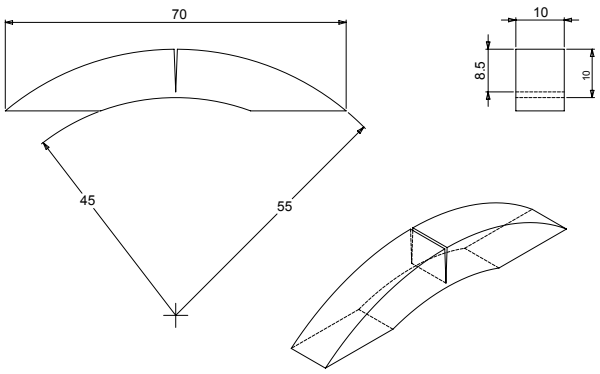


FIGURE 6.3: Arc-shaped Specimen

out of pipes with dimensions of $10(B) \times 10(W) \times 70(L)$ mm. All the experiments were performed with a span (S) of 60 mm, using symmetrical configuration at varying temperatures between room temperature, 20°C and -30°C and 3 repeats for each sample was done at each temperature. Tests were performed on specimens having a ligament size, l, of 1.5 mm. During the analysis, the data obtained for ligament sizes >2 mm should be discarded since bulk yielding affects the energy absorption.

6.2 Analysis of Reversed Charpy Test

When the nature of the test is observed as it is reflected on a tested specimen, as given in Fig. 6.4, it is seen that the ligament resists separation by drawing. During testing; the ligament extends, whitens and its width decreases in the centre. In Fig. 6.5, there are series of pictures taken during a test enabling us to see the effect of temperature on plane stress resistance behaviour. The first row of pictures taken at 0°C, shows less ductility when compared with the second row of pictures taken at 20°C. From this observation, we can conclude that as temperature increases, more ductility leads to more energy absorption during the separation of the ligament, resulting in an increase in the plane stress fracture resistance value. So prior to any calculations, plane stress fracture resistance value is expected to increase with temperature as will be confirmed by the experimental results given in Section 6.3.

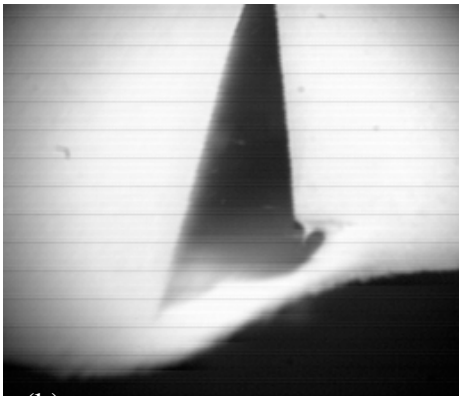


FIGURE 6.4: High speed photographs of specimens during fracture [2]

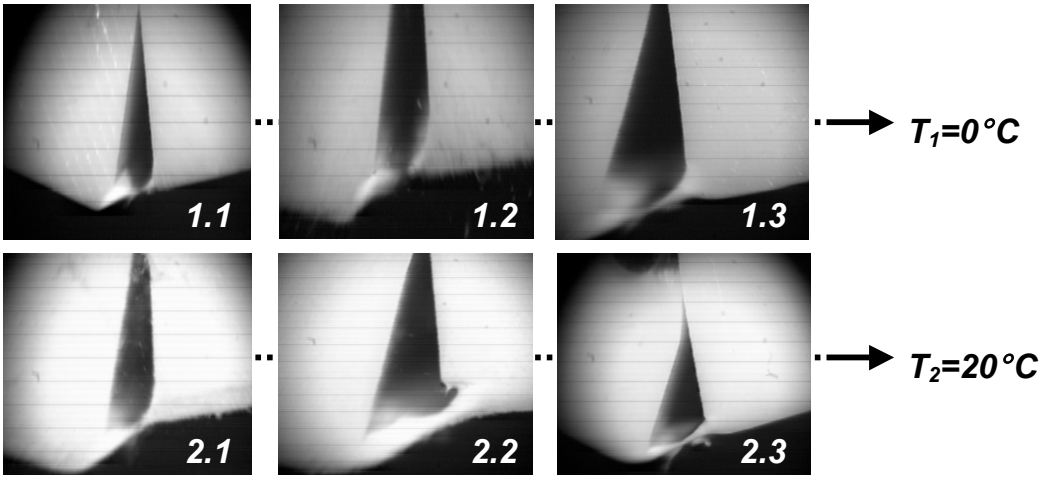


FIGURE 6.5: High speed photographs of specimens during fracture [2]

In order to analyze results from the Reversed Charpy test, the following assumptions need to be made,

- At peak load the presence of shear bands across the ligament suggests a state of uniform tensile stress acting on the ligament, equal to the uni-axial yield stress, σ_y.
- There is no horizontal reaction force from the striker or supports.
- The neutral axis of bending is at the centre of the specimen.

Following these assumptions, the yield stress for symmetric configuration case is given by,

$$\sigma_y = \frac{PS\,(1 - 2c/S)}{4BlW\,(1 - l/W)} \tag{6.1}$$

where S is the span, P is the peak load, c is the striker-notch offset and l is the ligament.

The energy absorbed per unit ligament volume (w_{pl}), which is effectively a plastic work density value, is given by:

$$w_{pl} = \frac{1}{l^2 B} \int_{u_{o1}}^{u_{o2}} P du \tag{6.2}$$

where u_{o1} is the displacement at which load departs from zero and u_{o2} is the displacement at which load returns to zero. The integral part of this equation represents the area under the load displacement curve standing for the total energy required to separate the ligament section. Dividing this term by the volume, w_{pl} parameter is obtained to characterise the materials.

Total energy, calculated from the area under the load displacement curve, is used to calculate the values of w_f, the work of fracture, by dividing the energy values by the cross sectional area of the ligament. The plastic work dissipation, w_{pl}, can be determined by following two approaches. It can either be determined by dividing the w_f value by the ligament value for each case and then taking the average of all; or it can be determined from the slope of the linear fit of the w_f *vs.* ligament size curve, which is to follow the EWF approach that was explained in Section 3.2.1. To be able to get informative results from EWF approach, a wider range of ligament sizes should be tested to get a better defined slope, and since this study is based on the ligament size of 1.5 mm only, it was not possible to apply this method. Following this, for the purposes of this project, the first method is found to give more reliable results and the results presented in the following sections will be based on this method.

6.3 Experimental Results

Reversed Charpy test parameters (w_{pl} and σ_y) are calculated based on the load-displacement signals received during the tests. Figure 6.6 represents a typical load displacement trend for one material at various temperatures. As can be seen, the ductility of the curve decreases with decreasing temperature. At lower temperatures, load shows a sharp drop representing brittle behaviour. In this case not all of the area under the curve necessarily represents energy absorbed in fracture and the results must be rejected.

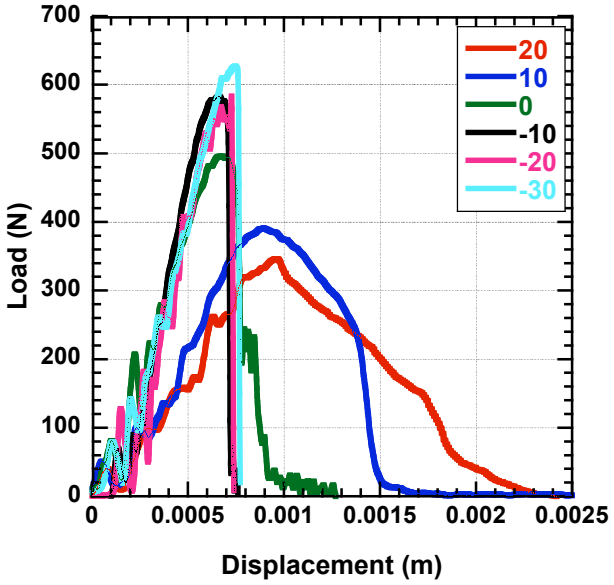


FIGURE 6.6: Reversed Charpy Load-Displacement Trend

6.3.1 Effect of Notching Technique

The initially suggested notching technique of using a slitting saw by Ritchie [68] was observed to deform the ligament and it was suspected that this might affect the amount of energy absorption during the test. In order to investigate this, specimens were prepared by two notching techniques: notching by slitting saw and notching by razor blade. Figure 6.7 shows the load-displacement curves for both cases. It can be seen clearly that frictional heating by slitting saw affects the material properties and reduces its energy absorption capacity. All subsequent

tests were done on razor-notched specimens and the results presented here are based on these tests.

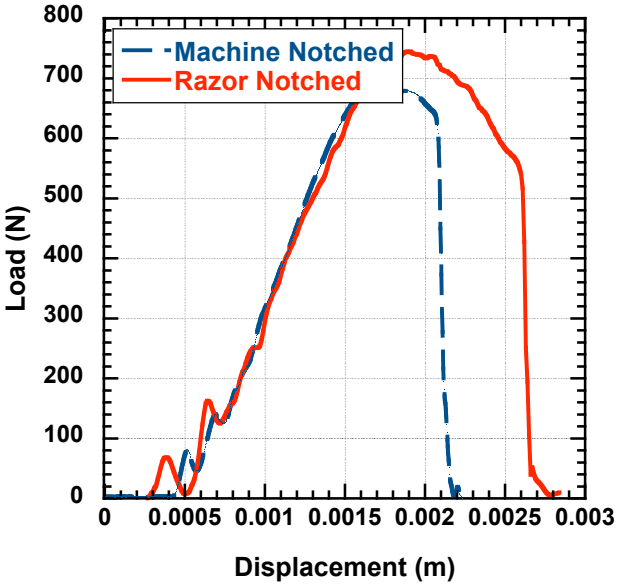
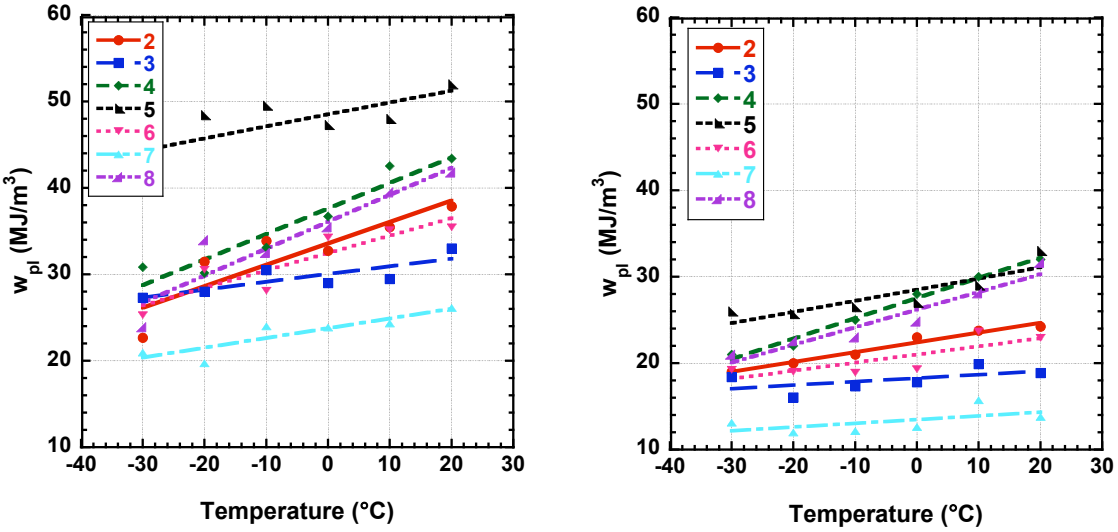


FIGURE 6.7: Effect of Notching Technique on the Load-Displacement Trace

6.3.2 C-Series PE Resins

Plane stress fracture resistance (w_{pl}) and yield stress (σ_y) values obtained from the experiments performed on C-Series PE Resins (as introduced in Section 5.3.1) are plotted in Fig. 6.8 and Fig. 6.9 showing the effect of temperature on the parameters. As can be seen, the resistance to separation increases with increasing temperature while the yield stress decreases. The increase in w_{pl} with temperature corresponds to the increasing influence of plane stress conditions in fracture as well.

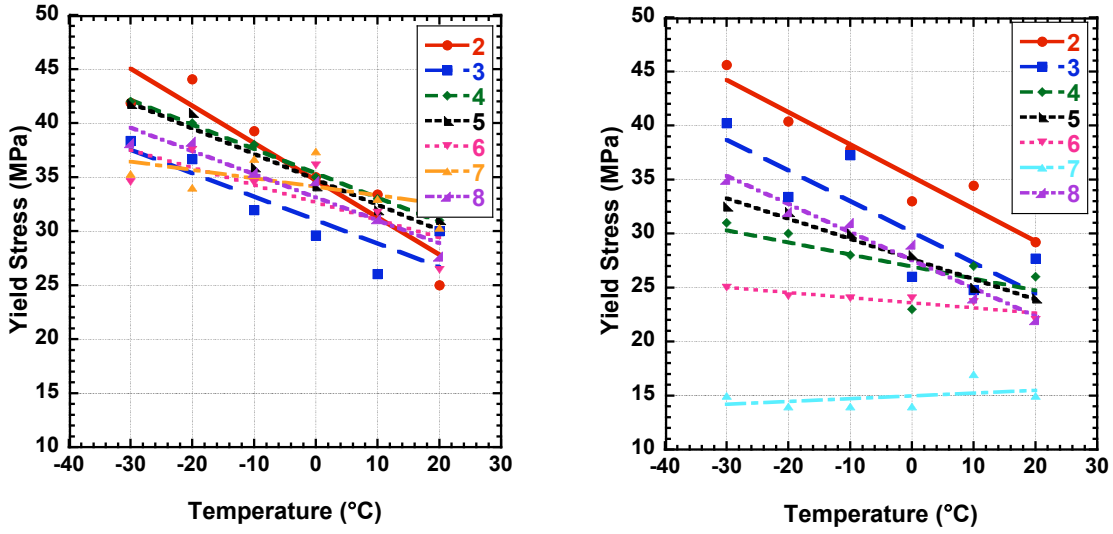
As seen in Fig. 6.10(a), w_{pl} trends are the same for both rectangular specimens (from plaque, CR1.5) and arc-shaped specimens (from pipe), although the values are smaller for pipe samples. This can be explained as an effect of processing conditions and fast cooling rates lowering the crystallinity of the material resulting in lower resistance to separation.



(a) w_{pl} vs. T for plaque specimens (CR 1.5)

(b) w_{pl} vs. T for pipe specimens

FIGURE 6.8: Effect of Temperature on Plane Stress Resistance for C-Series PE Resins



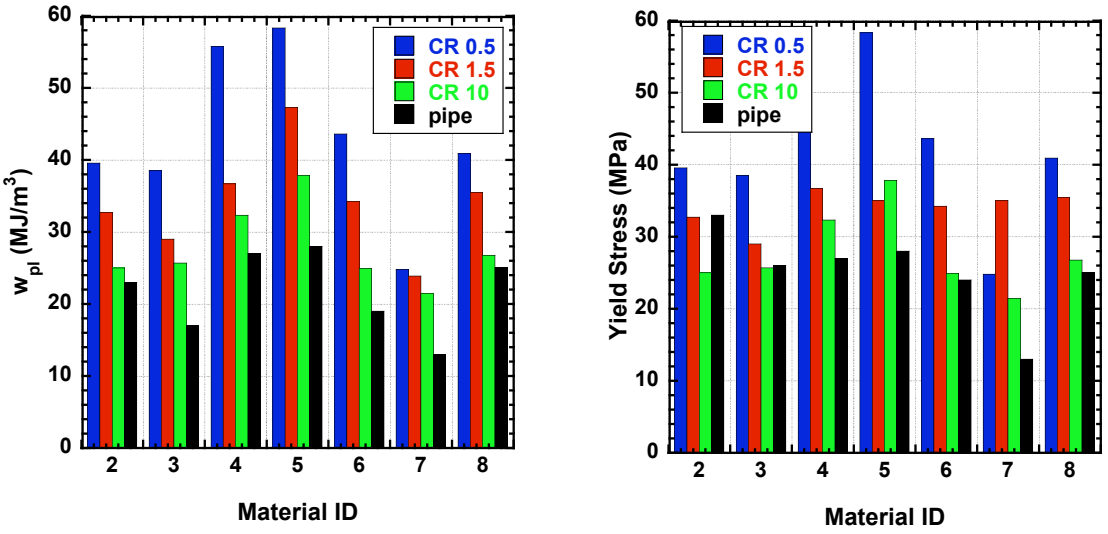
(a) σ_y vs. T for plaque specimens (CR 1.5)

(b) σ_y vs. T for pipe specimens

FIGURE 6.9: Effect of Temperature on Yield Stress

The effect of processing conditions was further investigated by testing plaques that had been processed with different cooling rates using the thermal conditioning press. To follow a comparative study, 0°C values of both w_{pl} and σ_y parameters are plotted in Fig. 6.10. In addition to extruded pipe material, cooling rates of 10°C/min, 1.5°C/min and 0.5°C/min are compared. Figure 6.10 suggests that slow cooling increases the plane stress resistance and yield stress properties of

these polyethylenes, which can be related to the increased crystallinity as a result of slow cooling. This observation will be investigated in greater depth in Chapter 7.



(a) Effect of Processing Conditions on w_{pl} (b) Effect of Processing Conditions on σ_y

FIGURE 6.10: Effect of Processing Conditions on yield stress and plane stress fracture resistance, 0°C

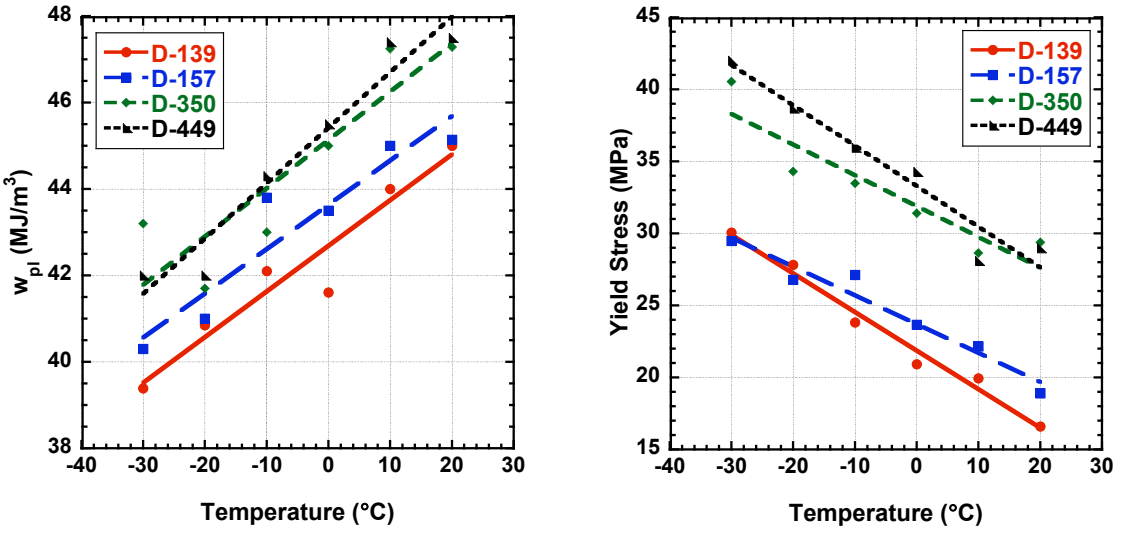
6.3.3 Effect of Density: D-Series PE Resins

Effect of density on Reversed Charpy parameters is investigated by testing D-Series PE Resins, which were introduced in Section 5.3.2. Figure 6.11 shows the effect of temperature on the test parameters where the 0°C values of these parameters are used to plot Fig. 6.12 which enables us to see the effect of density.

Both w_{pl} and σ_y values increase with increasing density. As the density increases more energy is needed to separate the ligament and the yield stress of the particle increase as a result of the crystallinity which agrees with the previous section's cooling rate effects as well.

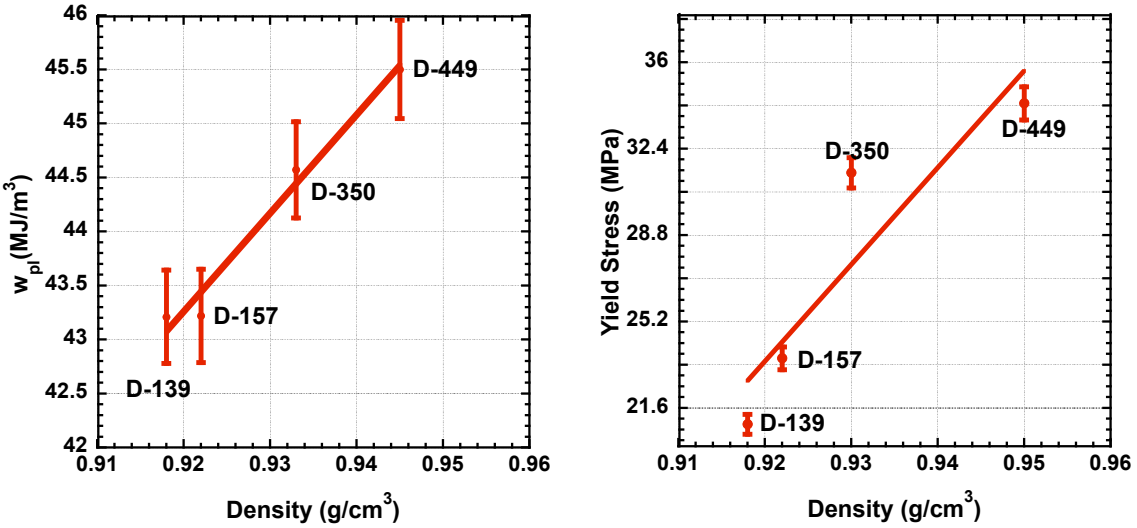
6.3.4 Effect of Molecular Weight: MW-Series PE Resins

The effect of molecular weight was investigated using MW-Series resins, which were introduced in Section 5.3.3. Referring to the load-displacement traces (as given



(a) w_{pl} vs. T (b) σ_y vs. T

FIGURE 6.11: Effect of Temperature on Reversed Charpy test parameters for Density series



(a) Effect of Density on w_{pl} (b) Effect of Density on σ_y

FIGURE 6.12: Effect of Density on Reversed Charpy Test parameters, 0°C

in Fig. 6.13), it is seen that MW-4, having the highest M_W, has both the lowest yield stress and the lowest ductility, whereas MW-5, having the lowest M_W, has the highest. Thus as M_W increases w_{pl} decreases as demonstrated in Fig. 6.14(a). 0°C values of the parameters are used to plot Fig. 6.15 which enables us to see the effect of M_W.

The increased yield stress is expected because increase in M_W is known to lead

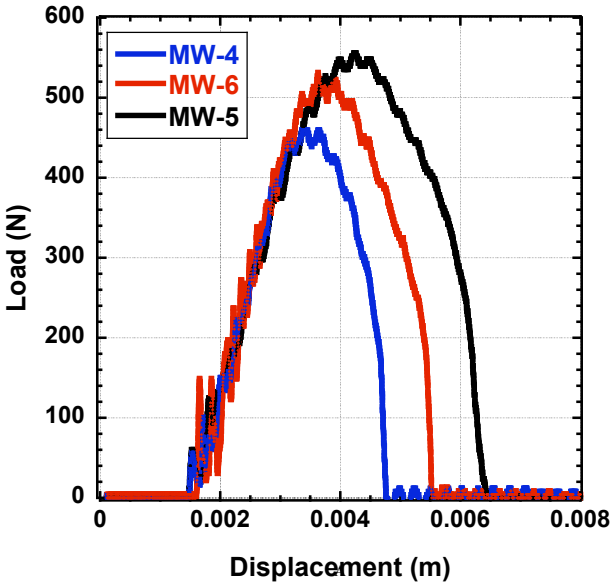
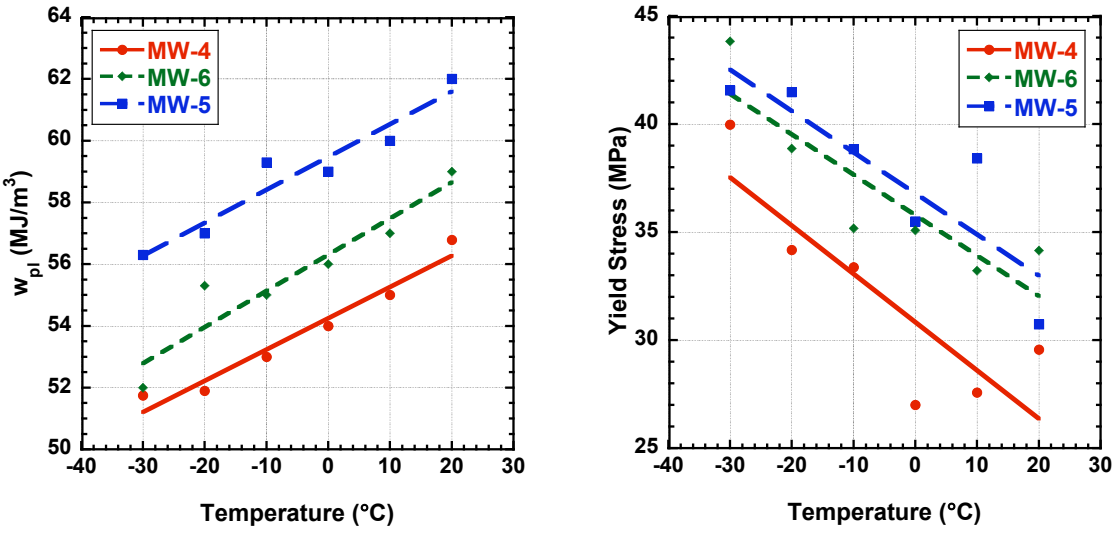


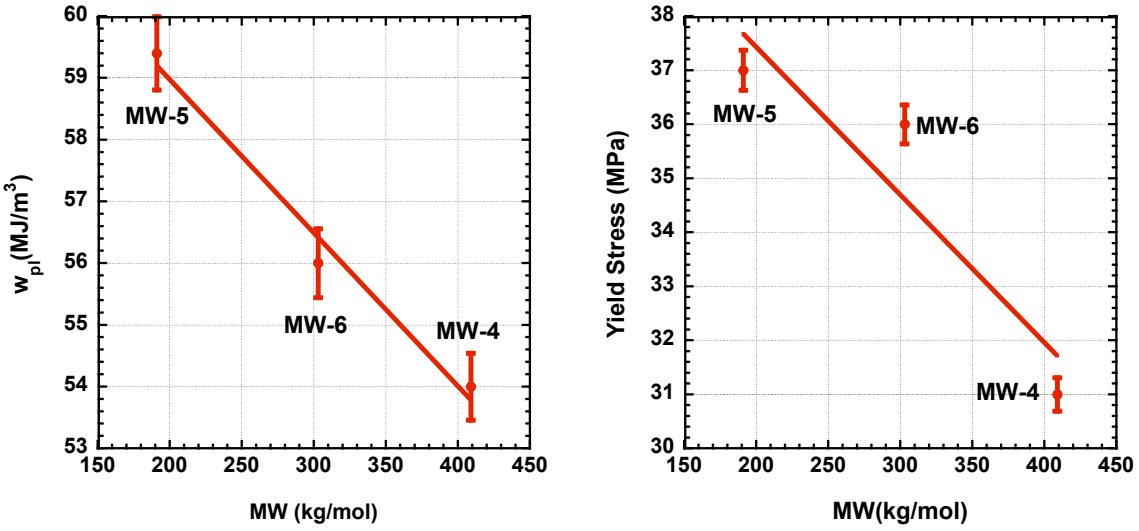
FIGURE 6.13: Effect of MW on Reversed Charpy load-displacement traces

to a slight decrease in the crystallinity [83]. This can be related to the effect of entanglement density. Having high entanglement density increases M_W while decreasing the crystallinity due to their highly disordered structure not being able to form ordered structures.



(a) w_{pl} vs. T (b) σ_y vs. T

FIGURE 6.14: Effect of Temperature on Reversed Charpy test parameters for M_W series



(a) Effect of MW on w_{pl}

(b) Effect of MW on σ_y

FIGURE 6.15: Effect of M_W on Reversed Charpy Test parameters

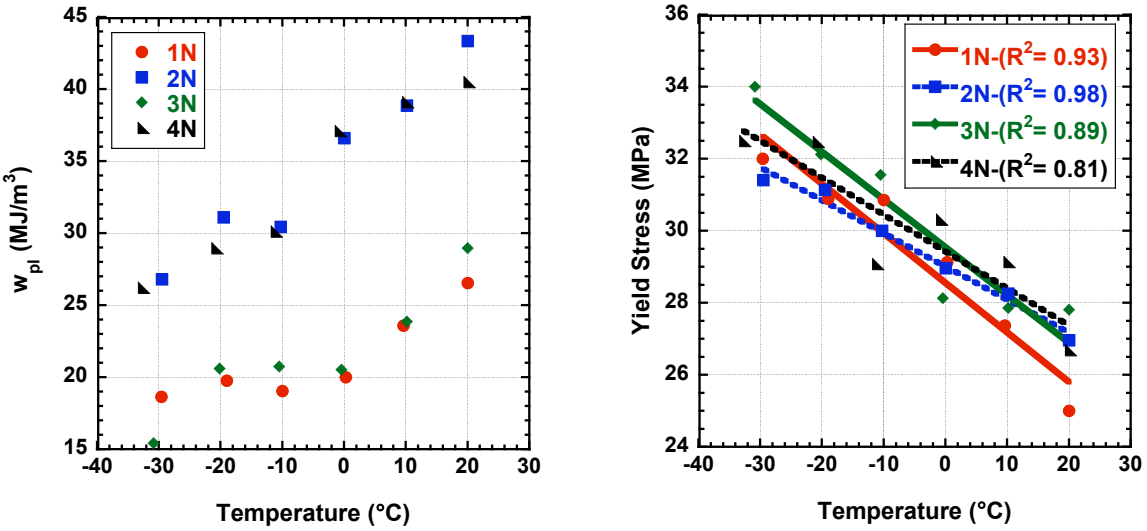
6.3.5 Effect of Carbon Black Dispersion

Reversed Charpy test study on carbon black dispersion showed us one more time that carbon black addition does not have a significant effect on PE performance (Fig. 6.16), which is inline with the results shown in Section 5.3.4.

The plane stress fracture resistance value is the same in both cases, whereas yield stress shows a slight increase with the addition of carbon black. This observation is somewhat surprising since it would have had been expected for w_{pl} to be more sensitive to structural changes when compared to σ_y, but here the opposite is observed. This might be explained by yield stress being counteracted by a change in some other property, related to ductility. Although these possible effects will be discussed in detail in Chapter 7, unfortunately CB series could not be investigated any further due to the lack of time and material.

6.4 Discussion & Conclusions

This chapter investigates the effect of processing conditions, density, molecular weight and carbon black on Reversed Charpy test parameters; namely: plane



(a) Effect of Carbon Black on w_{pl}

(b) Effect of Carbon Black on σ_y

FIGURE 6.16: Effect of Carbon Black additon on Reversed Charpy Test parameters

stress fracture resistance and yield stress values.

Plane stress fracture resistance, w_{pl}, having the dimensions of energy per unit volume in recognition of the volumetric nature of plane stress deformation, increases with temperature and so, though the surface area through which it acts remains small, it comes to dominate the overall fracture resistance.

Although not being the main parameter, yield stress (σ_y), obtained from the test by a simple moment relationship, enables us to link the material performance to a very basic parameter.

Based on the findings of this study, Table 6.1 summarizes the effect of structural changes on the Reversed Charpy test parameters.

An additional proposed approach by Leevers [46], suggests that Reversed Charpy test parameter, w_{pl} can be used to determine T_{BT}. Based on the idea that at the transition point, the crack propagation process is driven by strain energy in the specimen at the point of crack initiation, the model proposes that impact transition temperature can be predicted in terms of bulk property parameters. Combining thermal decohesion equations (Section 3.1.2.3) and plane stress resistance factor, T_{BT} can be determined. Although giving a relatively correct value, this model has

Parameters	w_{pl}	σ_y
Crystallinity ↑	↑	↑
Density ↑	↑	↑
Molecular Weight ↑	↓	↓
Carbon Black Addition ↑	—	↑

TABLE 6.1: Effect of structural changes on Reversed Charpy test parameters

limitations and needs to be improved (*eg.* it does not take the impact speed into account).

6.4.1 Contributions of Plane Strain and Plane Stress Regions to Overall Fracture Resistance

Having obtained both plane strain and plane stress fracture resistance components so far, an additional analysis can be done to see the effect of plane strain and plane stress regions to overall fracture resistance. The interaction between them can be defined referring to Eq. 4.3. If this equation is modified to include plane stress fracture resistance parameter, w_{pl},

$$G_D B = (B - 2s)G_{1D} + 2s^2 w_{pl} \tag{6.3}$$

can be obtained. Replacing G_{1D} factor with G_c (since we have not done any dynamic fracture resistance measurements), the contribution of plane stress and plane strain regions to overall fracture resistance can be compared. Taking a sample material, PE-3, at 0°C (where E= 1.1 MPa, G_c=10 KJ/m^2, w_{pl}=30 MJ/m^3, σ_y=30 MPa, s=1.5 mm and B=12 mm), the plane strain contribution is found to be 7.5 KJ/m^2 while the plane stress contribution is 11.25 KJ/m^2 (where overall resistance is 18.75 KJ/m^2).

Based on this, the plane strain contribution is the 40% of the total fracture resistance. In reality, if correct dynamic fracture resistance value (G_{1D} instead of G_c) was used, this percentage would have been a lot lower, because G_{1D} is much lower than G_c at normal impact speeds. Such as a typical G_{1D} value of 3 KJ/m^2 (usually between 2-4 KJ/m^2) [84] is used, then the plane strain fracture resistance contribution would drop to 16% as expected (where the overall resistance will be 13.5 KJ/m^2). The reason why G_c is higher than G_{1D} is that G_c values were obtained from tests done at 1m/s, while G_{1D} values obtained during RCP is subject to higher rates (100 m/s). Having known that G_c decreases with speed, at those high rates, it would be expected to have a much lower value. One other factor is that G_c is based on the load at initiation, while G_{1D} is the dynamic resistance, being defined when the crack is running.

In order to determine plane stress layer thickness, Irwin [39] suggested that, plane stress plastic zone size, r_p, is given by,

$$r_p = \frac{1}{2\pi}\frac{EG_D}{{\sigma_y}^2} \tag{6.4}$$

Using the G_D value of 18.75 KJ/m^2 obtained from Equation 6.3, r_p is found to be 3.64 mm, while it goes down to 2.62 mm when a more reliable G_{1D} value of 3 KJ/m^2 is used that gives a G_D value of 13.5 KJ/m^2.

	G_{1D} (KJ/m^2)	G_D (KJ/m^2)	r_p (mm^2)	Plane stress %
G_c as G_{1D}	10	18.75	3.64	60
Real G_{1D}	3	13.5	2.62	84

TABLE 6.2: Determination of plane stress plastic zone size and the percentage of plane stress fracture resistance

Equations 6.3 - 6.4 show how G_D and w_{pl} act together to determine crack resistance [85]. While G_D contributes directly and has a role in determining the width of the plastic zone size, w_{pl} has a greater contribution to the fracture resistance value.

Chapter 7

Correlation of Plane Stress Fracture with Uniaxial Tensile Properties

During the analysis of the Reversed Charpy test, it was seen that the ligament section resists separation by drawing (as can be seen in Fig. 6.4). This observation was the initial motive for pursuing this study with tensile testing, and for seeking a possible relationship between Reversed Charpy and tensile test results.

In this chapter, large strain deformation is studied by referring to the existing information in the literature, from which a suitable molecular model is chosen expressing the tensile behaviour. Following previous modelling studies [61, 80, 86, 87] of the loss of drawing stability point (here characterised as adiabatic drawing stability, β_c), the results are then found to be related to the Reversed Charpy test results. In other words, the plane stress fracture resistance parameter is found to be correlated to drawing stability loss caused by adiabatic heating.

Although other studies [80, 86] have been made on the loss of drawing stability at high rates, this study differs from them in focusing specifically on the relationship between plane stress fracture resistance (w_{pl}) and β_c. Here the main finding is that w_{pl} can be related to the tensile properties. Thus it can be explained in terms of

structural parameters such as yield stress and hardening, and can be used to guide resin development.

This chapter also includes a literature review on the deformation mechanisms as well as the molecular models, aiming to give a detailed background that would enable interpreting the observed results.

7.1 Uniaxial Tensile Testing

With the application of an external force, F, a specimen responds with a change in dimensions: an increase in length and a decrease in area. The nominal, or engineering stress is defined as:-

$$\sigma_e = \frac{F}{A_0} \tag{7.1}$$

and the engineering strain is defined as:-

$$\epsilon = \frac{l - l_0}{l_0} \tag{7.2}$$

A more general and geometry-independent definition of the material stress is true stress which takes instantaneous cross section area, A, into account,

$$\sigma_t = \frac{F}{A} \tag{7.3}$$

Then, true strain is defined as the sum of the all the instantaneous engineering strains,

$$\epsilon_t = \int \delta\epsilon = \int_{l_0}^{l_f} \frac{\delta l}{l} = ln\frac{l_f}{l_0} = ln\lambda \tag{7.4}$$

where l_f is the final length when the loading process is terminated and λ is the specimen's axial extension ratio.

Tensile modulus can be calculated from the initial slope of the stress-strain curves by,

$$E = \lim_{\sigma \to 0} \frac{\delta\sigma}{\delta\epsilon} \tag{7.5}$$

In this work it will be assumed that plastic extension takes place at constant volume. Pursuing that, for rectangular specimens the cross-sectional area A can be used to generate continuous axial strain data as:

$$\lambda = A/A_0 \tag{7.6}$$

True stress is then related to the engineering stress by the following equations,

$$Al = A_0 l_0 \tag{7.7}$$

$$\sigma_t = \frac{F}{A} = \frac{Fl}{A_0 l_0} = \sigma_E(1+\epsilon) \tag{7.8}$$

The measurement of the true stress-strain behaviour aiming to describe tensile deformation of a material in a geometry independent manner has been developed over the years. The key factor for correct measurements is to ensure that the specimen responds in a uniform way during deformation, or that a sufficiently small volume of material can be identified and assumed to be representative to base the calculations on. The first results for polymers were published by Vincent [88] and by Meinel and Peterlin [89] for high density polyethylene. Later, the accuracy of the work was improved with the introduction of the waisted hourglass test piece, which eliminates necking, by G'Sell and Jonas [90] and Hope, Ward and Gibson [91]. Hiss and Strobl [92] developed a video camera system, recording successive images of the test specimen, which enables to analyse the increasing strain in real time at the narrowest part of the specimen. Using this technique, they have published data for a series of polyethylenes.

On the modeling side, it was recognised that two components are necessary for modeling large polymer deformations: an elastic model for the network of chains

and a viscous or plastic mechanism for which the stress depends on the rate of strain [93]. Haward and Thackray [94] used this approach in their one dimensional theory. Several research groups have elaborated the Haward-Thackray (HT) model into fully 3D models by using a variety of network and plasticity models [93, 95, 96, 97, 98, 99, 100]. By correlating multiaxial deformation using advanced variants of the HT model, most of these studies are restricted to amorphous polymers in terms of application.

Hillmansen *et al.* [101] developed HT model based on the microstructure of materials. This has been used as the main idea of this study and will be investigated further in detail in the following sections. Later, Ritchie [102] examined Hillmansen's [101] work and developed it by using energy kinetic equations in the calculation of strain rate giving the dependence of the stress-strain characteristics of HDPE on microstructural parameters.

All these studies are aiming to be able to explain stress-strain behaviour in terms of material structure, so that the materials can be developed to have specific kinds of stress-strain behaviour.

7.2 Tensile Test Curve

Figure 7.1 is a typical nominal tensile stress-strain curve for a standard *dog-bone* specimen of a ductile polymer, where the y-axis is the nominal stress (σ_e) obtained by dividing load by original cross-sectional area and x-axis is the extension. The *initial* part of the curve exhibits a linear (Hookean) region which is used to determine the Tensile Modulus of the material. The curve then becomes convex and reaches a maximum. The *peak point*, which is defined as yield stress point for polymers, is where the necking starts to occur. For the amorphous region, this yield point is associated with thermally activated overcoming of the Van Der Vaals interaction enthalpy between neighbouring macromolecules [103].

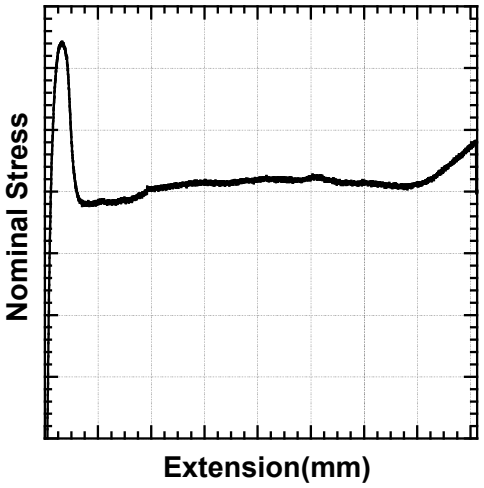


FIGURE 7.1: Typical Stress-Strain Curve for a ductile semicrystalline polymer

The tensile instability that follows yield results in the formation of neck. Following that, the *horizontal part* of the curve represents the stable drawing process at constant stress conditions. The stability of the neck depends on the material's strain hardening characteristics: it is the sign of a yielded material being strong enough to drag fresh material through the neck shoulders towards each end of the specimen. After the drawing process, the *final stage* in the curve is the increase in the load due to the shape of the specimen until the specimen fractures.

The structure and morphology of the material determines its mechanical behavior. The variety in the microscopic structure and morphology influences the deformation mechanism of the materials, which will be analysed in detail in the following sections.

7.3 Considère's Construction

This method can be simply used for the interpretation of yield and flow mechanisms by determining whether a polymer will neck, neck and cold draw, or deform homogeneously. Vincent [104] was the first person to apply Considère's construction method to solid polymers for the determination of the stability of drawing based on true stress-strain curves. The application of the method is simply based

on the tangent lines drawn to a true stress-strain curve from $e = -1$ and $\lambda = 0$ point, as seen in Fig. 7.2.

Following the definitions given in Section 7.1, engineering stress is given by,

$$\sigma_e = \frac{F}{A_0} = \frac{\epsilon}{1+\epsilon} = \frac{\sigma_t}{\lambda} \tag{7.9}$$

According to this, a line drawn from the $\lambda = 0$ point as a tangent to the true stress-strain curve has a slope of σ/λ giving the applied tension at that point which is the conventional yield stress.

Since for a sample under uniaxial tension the yield point is the maximum, where there is an observed drop in the nominal stress, the derivative is equal to zero by mathematical definitions and is given by,

$$\frac{d\sigma_e}{d\lambda} = 0 \tag{7.10}$$

The tangent that can be calculated from the slope is effectively the derivative of Eq. 7.9,

$$\frac{d\sigma_e}{d\lambda} = \frac{1}{\lambda}\frac{d\sigma_t}{d\lambda} - \frac{\sigma_t}{\lambda^2} \tag{7.11}$$

and combining Eq. 7.10 and Eq. 7.11 leads to,

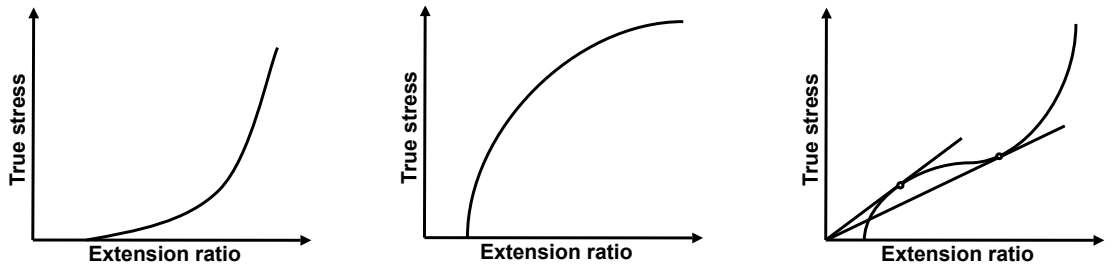
$$\frac{d\sigma_t}{d\lambda} = \frac{\sigma_t}{\lambda} \tag{7.12}$$

which is the basis of Considère's construction method.

Combining this mathematical equation with the application of the tangent line on the curve, three types of behaviour can be seen as shown in Fig. 7.2.

1. As demonstrated in Fig. 7.2(a), in the case of a convex curve, if

$$\frac{d\sigma_t}{d\lambda} > \frac{\sigma_t}{\lambda} \tag{7.13}$$



(a) No tangent (b) One tangent (c) Two tangents

FIGURE 7.2: Considère's Construction Curves

then, no necking occurs; the material extends uniformly until failure. In this type of curves, a tangent line from λ=0 cannot be drawn.

2. As demonstrated in Fig. 7.2(b), if Eq. 7.12 is valid at one point on the curve, then the material will neck and fail.

3. As demonstrated in Fig. 7.2(c), if Eq. 7.12 is valid at two points, then necking will be followed by cold drawing. At the second point (point B in Fig 7.2), the neck stabilizes, and begins to extend by drawing fresh material from the tapering regions on either side until the whole parallel section of the specimen is yielded. It can be concluded that two tangent lines are required for the observation of both necking and cold drawing phenomena.

7.4 Eyring's Model

Eyring model represents one of the approaches proposed to explain yielding behaviour in polymers [105]. Since this approach will be used for extrapolating data, a brief introduction is given in this section.

This model aims to relate the temperature and strain rate effects on flow stress by using a molecular movement point of view. The idea is based on the fact that an atom requires certain amount of energy to move from one position to another in the solid. Eyring [105] introduced the idea that barrier height and the energy needed to pass this barrier can be modified by shear stress, σ_s.

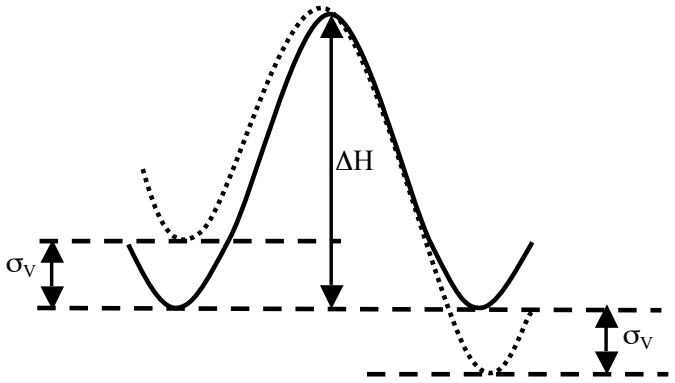


FIGURE 7.3: Eyring model of solid Flow

In this idea, it is assumed that plastic deformation is dominated by shear stress. With further assumptions that the imposed strain rate is proportional to the net rate when the forward and reverse jump rates are combined and that the dominant shear stress in a tensile test is considered to be the maximum shear stress, the final form of the equation can be expressed as,

$$\dot{\epsilon}_y = \dot{\epsilon}_0 \exp\left(-\frac{\Delta H}{RT}\right) \exp\left(\frac{\sigma_y V^*}{2RT}\right) \tag{7.14}$$

where $\dot{\epsilon}_0$ is the reference strain rate, V^* is the activation volume indicating the size of molecular segments that are mobile during the yield process, ΔH is the activation enthalpy required to transport these segments across a potential barrier resisting molecular motion, R is the molar gas constant, and T is the absolute temperature. If Eq. 7.14 is rearranged to determine σ_y at varying strain rates,

$$\left(\frac{\sigma_y}{T}\right) = \left(\frac{2}{V^*}\right)\left[\left(-\frac{\Delta H}{T}\right) + 2.303R\log\left(\frac{\dot{\epsilon}_y}{\dot{\epsilon}_0}\right)\right] \tag{7.15}$$

is obtained.

Data measured over a range of strain rates at constant temperature can be used to extract the Eyring rate constants and then make extrapolations outside the range of the measurements.

7.5 Haward-Thackray Model

In order to understand and extrapolate experimental data for large strain extension, it is necessary to fit a material model that can represent the materials' behaviour. Haward and Thackray [94] introduced a model which analyses true stress-true strain behaviour by dividing the process into several components (Fig. 7.4).

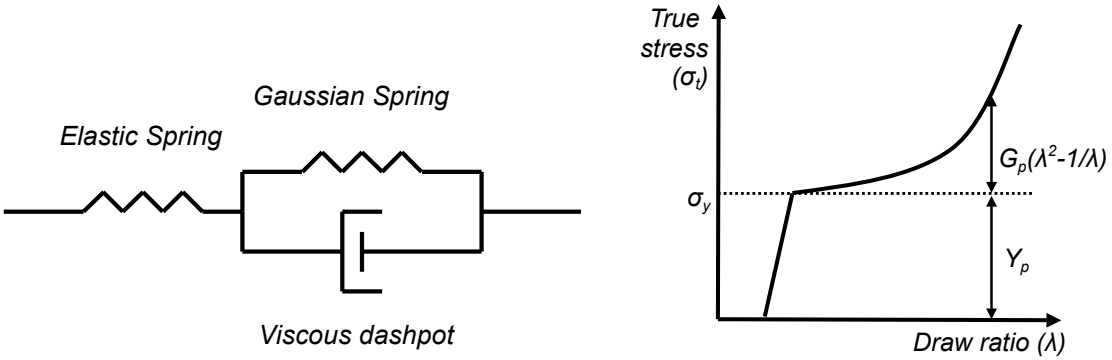


FIGURE 7.4: Haward-Thackray Spring-Dashpot Model, ($\sigma_t = \sigma_y + G_p(\lambda^2 - 1/\lambda)$)

Going up the stress-strain curve step by step: for the first part of the curve, Hookean deformation is assumed for the amorphous section deformation, which can be represented by linear elastic spring, where the process is considered as time independent, and defined by $E = stress/strain$.

After the yield point, deformation resistance is described by a viscous dashpot, representing temperature and rate-sensitive flow, in parallel with a rubber-elastic spring representing post yield deformation. The spring parallel to viscous element means that the model will eventually return to its initial stage whenever load is removed [94].

The applicability of the rubber elasticity theory for the strain hardening process was confirmed by Mills *et al.* [106] who correlated the deformation of an entangled network with rubber elasticity theory. For this part of the model, different representations can be used. Initially the Langevin Equations were suggested by Haward-Thackray [94], where it is assumed that the polymer chain is extended between permanent points of entanglement until it is nearly straight giving a limiting

ultimate elongation [107]. The solution of this equation requires the determination of two constants which require application of complicated mathematics although Cohen [108] found a Padé approximation as simple as the Gaussian equation. Boyce, Parks and Argon [95] demonstrated the applicability of the model to the experimental results of Hope *et al.* [91]. Although the predictions of this model are found to fit the experimental data satisfactorily, the difficulties and complications in finding the additional constants, such as the number of flexible links between the effective crosslinks, limit the usage of this approach.

One other approach that was suggested later by Argon [109] is to use the Gaussian approximation, in which the polymer coil does not approach a fully stretched condition. When conventional Gaussian chain statistics are employed to represent the spring, plastic deformation of a Haward-Thackray material is represented by the equation,

$$\sigma_t = \sigma_y + G_p(\lambda^2 - 1/\lambda) \tag{7.16}$$

where G_p is the Gaussian strain hardening modulus. Thus, G_p can be determined from the slope of the σ_y versus $(\lambda^2 - 1/\lambda)$ curve, which is linear in many cases. A number of crystalline polymers obey this relation at temperatures significantly below their melting point (T_m) [87, 101, 107, 110, 111].

Because the Haward-Thackray model has no elastic modulus, *i.e.* it does not extend before the yield stress is reached, the first part of Fig. 7.2 for such a material is a vertical line, and there is a corner at $\lambda = 1$. At constant nominal stress, Eq. 7.12 for such a material gives

$$G_p = \frac{\sigma_y}{\lambda^2 + 2/\lambda} \tag{7.17}$$

The first Considère condition of Eq. 7.12 is then satisfied automatically there if

$$\frac{\sigma_y}{G_p} > 3 \tag{7.18}$$

If there is a second Considère condition, it will correspond to stable drawing at an extension ratio (*natural draw ratio*) λ_d, derived from Eq. 7.17 as,

$$\lambda_d^2 + 2/\lambda_d = \frac{\sigma_y}{G_p} \tag{7.19}$$

relating G_p to σ_y and λ_d. It has been shown that for polyethylene, G_p is determined by an Eyring process [101] so that this, too, can be extrapolated to different rates and temperatures.

Cross and Haward [111] demonstrated the application of Gaussian model to quenched PVC while G'Sell [90] applied the model to semi-crystalline polymers. The validity of the model has been confirmed for a wide range of thermoplastics [107] by the application of the model to previously published experimental data in the field. G'Sell *et al.* [110], Haward *et al.* [111] and later Haward [107], [112] and Hillmansen *et al.* [101] showed that the model's prediction for polyethylenes is satisfactory.

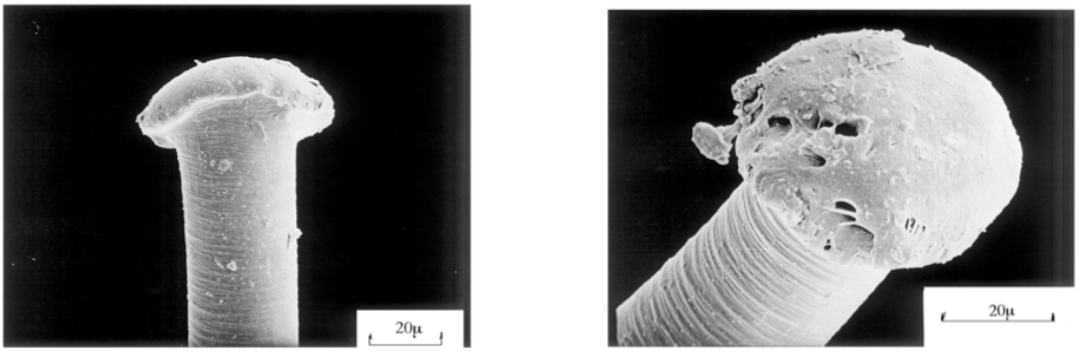
Using the previous work of Crawford and Kolsky [113], who showed that the drawing of polyethylene performing molecular reorientation does not qualitatively follow rubber elasticity theory, Ritchie [102] questioned the application of a rubber elasticity model for deformation of polyethylene below its melt temperature. The rate and temperature factors that are not taken correctly into account in the theory are known to play an important role in the deformation process. To overcome these problems, he developed a model indicating the dependence of stress strain behavior on microstructural parameters. However some further modifications are needed since the model does not provide a sufficiently close match with the experimental data.

In the present work, we will use the Gaussian approximation for the development of our model, based on the easiness and satisfactory results obtained from its application.

7.6 Thermomechanical Effects

Energy dissipation during deformation is an important factor since the mechanical properties of thermoplastics depend strongly on temperature. Deformations, accompanied by an increase in temperature, effectively result in a decrease in the materials' energy absorbing capacity [114].

There have been various studies in the area trying to observe thermomechanical heating and to measure the amount of energy dissipation as well as the amount of temperature change. Hearle *et al.* [6] and Brough *et al.* [115], studying the effect of strain rates, observed mushroom shaped deformation on the separation points of the PET fibrils (Fig. 7.5), and attributed these to the localized thermomechanical heating of the material.



(a) (b)

FIGURE 7.5: Mushroom ends from a PET fibre broken at high strain rate [6]

Haward [114, 116], measured this temperature change using infrared thermovision and was able to calculate thermal properties.

Williams [117] considered the effect of thermomechanical softening on crack growth. He considered adiabatic softening as a result of fracture to increase fracture resistance. On the other hand, an adiabatic decohesion model was developed by Leevers [43, 45, 46], which considered adiabatic heating as the mechanism of fracture. As estimated before, following studies showed that the temperature increase during fracture can be quite large. Studies on polystyrene showed local high temperature increases during fast crack propagation, reported as 327 °C and above

by Dickensom *et al.* [118] and for glassy polymers as 127 °C by Fuller *et al.* [119]. Recent studies on bulk deformation in polyethylenes have been done by Farruggio [120] and Davis [61], who measured temperature increases around 40-50 °C at high cross-head speeds of 0.017 m/s.

These observations can be expressed in terms of equations by considering the flow of material from the neck shoulders having the basic energy balance:

$$\Delta W = \Delta Q + \Delta U \tag{7.20}$$

where ΔW is an increment in plastic work, ΔQ is the heat generated during this increment and ΔU is the change in the internal energy; heat generation can be related to the work done by,

$$\Delta Q = \beta \Delta W \tag{7.21}$$

where β is the dimensionless factor specifying the proportion of work converted into heat. At *slow rates*, the heat generation is less then the heat loss by conduction resulting in isothermal conditions. However, above strain rates of $3{\times}10^{-3}\mathrm{s}^{-1}$ adiabatic conditions are expected since the heat generation overcomes heat loss resulting in an increase in the temperature of the section, so the thermal effects start playing an important role in the drawing process [87].

To calculate these effects quantitatively, conversion of isothermal conditions to adiabatic conditions is represented by introducing a heating factor to the equation which is given by,

$$\Delta T = \int \beta \frac{\sigma}{\rho C_p \lambda} \delta\lambda \tag{7.22}$$

where β is the dimensionless factor specifying the proportion of work converted into heat and ΔT is the amount of temperature change, with $\beta = 0$ condition representing isothermal systems and $\beta = 1$ representing adiabatic systems.

Hillmansen *et al.* [87] working on the adiabatic heating in polyethylene, referred to previously published true stress-strain data by Strobl *et al.* [121] and represented them using the Haward-Thackray model with the Gaussian approximation. Eyring extrapolations were applied to the Gaussian parameters to take the temperature

and strain rate effects into account. Without doing any further experiments, just to see the effect of adiabatic heating, Eq. 7.22 was applied to modify the isothermal experimental curves, and it was found that the initial temperature was important in determining the adiabatic heating process. It was also predicted that the increase in temperature as a result of adiabatic heating would be much greater when the initial temperature was lower; which had also been shown by Ritchie, Davis and Leevers [68].

Haward [112] also studied adiabatic heating quantitatively, working on previously published stress-strain curves [121]. Following the same ideas as Hillmansen [87], he focused on the effect of natural draw ratio on the temperature change. By using published specific heat capacity versus temperature data [122] at constant nominal stress, he obtained the draw ratio-temperature relationship by making use of Eq. 7.22. As a result of this study, he concluded that the natural draw ratio has significant importance on the amount of temperature change (and effectively on the adiabatic heating) and that the temperature increases as the draw ratio increases.

7.7 Relation between the Reversed Charpy and the Tensile Test

During Reversed Charpy testing, it was seen that the ligament resists separation by drawing (Fig. 6.4). This observation was the motive for seeking a possible relationship between Reversed Charpy and tensile test results. Further studies on the nature of these two tests revealed some more similarities between them, which can be summarised as follows:

- In both tests, the section subject to load is under uniaxial tensile stress.
- Both the gauge length of a tensile specimen and the ligament of a Reversed Charpy specimen neck at yield.

- In Reversed Charpy test, the constriction formed at the centre of the ligament appears to propagate outwards towards the site of initial shear band formation in a process similar to cold-drawing.

- Although the strain rates are different, the general shapes of the load-displacement curves are similar as can be seen in Fig. 7.6. The main difference seen in the load-displacement traces is that in the case of a tensile test, necking stabilises; whereas in a Reversed Charpy test, the ligament section continues to neck down until it separates. The presence of the sharp notch in the Reversed Charpy test causes localized deformation of the initial neck which, when combined with the need for the neck to propagate into a thicker section, reduces ligament elongation [61].

- The yield stress values that are determined from each test are similar as can be seen in Fig. 7.7.

In this study, the results from both tests are compared and reported in the following sections.

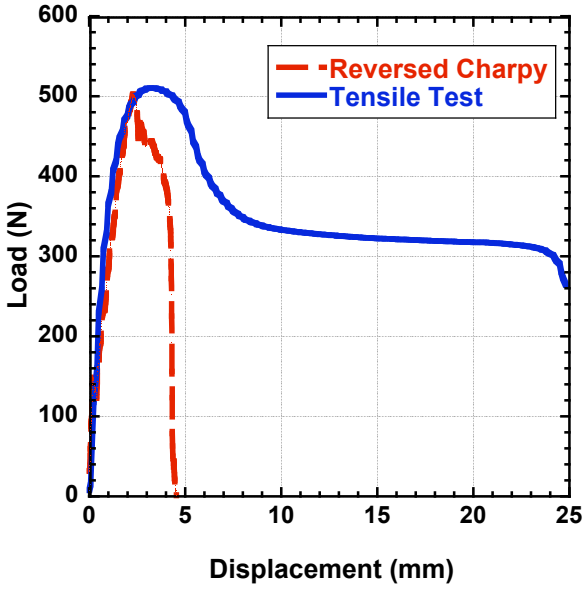


FIGURE 7.6: Load-Displacement Trace Comparison between Reversed Charpy and Tensile Test, 20°C, PE-8

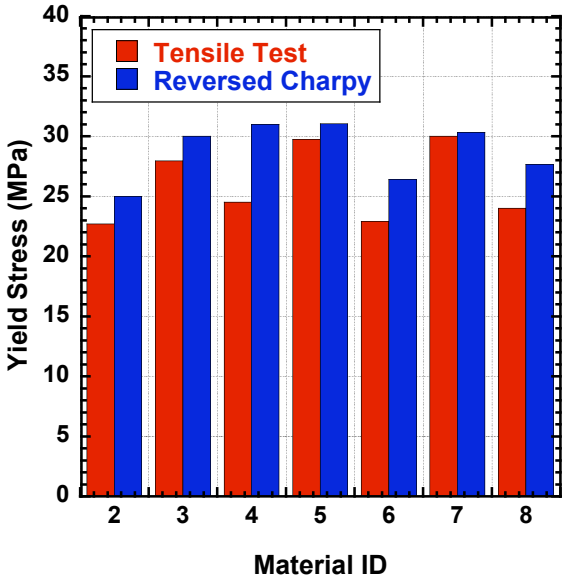


FIGURE 7.7: Yield stress Comparison between Reversed Charpy and Tensile Test (6 mm/min, $(4 \times 10^{-3} s^{-1})$), 20°C

7.8 Deformation Mechanisms

To improve the understanding of the effect of tensile stretching on the material structure, one should take a brief look into the deformation mechanisms of crystalline polymers in general.

As mentioned before, semi-crystalline polymers usually have spherulitic structure consisting of chain-folded ribbons, or lamellae that radiate outward from a centre. Separating these lamellae are areas of amorphous material; connecting them are the tie chains that pass through these amorphous regions (Fig. 2.9).

Elastic deformation mechanism involves rotation of strong covalent bonds in chain molecules where slight displacement of adjacent molecules can take place despite secondary Van der Waals bonds.

In the case of *plastic deformation*, lamellar interactions in addition to the amorphous regions respond to the applied tensile load. At the beginning of plastic deformation, deformation of the amorphous component happens by means of sliding (interlamellar shear) and rarely by separation of lamellae (interlamellar separation) or lamella-stack rotation. Due to the physical constraints, deformation of

the amorphous phase is limited, and for further deformation crystal rearrangement is necessary [123].

The continuous strain increase results in the reaction of crystal sections mainly by slipping (sliding of layers of repeat units through the motion of dislocations) and dislocation motions and occasionally by twinning or martensitic transformations. As the strain is increased, spherulites become elongated parallel to the stretching direction, they break and a fiberlike morphology is obtained.

The nature of the spherulite deformation is known to be non-uniform and is classified into homogeneous and inhomogeneous types. In the case of homogeneous, all parts of a spherulite extend simultaneously, and the spherulite is transformed into an ellipsoid. In the case of inhomogeneous deformation, both interlamellar and intralamellar mechanisms are observed where the deformation occurs in equatorial regions differently.

Tensile deformation mechanisms have been studied by different groups making use of various experimental systems. Even the reorganization of the molecules issue has not been agreed on between the choices of crystals themselves rotating [124, 125] or the polymer melting under stress and then reorganising [123, 126]. Many approaches have been suggested for the full explanation of this system. Most often, it is attributed to the generation and propagation of screw dislocations (dislocation theory/ crystal plasticity approach) [124, 125], or to melting-recrystallization [126].

Being the followers of the former approach, Peterson [124] and Young [125] link the changes in the global texture to rotations, slips, and rearrangements of the crystalline lamella and make use of the thermal activation of screw dislocations with Burgers vector parallel to the chain direction. The relations between shear stress and crystalline thickness are given in terms of Gibb's free energy that is required to form a screw dislocation of a Burgers vector. This model enables the calculation of the dependence of shear yield stress on crystallite thickness and on the deformation temperature.

Peterlin [17], introducing the term *microfibrils* as representing the main structural element, explains the phenomena of deformation by linking it to the cracking between adjacent lamellae which transform into microfibrils by the effect of micro-necks. Following this, Reed *et al.* [7] studied the spherulite deformation by etching techniques and agreed on Peterlin's conclusions. Figure 7.8 shows a sequence of sections taken longitudinally through the neck of cold-drawn polyethylene and indicates the development of columnar structure.

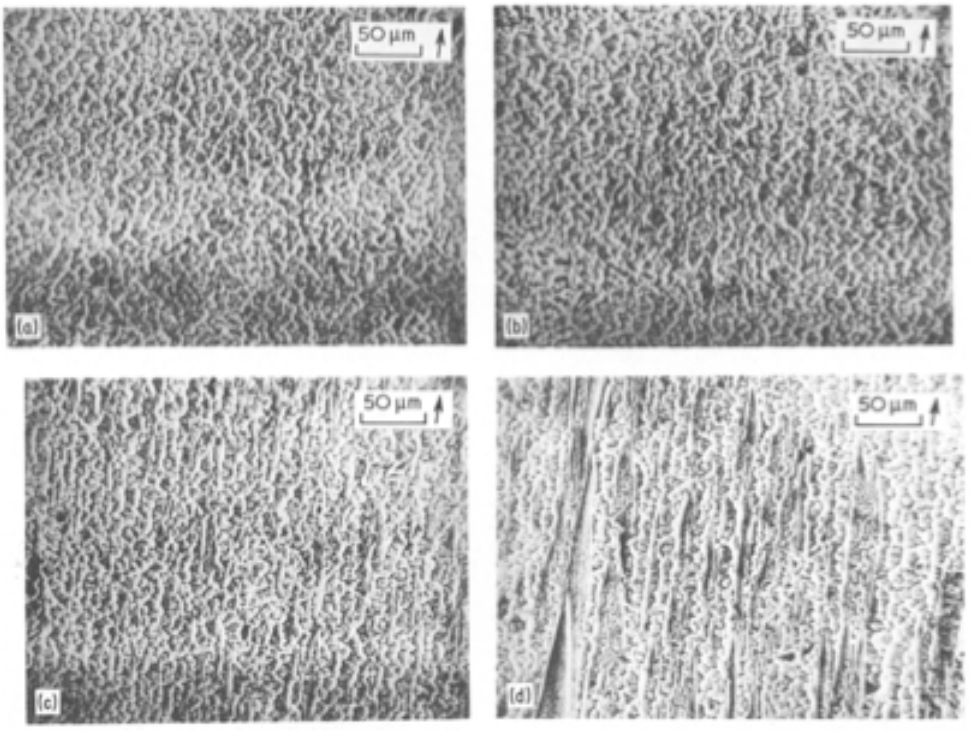


FIGURE 7.8: (a) Spherulitic structure at entry to the neck (b) One-third of the way into the neck (c) Two-thirds of the neck (d) Fully developed drawn texture at the base of the neck [7]

Following this, Bowden and Raha [127] proposed that during drawing, the amorphous region is deformed, and the crystalline regions act as entanglements for the amorphous network [106] while the material is re-arranged in terms of atoms moving to new positions [128]. Studies continued to investigate the effects of lamellar thickness and degree of crystallinity on yielding [102, 129].

Lin and Argon [3] restricted their studies only to the changes within the crystallite

interior, based on the fact that yield stress is highly affected by changes in crystallinity. They concluded that the slippage of crystallographic planes dominated over the complete deformation range.

Although the crystal plasticity approach manages to predict the correct order of yield stress, it fails to explain the observed dependence of the crystalline long period on the temperature of deformation [130, 131]. During their studies, Peacock [131] could not find a correlation between the experimental results and the model predictions in terms of temperature dependence.

As an extension of the dislocation theory, the Eyring transition state theory [105], involves the application of the Eyring equation to the thermally activated processes. In this approach, temperature and strain rate effects are taken into account using a molecular point of view, while it is assumed that plastic deformation is dominated by shear stress.

The alternative approach, melting-recrystallization approach, introduced by Flory and Yoon [126], proposes that crystals melt and recrystallize along the drawing direction to build up the fibrillar structure.

Strobl *et al.* [123] observed that in the case of high deformation, at a certain critical strain, the crystalline blocks lose stability due to the forces from the entangled amorphous phase. After this critical value at which crystalline blocks lose stability, they recrystallize in the drawing direction to form fibrils which might still include previous amorphous regions.

The melting-recrystallization approach fails to explain the development of preferred crystallographic orientation during deformation and phenomena like crystal phase change and twinning, which have been reported to occur in polymer crystals [130]. Also Kanig [132] carried out detailed electron microscopy studies on deformed PE, and could not find any evidence for the suggested transition from crystal lamellae to microfibrils but instead observed a network of fibers cross-linked by crystal blocks.

Although this project does not necessarily deal with the details of the microstructure during deformation, knowing the existence of these approaches makes it easier to interpret the results obtained from the experiments.

The effects of crystallinity, density and molecular weight on the yield stress and strain hardening modulus values are investigated in this study. The yield stress mechanism is related to the crystal content, while strain hardening is a property of the amorphous region where tie molecules are present. The results obtained are interpreted by referring to material structure, crystals, tie molecules and entanglements. From our observations, all structural parameters are found to have a significant role on the deformation behaviour together with the temperature and strain rate parameters. For the extrapolation of yield stress and strain hardening modulus to different strain rates and temperatures, Eyring theory is used. The details of these results will be discussed in Section 7.9.2.

7.9 Tensile Test Experiments

Having chosen the models representing the material (Haward-Thackray model with Gaussian rubber elasticity equations and Eyring state extrapolations), tensile tests were carried out to determine the two main parameters σ_y (from maximum load) and G_p (from λ_D). Aiming to satisfy isothermal conditions, tests are carried out at three *slow* rates (0.24 mm/min, 1.2 mm/min, 6 mm/min corresponding to strain rates of $1.6\times\ 10^{-4}s^{-1}$, $8\times\ 10^{-4}s^{-1}$ and $4\times\ 10^{-3}s^{-1}$ respectively), and at three constant temperatures (20°C, 40°C and 60°C). These experimental results are then extrapolated to high speeds representing adiabatic conditions.

7.9.1 Procedure and Analysis of Tensile Test

Rephrasing previous sections, stable drawing of necked material is predicted to become unstable under adiabatic conditions. The degree of adiabatic heating is

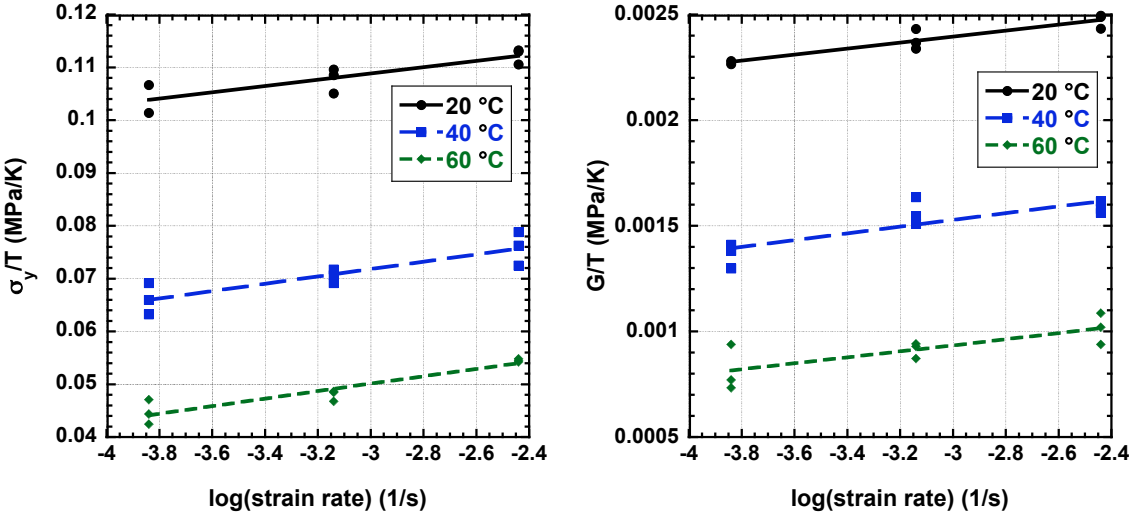
determined by the thermomechanical efficiency β. Since this is a very difficult parameter to measure, the approach used here is to test each material at low speed isothermal conditions, extrapolate the data to high speed adiabatic conditions using the Eyring process, and then use this extrapolated data to simulate adiabatic deformation at an estimated β value. Using a software program written by former researchers in the area [86], the stability of drawing is checked by a iterative process. For each case, stress-strain curves are integrated for a given value of β, work-to heat conversion ratio, and the Considère's condition is checked to see whether a 2nd tangent exists. The critical β at which this 2nd tangent no longer exists, *i.e.* at which the stable drawing is lost, is termed as the *adiabatic drawing stability*, β_c. Finally, materials are rated according to their β_c values. As mentioned before, this study specifically focuses on the relationship between plane stress fracture resistance (w_{pl}) and β_c, which effectively enables w_{pl} to be expressed in terms of material properties such as yield stress and natural draw ratio.

The physical meaning of this whole idea is that when a polymer is deformed under adiabatic conditions, the extension would be limited due to premature thermal rupture [86]. A polymer that is capable of having a second Considère tangent under all adiabatic conditions would be expected to form a stable neck. Although a value of $\beta > 1$ is physically unlikely, it indicates very high stability for stable drawing under adiabatic conditions $\beta \rightarrow 1$.

Tensile specimen dimensions are measured before and after the tests for the determination of natural draw ratio. These results are used for the calculation of HT model parameters which are extrapolated using Eyring curves. These Eyring curves are used for the determination of reference strain rate, activation volume and enthalpy values of both σ_y and G_p for each material which are then used to determine β_c.

Figure 7.9 shows typical examples of Eyring plots for σ_y and G_p respectively. The yield stress/temperature and G_p/temperature values decrease with increasing temperature and they show a positive trend with respect to the logarithm of the

strain rate. All the materials were tested at three different strain rates and at three different temperatures.



(a) Yield Stress

(b) Stress hardening Modulus

FIGURE 7.9: Eyring Plot: Yield Stress and Stress Hardening Modulus as a function of the logarithm of nominal strain rate (based on gauge length of 25 mm; 1.6× $10^{-4}s^{-1}$, 8× $10^{-4}s^{-1}$ and 4× $10^{-3}s^{-1}$) at three temperatures

Overall testing and analysis procedures are given below step by step.

Specimen preparation and initial testing:

1. *Plaque preparation:* Using a hot press as shown in Fig. 5.2, plaques of thickness 3 mm were moulded.

2. *Thermal processing:* In addition to 1.5 °C/min cooling rate achieved by hot press, via using thermal conditioning press, plaques were processed with cooling rates of 0.5 °C/min and 10 °C/min.

3. *Specimen preparation:* Specimens were machined from the plaques following the dimensions given in BS EN ISO 527-2:1996 (specimen type: 5B) [133] (as can be seen in Fig. 7.10).

4. *Measuring initial dimensions:* Width and thickness of the neck section was measured at 5 points to give an initial average cross-sectional area.

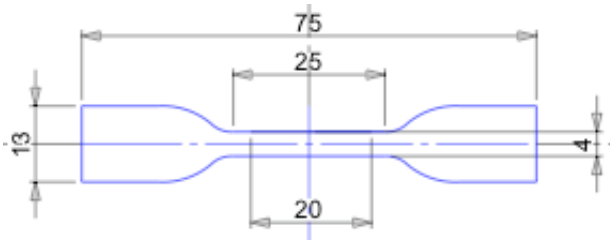


FIGURE 7.10: Tensile Specimen Geometry

5. *Tests were performed* at three rates (crosshead speeds: 0.24 mm/min, 1.2 mm/min and 6 mm/min; where nominal strain rates are $1.6\times\ 10^{-4}s^{-1}$, $8\times\ 10^{-4}s^{-1}$ and $4\times\ 10^{-3}s^{-1}$, based on gauge length of 25 mm), three temperatures (20°C, 40°C and 60°C), and with three repetitions in each condition.

6. *Load-displacement* traces were recorded by Instron.

7. *Maximum load* was extracted from the load-displacement traces and *final specimen dimensions* were measured for the calculation of extension ratio.

Data processing:

8. Knowing the maximum load and extension ratio, *Haward-Thackray Model* (Eq. 7.16) parameters, σ_y (via Eq. 7.1) and G_p (via Eq. 7.17, using the measured yield stress and the draw ratio at the neck based on the ratio of initial to final cross section area) were calculated. For both parameters, the temperature and strain rate effects are modelled by Eyring model, assuming that strain hardening modulus obeys the model as well as yield stress based on the previous studies in the area. [80]

9. *Eyring graphs* were plotted as given in Fig. 7.9. Having two variables ($1/T$ and $\log(\dot{\epsilon})$) affecting each parameter (G_p and σ_y), the multiple linear regression method was used to determine Eyring parameters ($\dot{\epsilon}_0$, V^* and ΔH).

   Multiple linear regression: For a two variable system, linear equations of the form,

$$F = Ax_1 + Bx_2 + C_e \tag{7.23}$$

can be used to express the relationships among the variables. Here F is the random variable whose values we want to predict in terms of given values of $x's$; and A, B and C the *multiple regression coefficients*, are the numerical constants that must be determined from observed experimental data.

Applying this method to the current case, rearranging Eyring equation Eq. 7.15 in a similar form,

$$\frac{\sigma_y}{T} = Ax_1 + Bx_2 + C_e \tag{7.24}$$

the terms will correspond to,

$$x_1 = \frac{1}{T} \quad \text{and} \quad x_2 = log(\dot{\epsilon})$$

$$A = \frac{2\Delta H}{V*} \quad \text{and} \quad B = \frac{2R2.303}{V*}$$

$$C = \frac{-2R2.303log(\dot{\epsilon}_0)}{V*}$$

Using Microsoft Excel for the analysis, ϵ_0, V^* and ΔH can be determined for each parameter.

To sum up, up to this stage we have one activation volume value V^*, one enthalpy value ΔH, and one reference strain rate $\dot{\epsilon}_0$ value for each Haward-Thackray parameter (σ_y and G_p), which are going to be used as input values to determine adiabatic drawing stability.

Stress-Strain Curve Simulation:

10. Initial β and strain rate ($\dot{\epsilon}$) values are given to the program. At each strain increment:

    - The change in temperature, ΔT, is calculated by Eq 7.22 for the given β condition.
    - According to the new temperature, HT parameters are updated by making use of simple linear extrapolation. New stress-strain curves are computed according to the new conditions.

- Considère's condition is checked to see whether 2nd tangent exists. (Fig. 7.11)

11. β is incremented and the previous procedure point (10) is repeated unless the 2nd tangent had vanished.

This critical β value serves as a qualitative, single point index for adiabatic neck stability. The materials are ranked according to this value.

Final Step: Checking the relation between Reversed Charpy and Tensile Tests

The adiabatic drawing stability β_c is compared with the plane stress fracture resistance value, w_{pl}, obtained from the Reversed Charpy test.

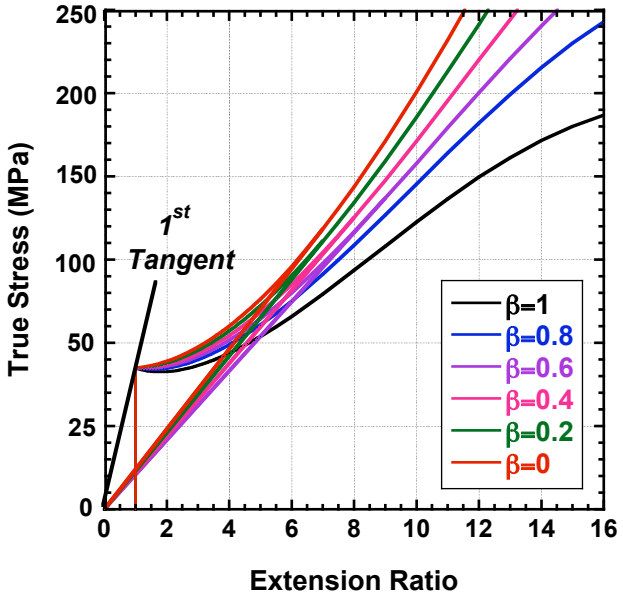
7.9.2 Experimental Results

Using the procedure described above, the effects of temperature, strain rate, crystallinity, density and molecular weight on the resulting parameters were investigated using C-Series, D-Series and MW series PE resins.

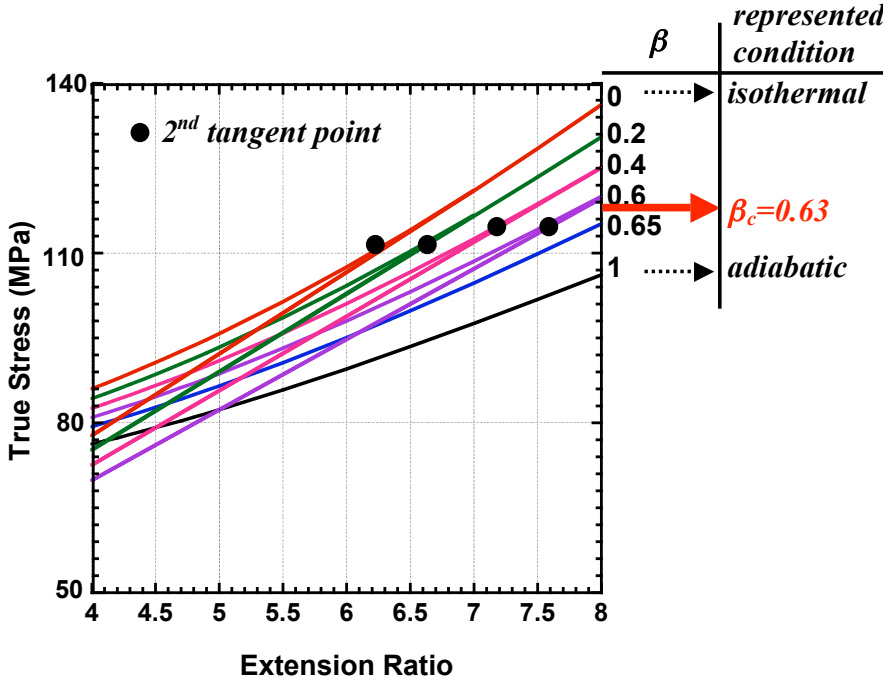
7.9.2.1 C-Series PE Resins

Load-displacement traces are first compared to see the effect of strain rate, temperature and crystallinity (for detailed material properties refer to Table 5.1).

Effect of Strain Rate can be seen in Fig. 7.12 which compares the different cross-head speeds recorded for the same material (PE-3, CR 1.5) at the same temperature (20°C). It can clearly be seen that, as the cross head speed increases, tensile drawing loses its stability and the specimen tends to fail at a lower displacement value *e.g.* see 250 and 500 mm/min.



(a)



(b)

FIGURE 7.11: Determination of adiabatic drawing stability β_c using Considère's condition, 20°C, 1 s^{-1}, PE-3 (CR0.5)

Effect of Temperature can be seen in Fig. 7.13 which compares the load-displacement traces recorded at 10 mm/min ($5.95 \times 10^{-3} s^{-1}$), for PE-3 (CR1.5) at different constant temperatures. It can be concluded that reducing the temperature shifts the curve upwards, showing higher yield and drawing stress values. Although the drawing process remains stable, elongation is observed to decrease

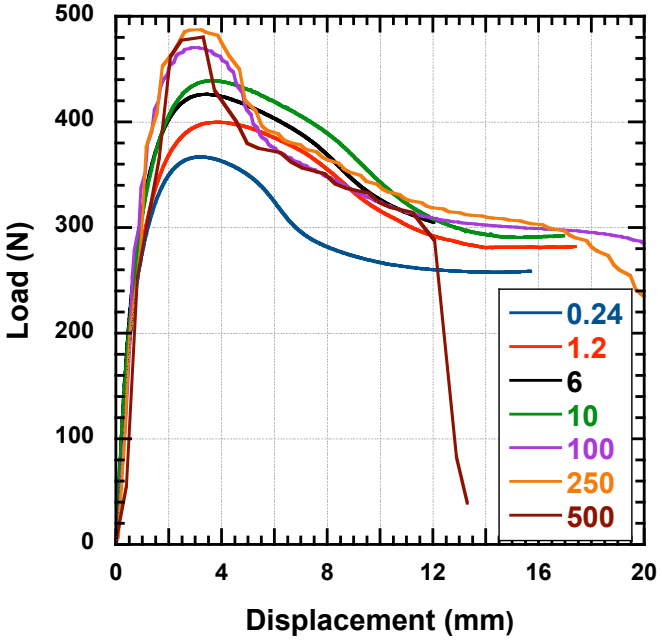


FIGURE 7.12: Effect of Cross-Head Speed (mm/min) on the Tensile Deformation at Constant Temperature, 20°C

with decreasing temperature.

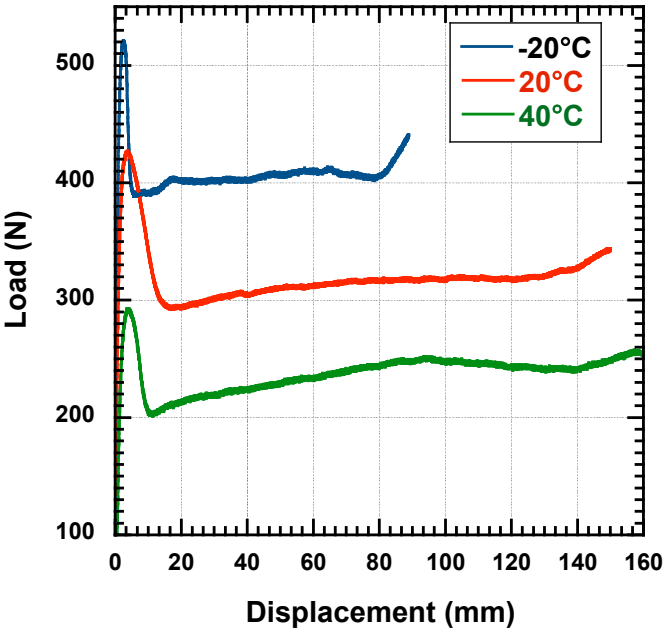


FIGURE 7.13: Effect of Temperature on the Tensile Deformation at a constant rate, 10 mm/min ($6.66 \times 10^{-3} s^{-1}$)

Effect of Crystallinity can be seen in Fig. 7.14 which compares the traces of PE-3 prepared using different cooling rates (CR 0.5, CR1.5, CR10) recorded at 6

mm/min ($4 \times 10^{-3}s^{-1}$) and 20°C. As can be seen, as the cooling rate decreases

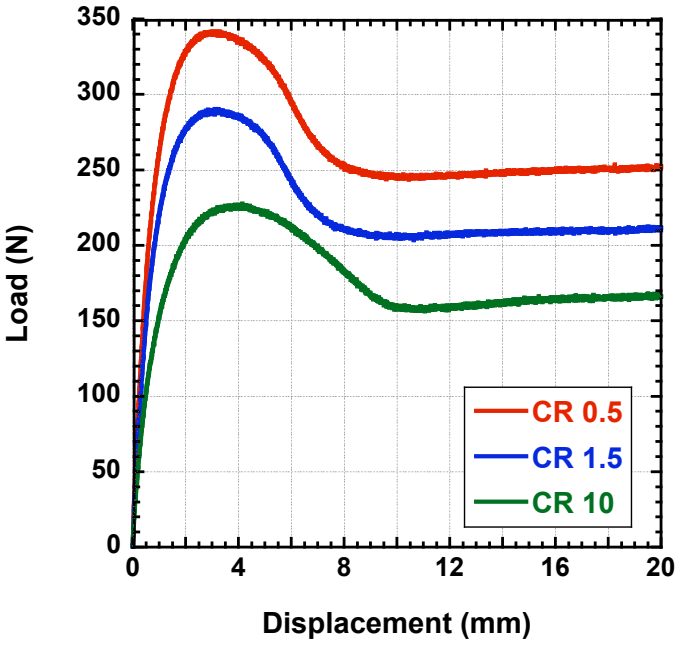
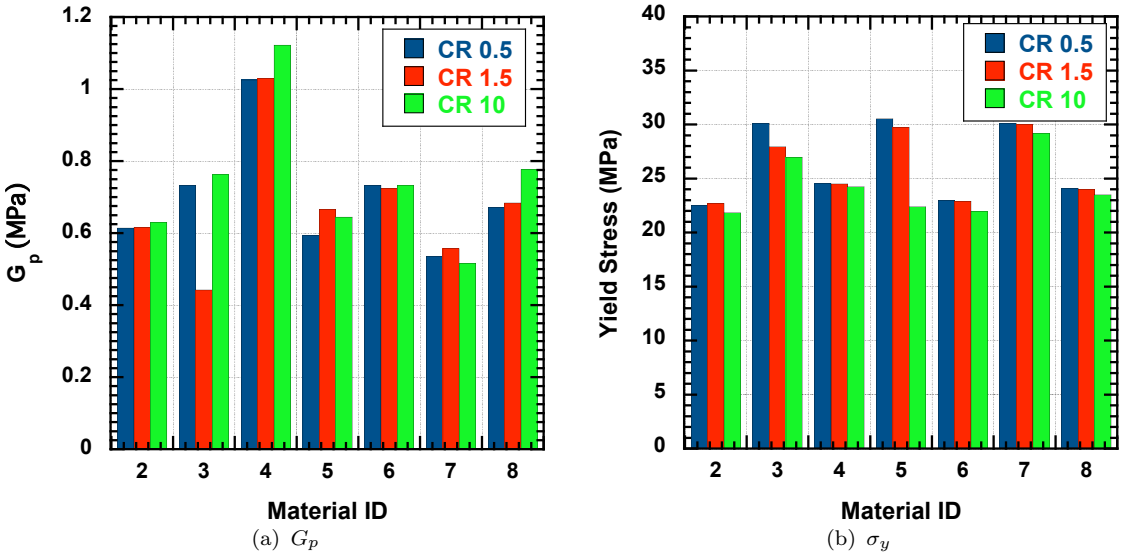


FIGURE 7.14: Effect of Cooling rate on the Tensile Deformation at a constant rate, 6 mm/min ($4 \times 10^{-3}s^{-1}$) and temperature 20°C

resulting in higher crystallinity, the tensile curve shifts upwards showing higher yield and drawing stresses. The effect can also be seen on the HT model parameters in Fig. 7.15 where the increasing cooling rate (*i.e.* decreasing crystallinity) results in a decrease in σ_y and an increase in G_p.

The yield stress, representing frictional forces during deformation [107], increases with crystallinity as previously observed [28, 74, 76, 83, 107, 123, 129, 134, 135, 136] many times. Initial studies of Mandelkern [28] and Williamson *et al.* [137] on the effect of crystallinity on the yield point showed that yield stress is related to crystallinity linearly and that this relationship does not depend on the crystallisation conditions [74]. Kennedy *et al.* [134], confirming the effect of crystallinity on different linear polyethylenes by experimental study, argued that the crystallinity also changes during yielding.

Developing the idea, Mandelkern *et al.* [76] found that at a constant crystallinity, the crystallisation condition is found to have an effect on the yield stress — contradicting the previous findings of Brown *et al.* [74]. They continued their research



(a) G_p (b) σ_y

FIGURE 7.15: Effect of cooling rate on strain hardening modulus and yield stress, based on data of 6mm/min ($4 \times 10^{-3} s^{-1}$), 20°C

by testing copolymers having different compositions and different polymerisation conditions [138]. As a result they concluded that in the glass transition temperature region, yield stress is not affected from the changes in crystallinity. However above that temperature, it plays an important role in draw ratio, tensile strength and deformation temperature parameters.

The studies of Ward *et al.* [129] showed that yield stress is related to the degree of crystallinity by a power law relationship and not by a linear relationship as suggested by others. They concluded that yield stress is mainly a factor of lamellar thickness following the idea in the dislocation theory approach.

On the other hand, the hardening modulus, G_p is mainly driven by the amorphous content, and entanglement density, and is a function of MW rather than crystallinity in reality [83, 134, 139, 140]. The observed results in Fig. 7.15(a) can be interpreted by the fact that the increased crystallinity results in a decrease in the number of tie molecules [27, 28, 74, 101], which effectively decreases the strain hardening property of the material, and makes it easy for the material to elongate leading to higher draw ratios.

Following the analysis procedure explained in the previous section, β_c values were calculated for each case and results are examined here in detail. The Eyring rate

constants for the HT model are given (only CR1.5 condition results are given for simplicity) in Table 7.1. As can be seen, the activation volume is much greater for the strain hardening parameter, while the enthalpy values are very close for both cases meaning that the energy requirement is the same for both processes. This result is very interesting in the sense that it might be indicating that there is only one process taking place overall.

HT	σ_y			G_p		
PE ID	**V*** $\mathbf{x10^{-3}}$ $(m^3/\mathbf{mol})$	**ΔH (kJ/mol)**	$\dot{\epsilon}_0$ $\mathbf{x10^{21}}$ (s^{-1})	**V*** $\mathbf{x10^{-3}}$ $(m^3/\mathbf{mol})$	**ΔH (kJ/mol)**	$\dot{\epsilon}_0$ $\mathbf{x10^{21}}$ (s^{-1})
PE-2	2.85	133.4	4.13	99.0	133.1	4.12
PE-3	2.86	183.9	4.05	92.1	168.3	4.07
PE-4	3.29	180.3	4.07	100.3	179.3	4.08
PE-5	2.15	153.0	4.09	98.6	174.3	4.06
PE-6	2.70	174.7	4.07	103.0	171.9	4.07
PE-7	2.99	236.6	3.99	52.3	184.1	4.02
PE-8	2.20	136.4	4.12	95.9	141.8	4.11

TABLE 7.1: Eyring rate constants for the HT model parameters

The effect of cooling rate on adiabatic drawing stability is shown in Fig. 7.16, where it is observed that for most of the cases, as the cooling rate decreases (*i.e.* as crystallinity increases), adiabatic drawing stability increases. It was initially expected that the crystallinity increase resulting in an increase in σ_y, would cause more adiabatic heating and decrease adiabatic drawing stability. Having obtained an opposing result, this might be explained by G_p acting as the dominating parameter. As crystallinity increases, strain hardening decreases (as a result draw ratio increases), due to the reduction in the number of tie molecules. So in this condition, drawing process is more stable being able to achieve higher draw ratios, meaning a higher β_c value.

Effect of assumed adiabatic strain rate and temperature on calculated adiabatic drawing stability is shown in Fig. 7.17 for the cooling rate condition

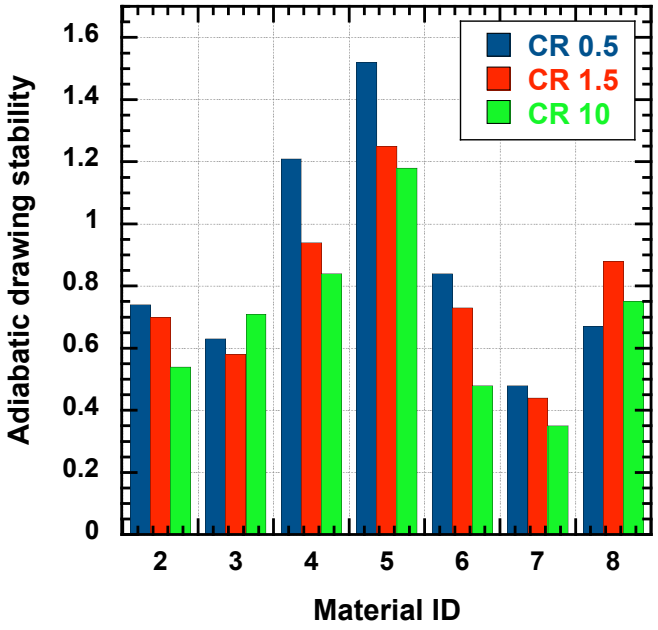
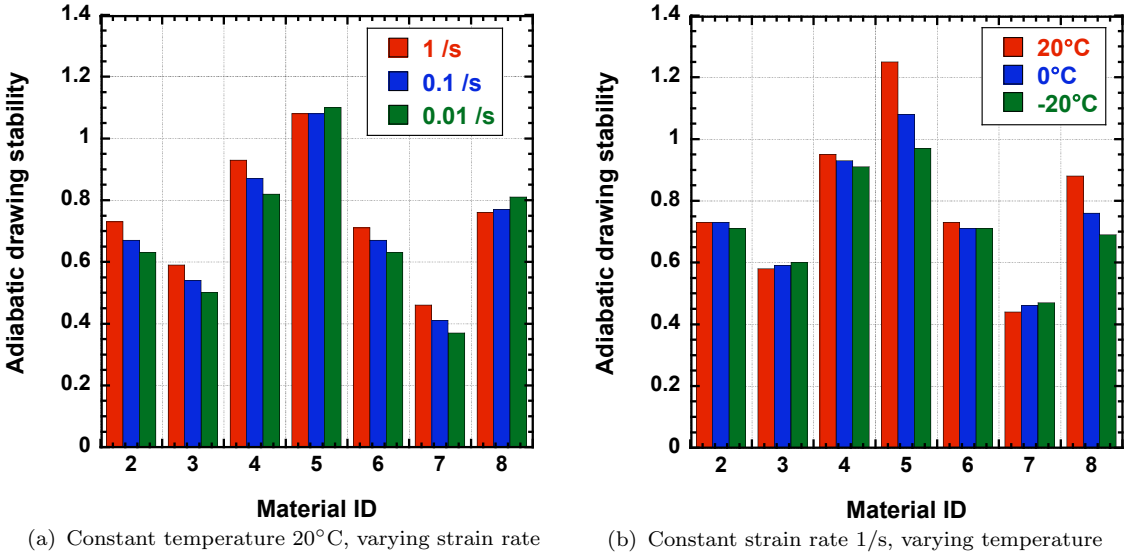


FIGURE 7.16: The effect of cooling rate on the adiabatic drawing stability

CR1.5. This analysis enables us to see the secondary effect of temperature and strain rate on β due to the changes in HT parameters.



(a) Constant temperature 20°C, varying strain rate

(b) Constant strain rate 1/s, varying temperature

FIGURE 7.17: Effect of assumed adiabatic strain rate and initial temperature on adiabatic drawing stability, CR1.5

Based on the results, it can be concluded that the increase of either strain rate or temperature results in β_c increase meaning a more stable system. As observed before by Haward [112] and Ritchie *et al.* [68], when the initial temperature is

reduced, the actual temperature change will be higher at the end of the process, so the adiabatic heating will be more active causing a more unstable system (lower β_c). For the case of strain rate, as the strain rate increases, the rate of heat generation decreases which might be the reason for the increasing adiabatic drawing stability [61].

Relationship between the tests: Coming to the main subject of interest, Reversed Charpy and tensile test parameters have been found to be related as shown in Fig. 7.18, supporting the initial ideas and assumptions. Each cooling rate condition shows reasonable linearity, but the sensitivity of w_{pl} to adiabatic drawing stability decreases with the increasing cooling rate.

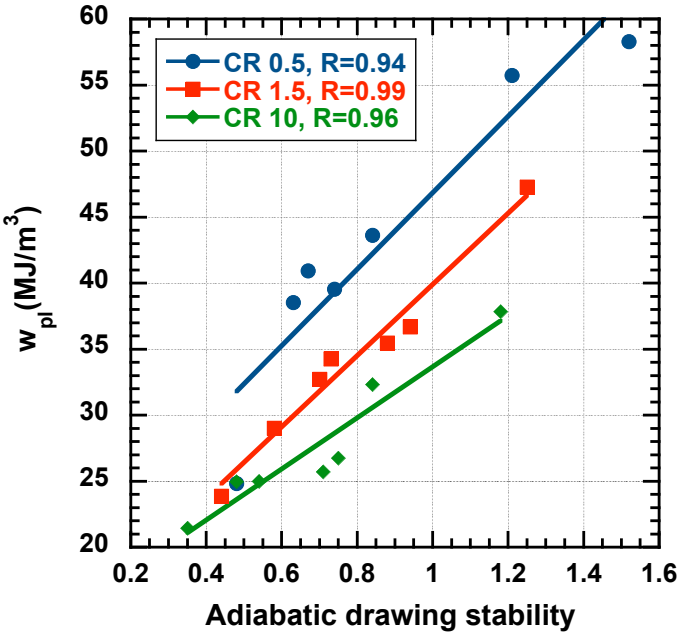


FIGURE 7.18: Correlation between adiabatic drawing stability and plane stress fracture resistance (reversed Charpy), at 0°C

Critical strain rate check: In order to check the validity of assumptions, more analysis were carried out by defining a *critical strain rate* at which the drawing stability is lost. As demonstrated in Fig. 7.19, it is determined from a neck propagation *vs.* crosshead speed plot by taking the speed just below that at the transition as the critical value. Plotting this value against β_c, which is another representation of the loss of drawing stability, the relationship obtained validates the findings as shown in Fig. 7.20.

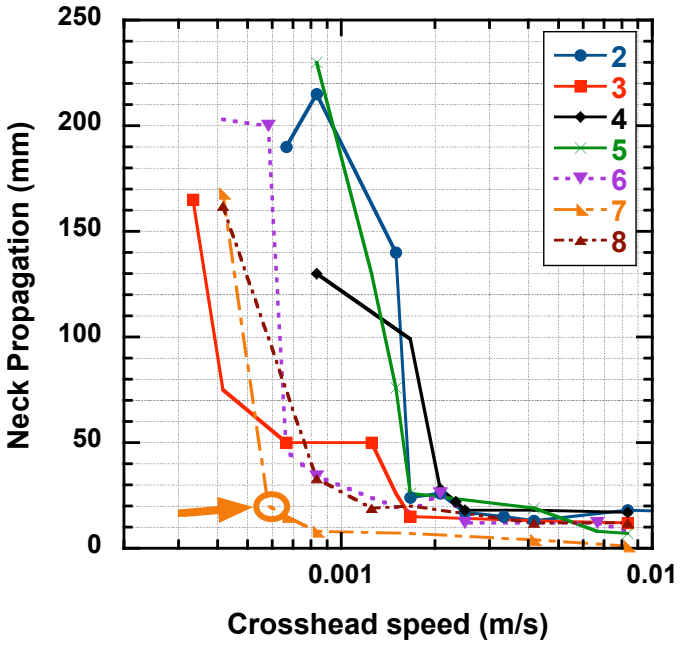


FIGURE 7.19: Critical strain rate determination method (CR1.5)

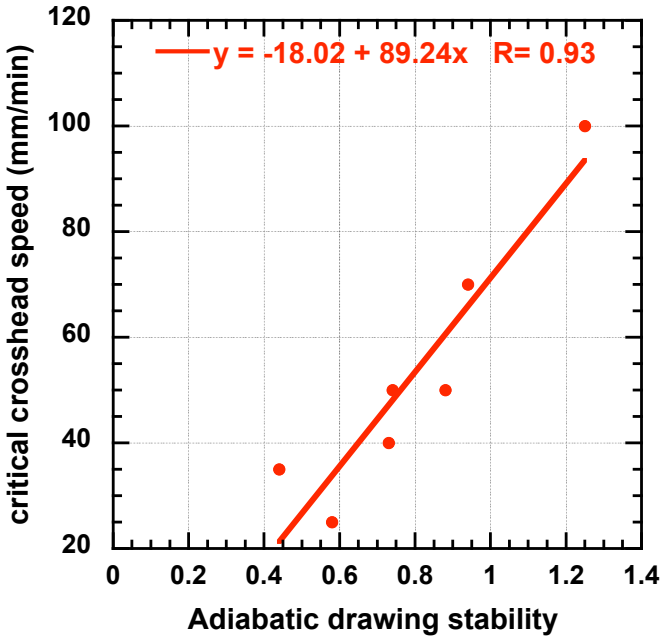


FIGURE 7.20: Relationship between critical strain rate and adiabatic drawing stability (CR1.5)

7.9.2.2 Effect of Density: D-Series PE Resins

Tensile testing carried out on D-Series PE resins prepared with CR 1.5 enabled us to see the effect of density on adiabatic drawing stability as well as on the stress-strain behaviour of the materials (for detailed material properties refer to Table 5.2). Generally, it can be concluded that as the density increases, load displacement traces shift upwards as shown in Fig. 7.21. This can be related to the same reasoning as the increasing crystallinity case. The overall effect of density on each HT model parameter is shown individually in Fig. 7.22, and these are also found to be inline with expectations.

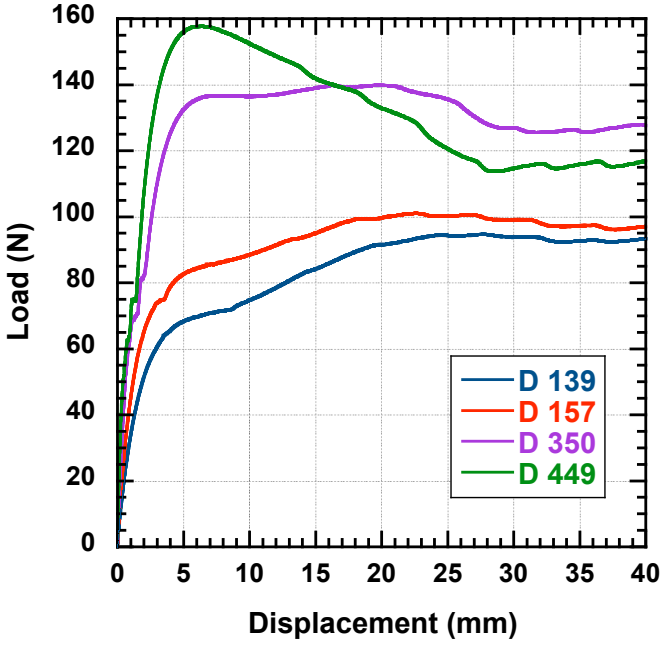
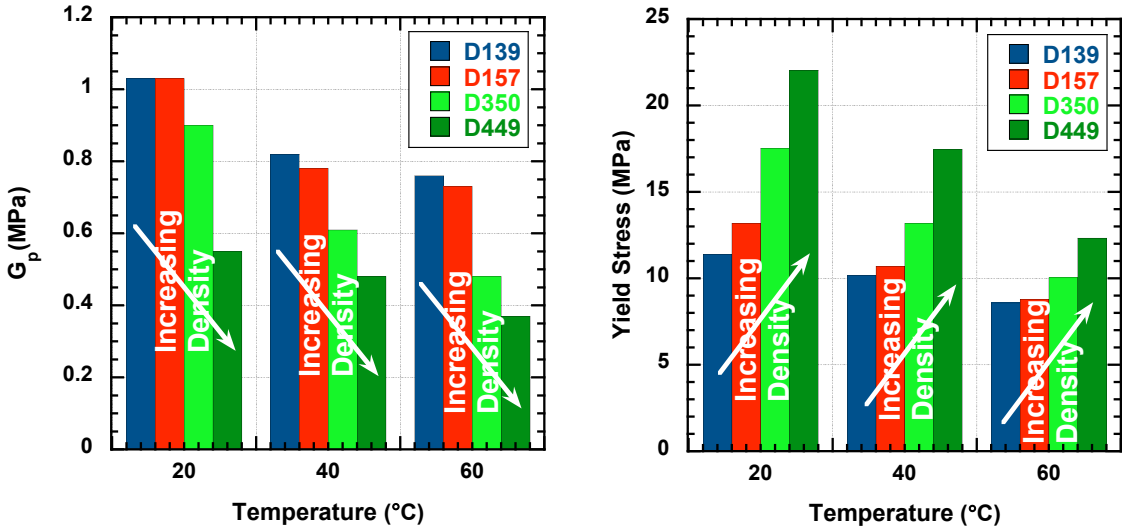


FIGURE 7.21: Effect of Density on the Tensile Deformation at a constant rate, 1.2 mm/min ($8 \times 10^{-4} s^{-1}$) and temperature 40°C

During testing, it was observed that necking took place in a different manner for some materials of the density series, as can be seen in Fig. 7.23 and can also be recognized in Fig. 7.21. When compared with the other materials, the previously observed sharp drop in load after necking did not occur especially in D139 and D157, which are the lower density materials. This can be explained by relating the necking behaviour to the structure. The density of these materials has been modified by branching effects while keeping the MW constant. These



(a) G_p (b) σ_y

FIGURE 7.22: Effect of density on strain hardening modulus and yield stress, 6mm/min ($4 \times 10^{-3} s^{-1}$)

highly branched samples having lower densities show greater strain hardening than others, which eliminates the post-yield load drop. Still taking the first *peak* as the maximum load in the yield stress calculations, adiabatic drawing stability is determined for each case using the same procedure.

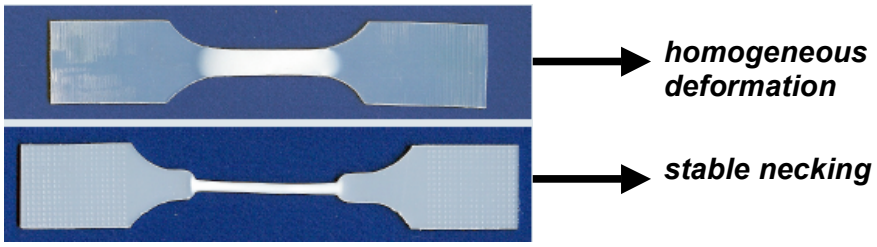


FIGURE 7.23: Observation of Necking Behaviour

Taking the error in the calculation of draw ratio and peak load due to uneven necking into account, the relationship found between w_{pl} and adiabatic drawing stability (as given in Fig. 7.24) is still promising. The adiabatic drawing stability parameter is found to increase with density as shown in Fig. 7.25, which is consistent with the crystallinity case given in Fig. 7.16.

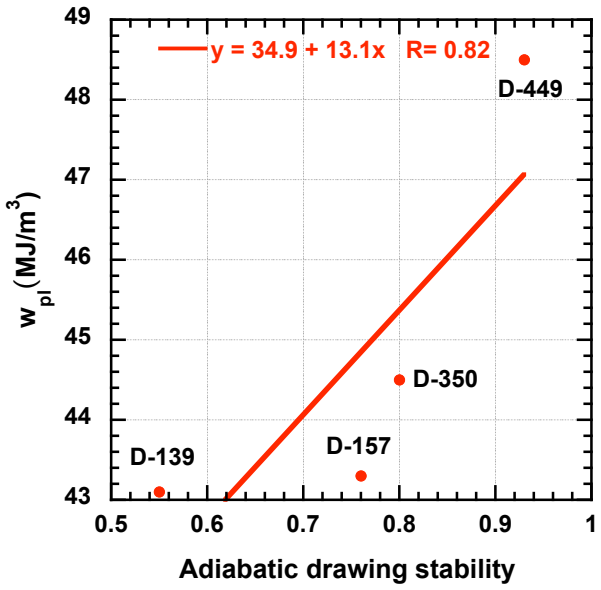


FIGURE 7.24: Correlation between adiabatic drawing stability and plane stress fracture resistance, at 0°C

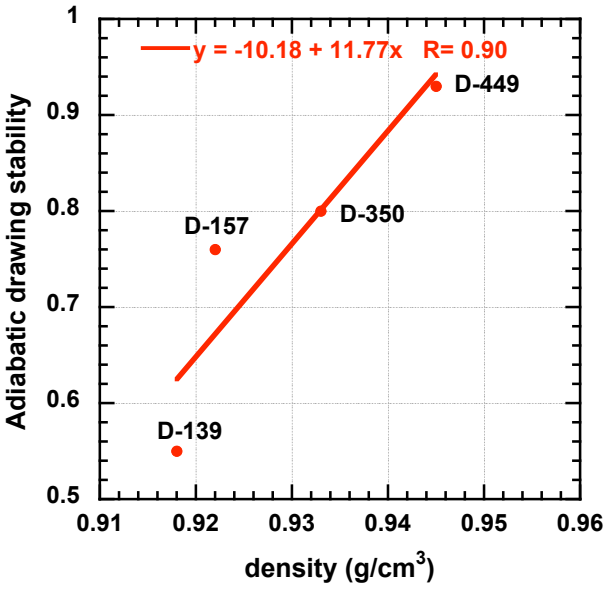


FIGURE 7.25: Effect of density on adiabatic drawing stability

Figure 7.22(a) shows that G_p decreases with temperature. A similar observation was made before [17, 90, 101, 107, 121] and this negative temperature dependence is attributed to the separation of the entanglements with increasing temperature. This result, contradicting with rubber elasticity, one more time suggests that G_p and σ_y are not really distinct parameters and that they are interrelated.

7.9.2.3 Effect of Molecular Weight: MW Series PE Resins

The effect of MW on the load-displacement traces can be seen in Fig. 7.26 where the curves are observed to shift upwards as the MW decreases (recalling that $MW4 > MW6 > MW5$ from Table. 5.4).

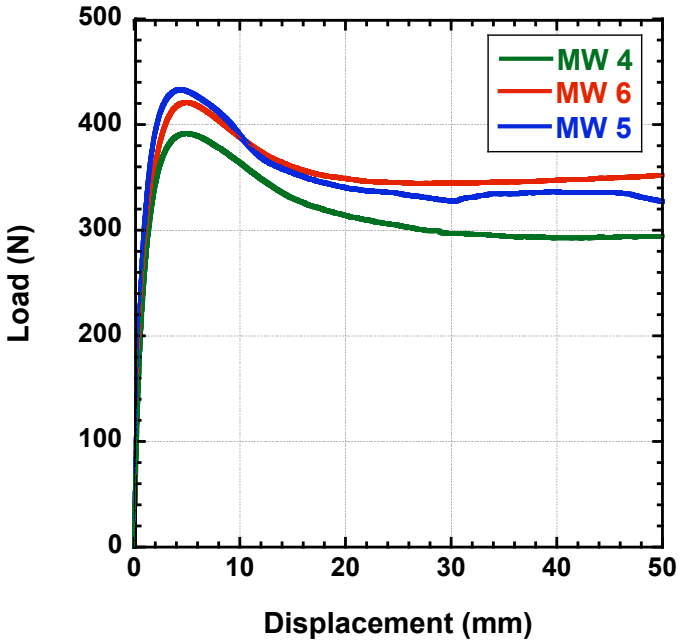
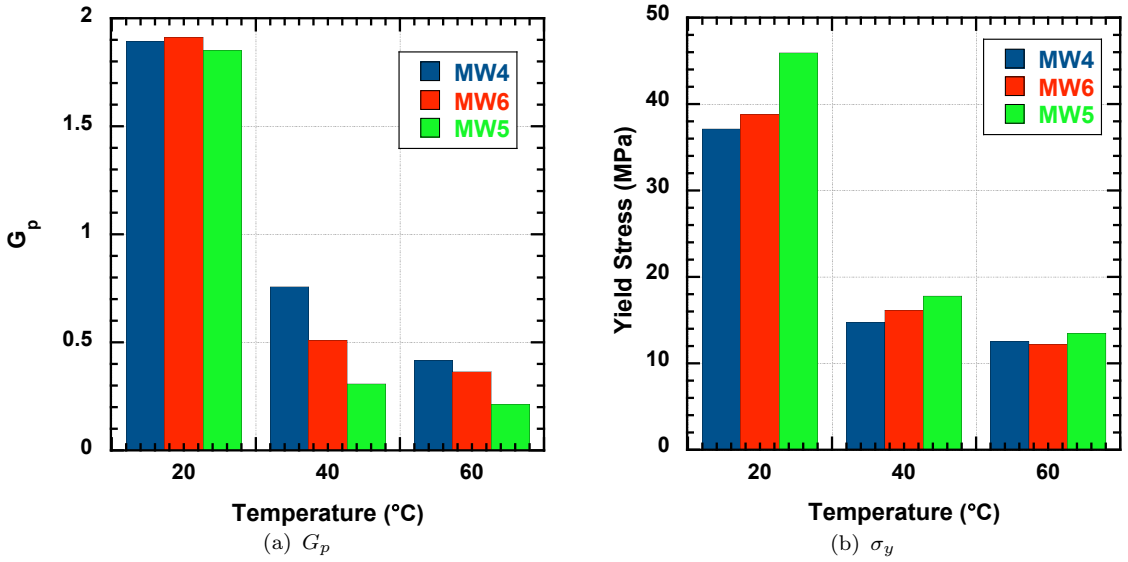


FIGURE 7.26: Effect of MW on the Tensile Deformation at Constant Temperature, 20°C and crosshead speed 1.2mm/min ($8 \times 10^{-4} s^{-1}$)

When the effect of MW on the HT model parameters is investigated as given in Fig. 7.27, it is seen that as the MW increases, G_p increases while σ_y decreases.

These observed results can be explained by referring to the material structure. As MW increases, the number of interlamellar tie molecules increases [18, 74, 83, 134, 136, 141], which plays an important role in the strain hardening properties of the material [18, 101, 140, 141]. Having tie molecules in the structure restricts the deformation process and hence, high molecular weight samples with many interlamellar links exhibit a higher strain hardening modulus [83]. On the other hand, the increase in MW, resulting in a decrease in crystallinity [27, 28, 101] makes it reasonable to observe a decrease in σ_y with increasing MW.



(a) G_p (b) σ_y

FIGURE 7.27: Effect of MW on strain hardening modulus and yield stress, 1.2 mm/min ($8 \times 10^{-4} s^{-1}$)

The parameters of Reversed Charpy and tensile tests (w_{pl} and adiabatic drawing stability) are again found to be related as shown in Fig. 7.28. Figure 7.29 shows how adiabatic drawing stability is affected from MW. The highly entangled structure in high MW materials increases strain hardening modulus resulting in lower elongation ratios as well as lower adiabatic drawing stability.

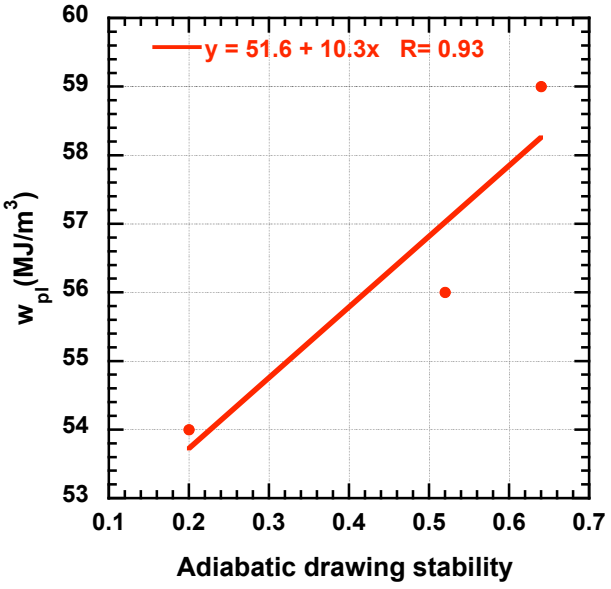


FIGURE 7.28: Correlation between adiabatic drawing stability (20°C, 1/s) and plane stress fracture resistance (0°C)

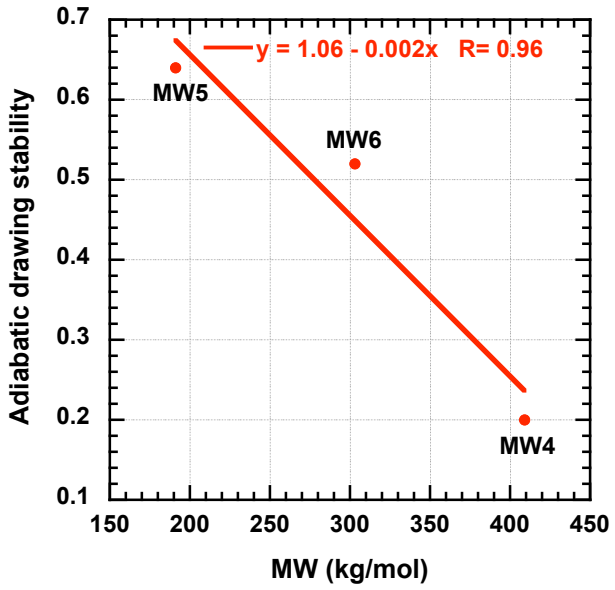


FIGURE 7.29: Effect of MW on adiabatic drawing stability, (20°C, 1/s)

7.10 Discussion and Conclusions

Specimen preparation is very important for the accuracy of the results of tensile tests. During neck formation if the cross-section of the specimen is not uniform, the element with the smallest effective cross-section is subjected to the highest true stress, and reaches the yield point before any other point in the specimen. Fluctuation in material properties may cause a localized reduction of the yield stress in an element, leading to this element reaching the yield point at a lower applied load. Following this, when an element reaches its yield point, the rest of necking continues on that element since it is easier due to its lower stiffness. Necking propagates along the material as other elements are brought to a similar stress-strain state. All these processes result in a non-uniform distribution of stress and strain along the length of the specimen. This is the reason why the load displacement curves should be investigated in detail for each case.

The analysis of the experimental results in this study has been based on the Haward-Thackray model and Gaussian rubber elasticity equation, that had been confirmed to be applicable to the current materials of interest by former researchers [101, 107, 110, 111, 112]. Rather than questioning or confirming the validity

of these models, the factors affecting the model parameters have been the main subject of this project.

As a result of the study, the idea of ranking the materials according to their adiabatic drawing stability is supported by experimental results. One term standing for resisting to separation by drawing (w_{pl}), and the other term referring to the stability of adiabatic drawing (β_c) are found to be related, validating the initial ideas and assumptions of this study.

The tensile deformation of polyethylene has been studied extensively and yet the structural basis underlying the deformation process is not well understood because of the complexity of the semicrystalline structure. The molecular structure and crystallisation conditions have a strong effect on the resulting parameters and in order to see the individual effect of each, isolation of one variable while holding the others constant has been applied to many properties. Each HT parameter is related to structure and affects the resulting β_c as shown in Fig. 7.30.

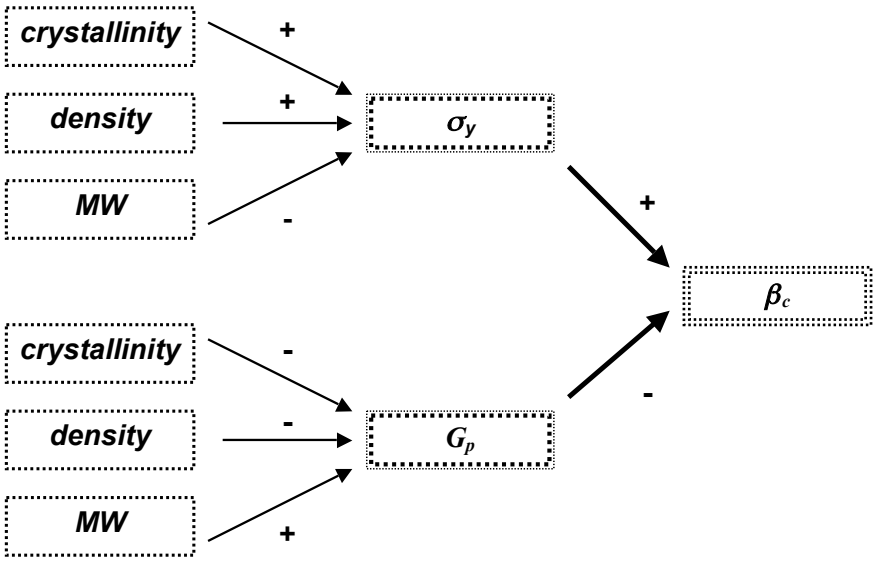


FIGURE 7.30: Relationship between the parameters

The individual effects of crystallinity, density and MW are shown in Table 7.2.

Parameters	σ_y	G_p	β_c	λ
Crystallinity $\uparrow$	$\uparrow$	$\downarrow$	$\uparrow$	$\uparrow$
Density $\uparrow$	$\uparrow$	$\downarrow$	$\uparrow$	$\uparrow$
Molecular Weight $\uparrow$	$\downarrow$	$\uparrow$	$\downarrow$	$\downarrow$

TABLE 7.2: Effect of structural changes on Tensile test parameters

Based on these results, in order to have a high adiabatic drawing stability, σ_y should be high while keeping G_p low. Relating this back to the material parameters, it is in favour of β_c to have high crystallinity and high density while having a low MW.

7.10.1 Sensitivity analysis

Sensitivity analysis is used to ascertain how β_c depends upon the input parameters. Taking the typical material property parameter values in Table 7.3 as a basis, each parameter in turn is changed to measure the resulting sensitivity of β_c to these values.

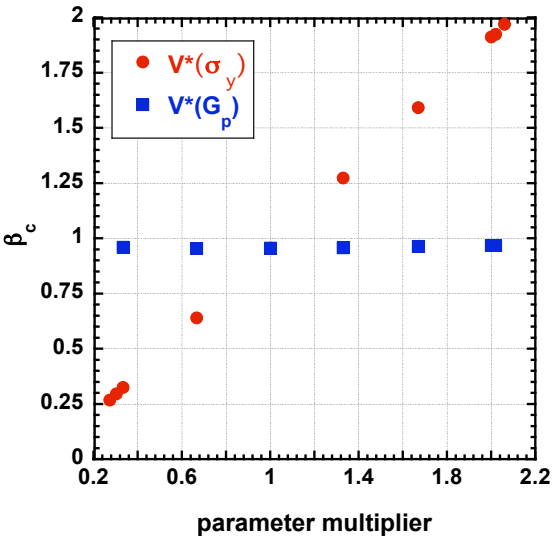
β_c=**0.956**	σ_y	G_p
V^*	3.3×10^{-3}	105×10^{-3}
ΔH	180×10^{3}	180×10^{3}
$\dot{\epsilon}_0$	4×10^{21}	4×10^{21}

TABLE 7.3: Base data used for sensitivity analysis

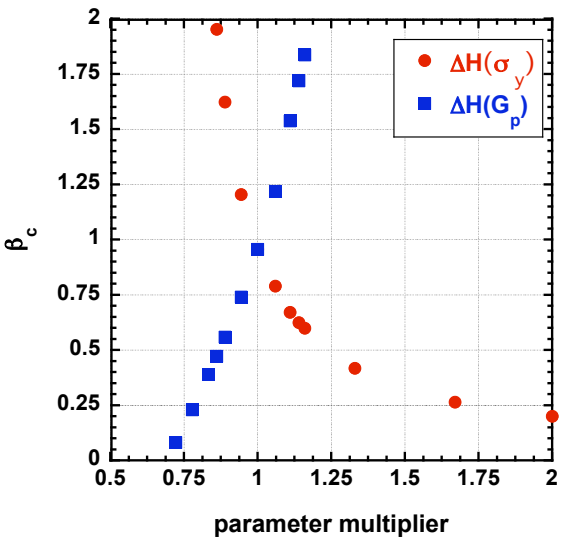
Sensitivity to V^*

V^* values are changed for both σ_y and G_p individually to see the effect on resulting β_c while keeping the rest of the parameters constant. As can be seen in Fig.

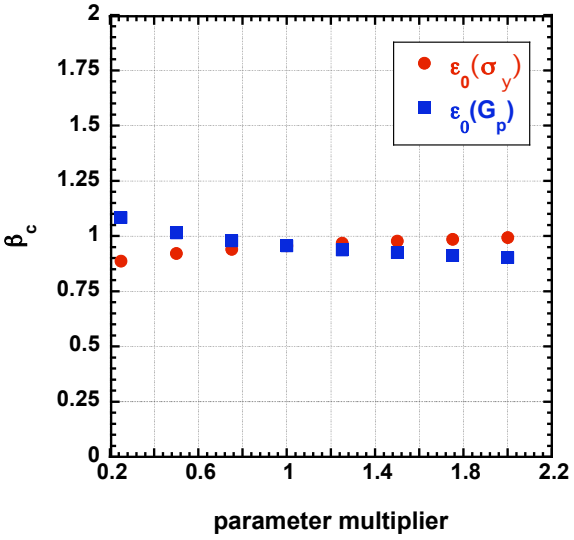
7.31(a), a change of activation volume has very little influence on strain hardening modulus. For the case of yield stress, there is almost a linear relationship observed. For a higher adiabatic drawing stability, it should be aimed to have a high activation volume for the yield process.



(a) Effect of V^*



(b) Effect of ΔH



(c) Effect of $\dot{\epsilon}_0$

FIGURE 7.31: Sensitivity analysis on adiabatic drawing stability

Sensitivity to ΔH

The same procedure is repeated to see how sensitive β_c is to the changes in ΔH. Both parameters' ΔH values are found to effect the results (Fig. 7.31(b)). Based on this case, it should be aimed to have a high ΔH for the strain hardening process and a low one for the yield stress process.

Sensitivity to $\dot{\epsilon}_0$

The same procedure is repeated again to see how sensitive β_c is to the changes in $\dot{\epsilon}_0$. The σ_y and G_p parameters have contradicting effects as shown in Fig. 7.31(c), and based on these, a high yield stress $\dot{\epsilon}_0$ should be aimed at, while strain hardening $\dot{\epsilon}_0$ should be kept low. When compared with the other cases, it can be concluded that change in $\dot{\epsilon}_0$ does not have a major influence on the adiabatic drawing stability.

If all the conditions are summarised based on σ_y; in order to have a high adiabatic drawing stability, V^* should be increased, ΔH should be decreased and $\dot{\epsilon}_0$ should be increased. Based on G_p, while V^* does not make a difference, ΔH should be increased and $\dot{\epsilon}_0$ should be decreased.

7.10.1.1 An alternative analysis method by reduction of parameters

Observing the results in Table 7.1, it can be seen that the ΔH and $\dot{\epsilon}_0$ values are almost the same for both yield and strain hardening processes. V^* appears to be the only parameter that is different. In order to investigate this observation in detail, ΔH and $\dot{\epsilon}_0$ parameters were forced to be equal for both yield and strain hardening processes using Microsoft Excel Solver function (this analysis was done only for C-Series PE resins, prepared at a cooling rate of 1.5 °C/min). The new parameters are given in Table 7.4, where the resulting β_c values of both original and new conditions are given as well.

Having reduced the parameters defining a material, it is possible to describe each material by a single ΔH, a single $\dot{\epsilon}_0$, in addition to $V^*(\sigma_y)$ and $V^*(G_p)$ parameters.

HT	σ_y	G_p	Common Parameters		β_c	β_c
PE ID	**V* x10^{-3} (m^3/mol)**	**V* x10^{-3} (m^3/mol)**	**ΔH (kJ/mol)**	$\dot{\epsilon}_0$ **x10^{21} (s^{-1})**	*original*	*new*
PE-2	2.85	99.2	133.4	4.13	0.74	0.65
PE-3	2.17	76.09	140.0	4.11	0.58	0.55
PE-4	3.29	105.3	180.3	4.07	0.94	0.95
PE-5	3.23	117.58	230.0	3.99	1.25	1.22
PE-6	2.70	104.4	174.7	4.07	0.73	0.77
PE-7	2.07	46.19	165.0	4.07	0.44	0.44
PE-8	2.90	115.3	180.0	4.07	0.88	0.85

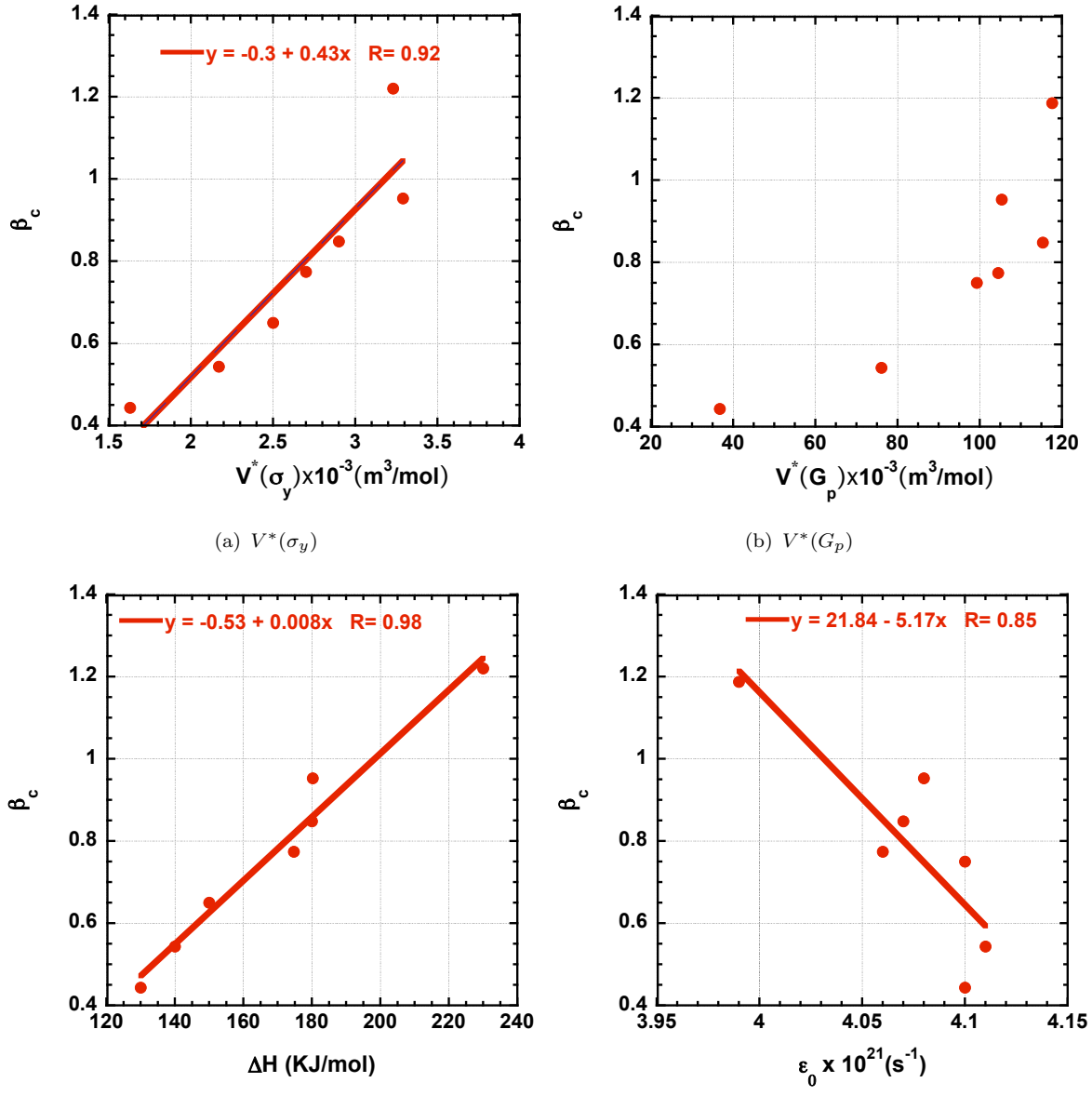
TABLE 7.4: Eyring rate constants for the HT model parameters

The effect of each parameter on adiabatic drawing stability can be seen in Fig. 7.32. Figure 7.33 shows that although $V^*(\sigma_y)$ and $V^*(G_p)$ have well-defined individual effects, their ratio does not.

By observing Fig. 7.32, it is possible to conclude that high adiabatic drawing stability can be obtained from processes having high ΔH and V^*, and low $\dot{\epsilon}_0$.

7.10.2 Relationship between Reversed Charpy and tensile test results

The Reversed Charpy test is used to measure the plane stress fracture resistance, which is effectively a measure of the toughness of the shear lips responsible for the crack arrest mechanism in RCP. Within the purposes of this study, it is very important to be able to define and relate this mechanism in order to predict the materials' RCP performance. Having this as the initial motive, the relationship found between the stable drawing parameter defined from tensile testing and plane stress resistance parameter from Reversed Charpy test has been very promising and satisfactory in terms of completing the mission of the study.



(a) $V^*(\sigma_y)$ (b) $V^*(G_p)$

(c) ΔH (d) $\dot{\epsilon}_0$

FIGURE 7.32: Effect of parameters on adiabatic drawing stability

According to the findings, the more stable the drawing of the system (higher β_c) means better the material, which corresponds to the higher plane stress fracture resistance (w_{pl}) and effectively better performance in the RCP (lower T_{BT}).

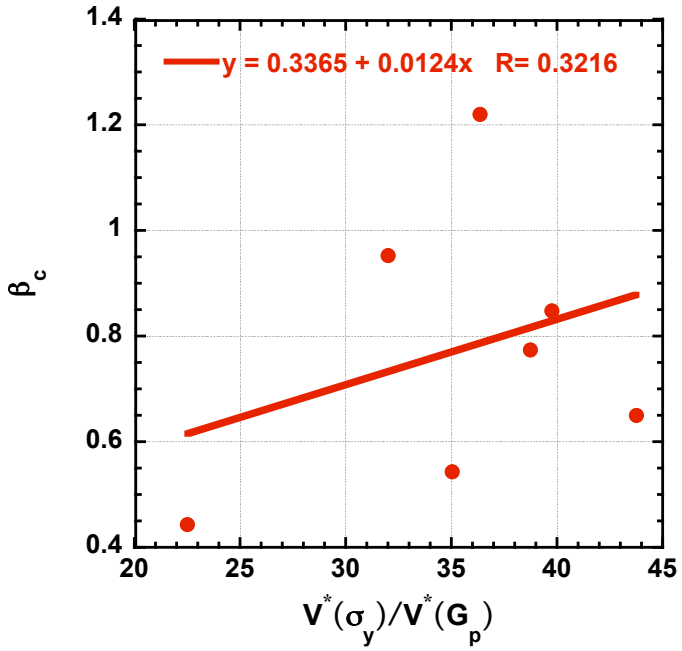


FIGURE 7.33: Effect of ratio of V* on β_c

Chapter 8

Conclusions and Recommendations for Future Work

8.1 Overview

The main objective of this study was to investigate the effect of structural parameters (crystallinity, density, molecular weight, and carbon black addition) on the RCP resistance of polyethylene pipe materials. To fulfil this aim, various groups of materials were tested by using various test methods.

The variation in crystallinity was achieved using a thermal conditioning press in which the cooling rates of PE plaques were controlled. As expected, higher cooling rates resulted in lower crystallinity while high crystallinity was achieved by slow cooling rates.

The density effect was investigated on a group of materials that had similar MW, while the MW effect was investigated on a group of materials that had similar densities but differing branching content. The Carbon Black group consisted of two pairs of polyethylene resins, each including a natural and carbon black filled

form of each material enabling us to see the effect of carbon black addition. In addition to these groups, another group of materials consisting of 7 different PE resins representing a wide range of different structures have been studied. All of these material groups had been specially prepared by Chevron Phillips Chemical Company for the purposes of this study.

One other aim of this study was to find a small scale test method to predict the RCP resistance of a pipe material. A method that would enable the prediction of a pipe material's performance prior to extrusion would be the ideal case. Pursuing this idea, in order to define such a test method, the underlying mechanism behind RCP phenomena should be understood first. Observing the fracture surface of RCP, it was seen that two basic mechanisms play an important role: plane stress and plane strain. Although plane strain fracture resistance is a very well known and well defined parameter, plane stress fracture resistance determination is not. Here we used the ISO CD 17281 Impact Bend Test for the determination of plane strain fracture resistance, while both Reversed Charpy and Tensile tests were used to investigate the plane stress fracture resistance mechanism.

In this chapter the major conclusions are summarised and some further studies are recommended to be continued in the future.

8.2 S4 Test Results

The effects of extrusion rate, temperature, screw type and carbon black addition on T_{c-S4} were investigated using S4 tests on pipe having 59 mm OD and with an SDR of 11. Based on the material groups tested here, it can be concluded that CB addition either leads to better S4 performance, in terms of decreasing T_{c-S4}, or does not have any effect. Increasing extrusion rate was found to improve the S4 performance, while neither extrusion screw type nor extrusion set temperature parameters were found to have a consistent effect on the materials tested. Due to lack of information on material properties, no further conclusions could be made.

8.3 Effect of structural changes on test parameters

The summary of the experimental results based on the effects of structural parameters is given in Table. 8.1.

Tests	***ISO CD 17281***		***Rev. Charpy***		***Tensile Test***			
Parameters	G_c	T_{BT}	w_{pl}	σ_y	σ_y	G_p	β_c	λ
Crystallinity ↑	slight ↓	↓	↑	↑	↑	↓	↑	↑
Density ↑	↓	↓	↑	↑	↑	↓	↑	↑
MW ↑	↑	n/a	↓	↓	↓	↑	↓	↓
Carbon Black ↑	↓	↓	n/a	↑	n/a	n/a	n/a	n/a

TABLE 8.1: Effect of structural changes on test parameters

8.4 Arc-Shaped geometry factor determination

As shown in detail in Chapter 3, the arc-shaped geometry factor was determined for a wide range of pipe geometries aiming to determine precise G_c values. The arc-shaped specimens were found to be more compliant when compared with the rectangular plaque specimens. This effectively results in moulded arc-shaped specimens having higher brittle-tough transition temperature values than plaque specimens of the same material. Being more compliant, the arc-shaped specimens store more energy at fracture. As a result, arrest requires more energy absorbtion by the shear lips, requiring an increase in the temperature.

8.5 Uniaxial Tensile Test

Adiabatic drawing stability, being related to both σ_y and G_p processes taking place during tensile deformation, is consequently affected from the material properties influencing these parameters as shown in Fig. 7.30. High crystallinity, high density and low MW is found to be in favour of high adiabatic drawing stability.

Gaussian strain hardening modulus (G_p) was found to decrease with temperature which is inline with the previous work in the area [90, 101, 121], but contradicts with the rubber elasticity theory. This result together with obtained ΔH and $\dot{\epsilon}_0$ values being the same for both yield and strain hardening processes, can be considered as an indication of a single process taking place during deformation rather than both.

Further analysis done on the results by forcing them to be equal and looking at the individual effects of the parameters on adiabatic drawing stability had shown that these two processes are not really distinguishable, and that it is very difficult to separate their effects in a general way. Rather than the effect of G_p and σ_y separately, defining them by the Eyring parameters (V^*, ΔH and $\dot{\epsilon}_0$) is found to be more informative and based on the results here, it can be concluded that high plane stress resistance is associated with high $V^*(G_p)$, $V^*(\sigma_y)$ and ΔH.

8.6 Relationships between the test results

S4 Test and Instrumented Charpy Test

In terms of S4 critical temperature results, the best assessment of resins using the Instrumented Charpy test was given using pipe specimens, followed by the plaque specimens that were prepared with a cooling rate of 1.5 °C/min (as shown in Fig. 5.29).

S4 Test and Reversed Charpy Test

Observation of shear lips during the studies of RCP led to the conclusion that the main mechanism resisting crack propagation is shear lips. Forming near the free surface, they have various thickness along the crack length, and the amount they extent is material dependent. The formation of these shear lips can be related to ductility since they do not form below T_{BT}. From the results obtained in this study, it can be concluded that as cooling rate decreases, w_{pl} increases, which is also in line with the observed decrease in T_{c-S4} due to slow cooling.

Reversed Charpy Test and Tensile Test

One term standing for resisting to separation by drawing (w_{pl}), and the other term referring to the stability of drawing (β_c) were found to be in good agreement validating the initial ideas and assumptions of this study.

In order to have high RCP resistance (low T_{c-S4}), the material should exhibit high plane stress fracture resistance, which means having high adiabatic drawing stability. Based on the results of this study, in order to have high adiabatic drawing stability (stable drawing), the material should have high crystallinity and high density while having a low MW.

Having this relationship is important in the sense that RCP mechanism can be related to the very basic polyethylene structure, which enables us to predict the performance of the resulting pipe prior to its extrusion, and may eventually even enable us to design a desired pipe performance by altering the initial structural parameters.

8.7 Recommendations for future work

The method of G_c determination from the load-displacement curves should be improved, and generalised taking all aspects of loading into account. Especially

for highly ductile materials, the non-linear loading and unloading parts should be examined.

Although this study covers the effect of structural parameters on the test results, the interpretation of the results could not go any further than some general concepts due to the lack of morphological studies. More advanced results can be obtained if the detailed morphology of the specimens are studied.

The tensile section of this study covers only the effects of structural parameters on the results. The applicability of the models used here was not questioned: it was assumed to be satisfactory based on the previous studies in the area [80, 90, 107, 110, 111]. Based on the models used here, the results were found to be satisfactory. But this finding is limited to the materials used here, and can be improved by testing different materials than PE. Using different models in the literature would enable to generalise and improve the findings since the models used here are very basic.

The tensile test analysis scheme developed here can be used to represent each material using four Eyring parameters (ΔH, $\dot{\epsilon}_0$, $V^*(\sigma_y)$ and $V^*(G_p)$) and the adiabatic drawing stability analysis shows how these determine the plane stress fracture resistance. Future work should focus on gaining a deeper understanding of how the polymer structure influences these parameters.

References

[1] William D. Callister. *Materials Science and Engineering: an introduction*. John Wiley and Sons, 5th edition, 2000.

[2] Alexis Paizis. *Orientation and Strain Cycle Effects on the RCP Resistance of Polyethylene Resins*. PhD thesis, Imperial College of Science Technology and Medicine, 2004.

[3] L. Lin and A. S. Argon. Review: Structure and plastic deformation of polyethylene. *Journal of Materials Science*, 29(2):294–323, 1994.

[4] H. R. Dennis et. al. Nanocomposites by extruder processing. In *SPE/Antec Conference*, Atlanta, 1998.

[5] S. Derrible et. al. 3M group design project: Thermal conditioning rig. Technical report, Imperial College London, 2005.

[6] J. W. S. Hearle, B. Lomas, and W. D. Cooke. *Atlas of fibre fracture and damage to textiles*. Woodhead Publishing, 2nd edition, 1998.

[7] P. E. Reed and G. Q. Zhao. Structural deformation in polyethylene during cold-drawing. *Journal of Materials Science*, 17(11):3327–3335, 1982.

[8] G.P. Venizelos, C. J. Greenshields, A. Ivankovic, and P. S. Leevers. Fast brittle fracture of plastic pipes Part 2- Gas Pressurised. *Plastics, Rubber and Composites Processing and Applications*, 26(9):394–403, 1997.

[9] C. J. Greenshields. Fast brittle fracture of plastic pipes Part 1-Water Pressurised. *Plastics, Rubber and Composites Processing and Applications*, 26(9):387–393, 1997.

[10] P.J. DesLauriers, M. P. McDaniel, D. C. Rohlfing, R. K. Krishnaswamy, S. J. Secora, E. A. Benham, P. L. Maeger, A.R. Wolfe, A. M. Sukhadia, and B. B. Beaulieu. A comparative study of multimodal vs. bimodal polyethylene pipe resins for PE-100 applications. *Polymer Engineering and Science*, 45(9):1203–1213, 2005.

[11] C. J. Greenshields, P. Davis, and P.S. Leevers. Fast brittle fracture of plastic pipes Part 3- Materials and processing. *Plastics, Rubber and Composites Processing and Applications*, 26(9):404–411, 1997.

[12] E. Orowan. Fracture and strength of solids. *Reports on Progress in Physics*, 12(3):185, 1949.

[13] R. J. Young and P. A. Lovell. *Introduction to Polymers*. Cambridge University Presss, London, 2nd edition, 1991.

[14] L. H. Sperling. *Introduction to Physical Polymer Science*. Wiley-Interscience, 2nd edition, 1992.

[15] N. G. McCrum, C. P. Buckley, and C. B. Bucknall. *Principles of Polymer Engineering*. Oxford University Press, 2nd edition, 2000.

[16] Q. Fu, Y. Men, and G. Strobl. A molar mass induced transition in the yielding properties of linear polyethylene. *Polymer*, 44(6):1941–1947, 2003.

[17] A. Peterlin. Molecular model of drawing polyethylene and polypropylene. *Journal of Materials Science*, 6(6):490–502, 1971.

[18] J. M. Andrews and I. M. Ward. The cold-drawing of high density polyethylene. *Journal of Materials Science*, 5(5):411–417, 1970.

[19] http://www.polymer age.co.uk/archive4.htm. Higher performance claimed for new PE 100 pipe grade HDPE, 1998.

[20] R. K. Krishnaswamy and M. J. Lamborn. PE pipes and applications, 2006.

[21] L. Mandelkern. Crystals and long-chain molecules. *Accounts of chemical research*, 9(3):81–87, 1976.

[22] A. Keller. Polymer crystals. *Reports on Progress in Physics*, 31(2):623–704, 1968.

[23] P. J. Flory. On the morphology of the crystalline state in polymers. *Journal of the American Chemical Society*, 84(15):2857–2865, 1962.

[24] T. Amornsakchaia, R. H. Olleya, D. C. Bassett, M. O. M. Al-Husseinb, A. P. Unwinb, and I. M. Ward. On the influence of initial morphology on the internal structure of highly drawn polyethylene. *Polymer*, 41(23):8291–8298, 2000.

[25] D.H. Isaac, E. Ecott, R. Perridge, and J.F.T. Pittman. Transfer coefficients in spray cooling of plastic pipes. In Institute of Materials, editor, *Plastic Pipes IX, Proceedings of Conference*, pages 534–541, Edinburgh, UK, 1995.

[26] G. L. Pitman and I. M. Ward. Effect of molecular-weight on craze shape and fracture-toughness in polycarbonate. *Polymer*, 20(7):895–902, 1979.

[27] Leo Mandelkern. Crystallization kinetics of homopolymers: overall crystallization: A Review. *Biophysical Chemistry*, 112(2-3):109–116, 2004.

[28] L. Mandelkern. The structure of crystalline polymers. *Accounts of Chemical Research*, 23(11):380–386, 1990.

[29] M. Avrami. Kinetics of phase change I-III. *The Journal of Chemical Physics*, 7(12):1103–1112, 1939.

[30] M. Avrami. Kinetics of phase change I-III. *The Journal of Chemical Physics*, 8(2):212–224, 1940.

[31] M. Avrami. Kinetics of phase change I-III. *The Journal of Chemical Physics*, 9:177–184, 1941.

[32] H. D. Keith and F. J. Padden. Spherulitic crystallization from the melt. I. Fractionation and impurity segregation and their influence on crystalline morphology. *Journal of Applied Physics*, 35(4):1270–1285, 1964.

[33] J. D. Hoffman. Role of reptation in the rate of crystallization of polyethylene fractions from the melt. *Polymer*, 23(5):656–670, 1982.

[34] F. Goler and G. Sachs. Zur kinetik von kristallisations-vorgngen. *Zeitschrift fr Physik A Hadrons and Nuclei*, 77:281, 1932.

[35] R. Krishnaswamy. Carbon black filler, 2005.

[36] F. Ramsteiner. Failure of polymers by rupture versus disentanglement of molecules. In *Application of Fracture Mechanics to Polymers, Adhesives and Composites*, volume 33, pages 31–37. Elsevier Science Ltd, 2004.

[37] Z. Major and R.W. Lang. Rate dependent fracture toughness of plastics. *Journal De Physique IV*, 110(1):531–536, 2003.

[38] A. A. Griffith. The phenomena of rupture and flow in solids. *Philosophical Transactions of the Royal Society of London*, A(221):163–198, 1920.

[39] G. R. Irwin. Fracture dynamics. In *Conference Proceedings of Fracturing of Metals*, pages 147–166, Cleveland, 1948.

[40] P. S. Leevers and J. G. Williams. Double torsion testing of high velocity crack resistance. *Journal of Materials Science*, 22(3):1097–1107, 1987.

[41] C. J. Greenshields and P. S. Leevers. Rapid crack propagation in plastic water pipes: measurement of dynamic fracture resistance. *Internal Journal of Fracture*, 79(1):85–95, 1996.

[42] S. J. Youd. *The effects of crosslinking on the fracture properties of high and medium density polyethylene*. PhD thesis, Manchester Politechnic, 1991.

[43] P. S. Leevers and R. E. Morgan. Impact fracture of polyethylene : A non-linear-elastic thermal decohesion model. *Engineering Fracture Mechanics*, 52(6):999–1014, 1995.

[44] P. S. Leevers. Impact and dynamic fracture resistance of crystalline thermoplastics: prediction from bulk properties. *Polymer Engineering and Science*, 36(18):2296–2304, 1996.

[45] P. S. Leevers. Impact and dynamic fracture of tough polymers by thermal decohesion in a dugdale zone. *International Journal of Fracture*, 73(2):109–127, 1995.

[46] P. S. Leevers, S. Hazra, and S. Hillmansen. Impact resistance of thermoplastics - prediction from bulk properties. *Plastics Rubber and Composites*, 29(9):460–467, 2000.

[47] M. Douglas. *Impact Fracture of Engineering Polymers*. PhD thesis, University of London, 1998.

[48] J.G. Williams. *Fracture Mechanics of Polymers*. Halsted Press, London, 1987.

[49] C.Argyrakis. FEM analysis of arc-shaped specimens, 2007.

[50] E. Plati and J.G. Williams. The determination of the fracture parameters for polymers in impact. *Polymer Engineering and Science*, 15(6):470–477, 1975.

[51] B. Cotterell and J. Reddel. The essential work of plain stress ductile fracture. *International journal of fracture*, 13(3):267–275, 1977.

[52] W.K.Y. Poon, E.C.Y. Ching, C.Y.Cheng, and R.K.Y Li. Measurement of plane stress essential work of fracture (EWF) for polymer films: Effects of gripping and notching methodology. *Polymer Testing*, 20(4):395–401, 2001.

[53] P. Luna, C. Bernal, A. Cisilino, P. Frontini, B. Cotterell, and Y. W. Mai. The application of the essential work of fracture methodology to the plane strain fracture of ABS 3-point bend specimens. *Polymer*, 44(4):1145–1150, 2003.

[54] Y. W. Mai, B. Cotterell, R. Horlyck, and G. Vigna. The essential work of plane stress ductile fracture of linear polyethylenes. *Polymer Engineering and Science*, 27(11):804–808, 1987.

[55] J. S. Wu, Y-W Mai, and B. Cotterell. Prediction of the initiation of ductile fracture. *Journal of Material Science*, 43(5):793–810, 1993.

[56] D. E. Mouzakis and J. Karger-Kocsis. Essential work of fracture: application for polymers showing ductile-to-brittle transition during fracture. *Polymer Bulletin*, 42(4):473–480, 1999.

[57] L. Fasce, C. Bernal, P. Frontini, and Y. Mai. On the impact essential work of fracture of ductile polymers. *Polymer Engineering and Science*, 41(1):1–14, 2001.

[58] T. Barany. Essential work of fracture concept in polymers. *Periodica Polytechnica Ser. Mech. Eng.*, 47(2):91–102, 2003.

[59] R. S. Yamakawa. Influence of notching and molding conditions on determination of EWF parameters in polyamide 6. *Polymer Testing*, 23(2):195–202, 2004.

[60] V. Pettarin, P. M. Frontini, and G. E. Elicabe. Optimal ligament lengths in impact fracture toughness estimation by the essential work of fracture method. *Polymer Testing*, 24(2):189–196, 2005.

[61] P. Davis. *Process/property interactions in the new polyethylenes*. PhD thesis, Imperial College of Science, Technology and Medicine, 1999.

[62] R. E. Morgan. *Ductile-brittle transitions in pipe grade polyethylene*. PhD thesis, Imperial College of Science, Technology and Medicine, 1994.

[63] G. R. Irwin and H. T. Corten. Evaluating the feasibility of basing pipeline operating pressure on in-place hydrostatic test pressure. *Report to Northern Natural Gas Company and El Paso Natural Gas Company*, 1968.

[64] ISO 13478:2007. Thermoplastics pipes for the conveyance of fluids – determination of resistance to rapid crack propagation (RCP) – full-scale test (FST), 2007.

[65] P. Yayla. *Rapid Crack Propagation in Polyethylene Gas Pipes*. PhD thesis, Imperial College of Science, Technology and Medicine, 1991.

[66] P. S. Leevers. Rapid crack propagation the failure mode that never was? *Plastics, Rubber and Composites Processing and Applications*, 27(9):410–414, 1998.

[67] C. J. Greenshields and P. S. Leevers. Correlation between full scale and small scale steady state (S4) tests for rapid crack propagation in plastic gas pipe. *Plastics Rubber and Composites*, 28(1):20–25, 1999.

[68] S. J. Ritchie, P. Davis, and P. S. Leevers. Brittle-tough transition of rapid crack propagation in polyethylene. *Polymer*, 39(25):6657–6663, 1998.

[69] J. Niglia, A. Cisilino, R. Seltzer, and P. Frontini. Determination of impact fracture toughness of polyethylene using arc-shaped specimens. *Engineering Fracture Mechanics*, 69(12):1391–1399, 2002.

[70] ISO 17281. Plastics-determination of fracture toughness at moderately high loading rates (1 m/s), 2002.

[71] C. Pearson. 4M Final year project : Estimating plane stress fracture resistance of PE from tensile data. Technical report, Imperial College London, 2006.

[72] P. S. Leevers. Plastics-determination of impact plastic work dissipation-Reversed Charpy test, 2005.

[73] R. K. Krishnaswamy, P. S. Leevers, M. J. Lamborn, D. F. Register, A. M. Sukhadia, and P. L. Maeger. Rapid crack propagation failures in HDPE pipes: Some structure-property investigations. *Polymer Engineering and Science*, 46(10):1358–1362, 2001.

[74] X. Lu, R. Qian, and N. Brown. The effect of crystallinity on fracture and yielding of polyethylenes. *Polymer*, 36(22):4239–4244, 1995.

[75] N. Brown and I. M. Ward. The influence of morphology and molecular weight on ductile-brittle transitions in linear polyethylene. *Journal of Materials Science*, 18(5):1405–1420, 1983.

[76] J. T. Graham, R. G. Alamo, and L. Mandelkern. The effect of molecular weight and crystallite structure on yielding in ethylene copolymers. *Journal of Polymer Science*, 35(2):213–223, 1997.

[77] P. Prentice. The influence of molecular weight on the fracture of thermoplastic glassy polymers. *Journal of Materials Science*, 20(4):1445–1454, 1985.

[78] E. Q. Clutton, L.J. Rose, and G. Capaccio. Slow crack growth and impact mechanisms in polyethylene. *Plastics, Rubber and Composites Processing and Applications*, 27(10):478–482, 1998.

[79] L. Moreno and P.S. Leevers. Effect of axial surface scores on rapid crack propagation in polyethylene pipe. *Plastics Rubber and Composites: Macromolecular Engineering*, 33(4):149–154, 2004.

[80] S. Hillmansen. *Large Strain bulk deformation and brittle-tough transitions in polyethylene*. PhD thesis, Imperial College of Science, Technology and Medicine, 2001.

[81] P. G. Harry and G. P. Marshall. Use of instrumented impact testing to characterise failure in pressure pipe grades of MDPE and HDPE. In Plastics and London Rubber Institute, editors, *Plastic and Rubber International*, volume 16, pages 10–13, 1991.

[82] N. Brown and X. Lu. The dependence of rapid crack propagation in polyethylene pipes on the plane stress fracture energy of the resin. *Polymer Engineering and Science*, 41(7):1140–1145, 2001.

[83] M. A. Kennedy, A. J. Peacock, M. D. Failla, J. C. Lucas, and L. Mandelkern. Tensile properties of crystalline polymers: Random copolymers of ethylene. *Macromolecules*, 28(5):1407–1421, 1995.

[84] C.Argyrakis. Dynamic fracture resistance values, 2007.

[85] P. S. Leevers. RCP in PE pipe: how does it depend on plane stress and plane strain frcature properties?, 2007.

[86] P. S. Leevers, R. N. Haward, S. Hazra, and S. Hillmansen. Fast fracture of thermoplastics as a micro-scale tensile drawing process. *Fracture of Polymers, Composites and Adhesives*, 27(12):335–345, 2000.

[87] S. Hillmansen and R. N. Haward. Adiabatic failure in polyethylene. *Polymer*, 42(22):9301–9312, 2001.

[88] P. I. Vincent. Deformation and fracture of high polymers. page 287. Plenum Press, New York, 1974.

[89] G. Meinel and A. Peterlin. Plastic deformation of polyethylene II. change of mechanical properties during drawing. *Journal of Polymer Science*, 2(9):67, 1971.

[90] C. G'Sell and J. J. Jonas. Determination of the plastic behaviour of solid polymers at constant true strain rate. *Journal of Materials Science*, 14(3):583–596, 1979.

[91] P. S. Hope, I. M. Ward, and A. G. Gibson. The hydrostatic extrusion of poly(methyl methacrylate). *Journal of Materials Science*, 15(9):2207–2227, 1985.

[92] R. Hiss and G. Strobl. Deformation, yield and fracture of polymers. In *Institute of Materials*, page 439, Cambridge, 1997.

[93] J. Sweeney, T. L. D. Collins, P. D. Coates, A. P. Unwin, R. A. Duckett, and I. M. Ward. Application of a large deformation model to unstable tensile stretching of polyethyelene. *International Journal of Plasticity*, 18(3):399–414, 2002.

[94] R. N. Haward and G. Thackray. The use of a mathematical model to describe isothermal stress-strain curves in glassy thermoplastics. *Proceedings of the Royal Society of London. Series A, Mathematical and Physical Sciences*, 302(1471):453–472, 1968.

[95] M. C. Boyce, D. M. Parks, and A. S. Argon. Large inelastic deformation of glassy polymers. I. Rate dependent constitutive model. *Mechanics of Materials*, 7(1):15–33, 1988.

[96] M. C. Boyce, D. M. Parks, and A. S. Argon. Plastic flow in oriented glassy polymers. *International Journal of Fracture*, 5(6):593–615, 1989.

[97] E. M. Arruda and M. C. Boyce. Evolution of plastic anisotropy in amorphous polymers during finite straining. *International Journal of Plasticity*, 9(6):697–720, 1993.

[98] C. P. Buckley and D. C. Jones. Glass-rubber constitutive model for amorphous polymers near the glass transition. *Polymer*, 36(17):3301–3312, 1995.

[99] C. P. Buckley, P. J. Dooling, J.Harding, and C.Ruiz. Deformation of thermosetting resins at impact rates of strain. Part 2: constitutive model with rejuvenation. *Journal of Mechanics and Physics of Solids*, 52(10):2355–2377, 2004.

[100] P. D. Wu and E. van der Geissen. On improved network models for rubber elasticity and their application to orientation hardening in glassy polymers. *Journal of the Mechanics of Physics of Solids*, 41(3):427–456, 1993.

[101] S. Hillmansen, S. Hobeika, R. N. Haward, and P. S. Leevers. The effect of strain rate, temperature, and molecular mass on the tensile deformation of polyethylene. *Polymer Engineering and Science*, 40(2):481–489, 2000.

[102] S. J. K. Ritchie. A model for the large-strain deformation of polyethylene. *Journal of Materials Science*, 35(23):5829–5837, 2000.

[103] C. G'Sell, J. M. Hiver, and A. Dahoun. Experimental characterization of deformation damage in solid polymers under tension, and its interrelation with necking. *Internal Journal of solids and structures*, 39(13-14):3857–3872, 2002.

[104] P. I. Vincent. The physical basis of yield and fracture. page 155, Oxford, 1966.

[105] A. S. Krausz and H. Eyring. *Deformation Kinetics*. John Wiley and Sons, New York, 1975.

[106] P. J. Mills, J. N. Hay, and R. N. Hayward. The post-yield behaviour of low-density polyethylenes. *Journal of Materials Science*, 20(3):501–507, 1985.

[107] R. N. Haward. Strain hardening of thermoplastics. *Macromolecules*, 26(22):5860–5869, 1993.

[108] A. Cohen. A Pade approximation to the inverse Langevin function. *Rheologica Acta*, 30(3):270–273, 1991.

[109] A. S. Argon. Physical basis of distortional and dilational plastic flow in glassy polymers. *Journal of Macromolecular Science. Part A: Pure and applied chemistry*, 8(3):573–596, 1973.

[110] C. G'Sell and J. J. Jonas. Yield and transient effects during the plastic deformation of solid polymers. *Journal of Materials Science*, 16(7):1956–1974, 1981.

[111] A. Cross and R. N. Haward. Orientation hardening of PVC. *Polymer*, 19:677–682, 1978.

[112] R. N. Haward. The adiabatic fracture of thermoplastic fibres. *Journal of Materials Science*, 38(10):2155–2160, 2003.

[113] S. M. Crawford and H. Kolsky. The relation between stress, strain and birefringence in some high polymers. *Proceedings of the Physical Society*, B64(1):119–125, 1951.

[114] R. N. Haward. Heating effects in the deformation of thermoplastics. *Thermochimica Acta*, 247(1):87–109, 1994.

[115] I. Brough, R. N. Haward, G. Healey, and A. Wood. Scanning electron micrographs of high density polyethylene fracture surfaces. *Polymer*, 45(10):3115–3123, 2004.

[116] A. Cross and R. N. Haward. Thermal fracture of plastics. *Journal of Polymer Science: Polymer Physics Edition*, 11(12):2423–2439, 1973.

[117] J. Williams. Visco-elastic and thermal effects on crack growth in PMMA. *International Journal of Fracture*, 8(4):393–401, 1972.

[118] J. T. Dickinson, I. C. Jensen, S. C. Langford, and R. P. Dion. Temperature measurements of the gaseous emission during the fracture of polystyrene: a determination of the fracture energy and fracture surface temperature. *Journal of Polymer Science Part B: Polymer Physics*, 32(4):779–784, 1994.

[119] K. N. G. Fuller, P. G. Fox, and J. E. Field. The temperature rise at the tip of fast-moving cracks in glassy polymers. *Proceedings of Royal Society of London*, 341(1627):537–557, 1975.

[120] G. Farruggio. Experimental studies of neck formation and propagation in polyethylene. Technical report, University of London, 1996.

[121] R. Hiss, S. Hobeika, C. Lynn, and G. Strobl. Network stretching, slip processes, and fragmentation of crystallites during uniaxial drawing of polyethylene and related copolymers. A comparative study. *Macromolecules*, 32(13):4390–4403, 1999.

[122] U. Gaur and B. Wunderlich. Heat capacity and other thermodynamic properties of linear macromolecules. II. Polyethylene. *Journal of Physical and Chemical reference data*, 10(1):119, 1981.

[123] Q. Fu, Y. Men, and G. Strobl. Understanding of the tensile deformation in HDPE/LDPE blends based on their crystal structure and phase morphology. *Polymer*, 44(6):1927–1933, 2003.

[124] J.M. Peterson. Thermal initiation of screw dislocations in polymer crystal platelets. *Journal of applied Physics*, 37(11):4047–4050, 1966.

[125] R. J. Young. A dislocation model for yield in polyethylene. *Philosophical Magazine*, 30(1):85–93, 1974.

[126] P. J. Flory and D. Y. Yoon. Molecular morphology in semicrystalline. polymers. *Nature*, 272(10):226–229, 1978.

[127] P. B. Bowden and S. Raha. A molecular model for yield and flow in amorphous glassy polymers making use of a dislocation analogue. *Philosophical Magazine*, 29(1):149–166, 1974.

[128] D. Roylance. Stress-strain curves, 2001.

[129] N. W. Brooks, M. Ghazali, R. A. Duckett, A. P. Unwin, and I. M. Ward. Effects of morphology on the yield stress of polyethylene. *Polymer*, 40(4):821–825, 1999.

[130] S. Nikolov and D. Raabe. Yielding of polyethylene through propagation of chain twist defects: Temperature, stem length and strain-rate dependence. *Polymer*, 47(5):1696–1703, 2006.

[131] A. J. Peacock, L. Mandelkern, and R. G. Alamo. The influence of the deformation temperature on the tensile properties of polyethylenes. *Journal of Materials Science*, 33(9):2255–2268, 1998.

[132] G. Kanig. Application of the short-time staining for the electron microscopic investigation of the crystallization of polyethylene. *Colloid and Polymer Science*, 261(4):373–374, 1983.

[133] BS EN ISO:527-2. Plastics-Determination of tensile properties, Part 2: Test conditions for moulding and extrusion plastics, 1996.

[134] M. A. Kennedy, A. J. Peacock, and L. Mandelkern. Tensile properties of crystalline polymers: Linear polyethylene. *Macromolecules*, 27(19):5297–5310, 1994.

[135] A. J. Peacock and L. Mandelkern. The mechanical properties of random copolymers of ethylene: Force-elongation relations. *Journal of Polymer Science Part B: Polymer Physics*, 28(11):1917–1941, 1990.

[136] R. Popli and L. Mandelkern. Influence of structural and morphological factors on the mechanical properties of the polyethylene. *Journal of Polymer Science Part B: Polymer Physics*, 25(3):441–483, 1987.

[137] G. R. Williamson, B. Wright, and R. N. Howard. Light scattering studies of narrow fractions of polyethylene. *Journal of applied chemistry*, 14(4):131–143, 1964.

[138] M. J. Galante, L. Mandelkern, and R. G. Alamo. The crystallization of blends of different types of polyethylene: The role of crystallization conditions. *Polymer*, 39(21):5105–5119, 1998.

[139] B. Schrauwen. *Deformation and failure of semi-crystalline polymer systems.* PhD thesis, Technische Universiteit Eindhoven, 2003.

[140] P. D. Coates and I. M. Ward. Neck profiles in drawn linear polyethylene. *Journal of Materials Science*, 15(11):2897–2914, 1980.

[141] P. B. Bowden and R. J. Young. Deformation mechanisms in crystalline polymers. *Journal of Materials Science*, 9:2034–2051, 1974.